POLITECNICO DI TORINO

MASTER THESIS IN BIOMEDICAL ENGINEERING

Fabrication and Mechanical Characterization of Self-Opening Intraneural Electrodes in OSTE+ for Optic Nerve Stimulation

Author
MARINA LIBERTI

Supervisors:
Prof. Diego GHEZZI
Prof. Danilo DEMARCHI

Co-supervisors:
PhD Eleonora BORDA

A thesis submitted in fulfilment of the requirements for the Master's degree in Biomedical Engineering

Laboratory of Medtronic Chair in Neuroengineering (LNE)

October 2019

In collaboration with

ÉCOLE POLYTECHNIQUE FÉDÉRALE DE LAUSANNE

CAMPUS BIOTECH

Abstract

Blindness is a disease that affects about 39 million people in the world. Vision loss is the result of the damage to one or more components of the visual system due to diseases such as Retinitis Pigmentosa and Age-Related Macular Degeneration, infection or trauma. One possible therapeutic approach is visual prostheses, whose working principle is the electrical stimulation in accord with the key-information received from the outside world. Among the visual implants, retinal prostheses are the most developed devices, even if their multiple restrictive criteria limit the implant. In addition to these, there is the optic nerve stimulation which, bypassing the entire retinal network, allows us to treat several cases. OpticSELINE is a new type of intraneural electrode, currently tested on rabbits, that emerges among the nerve stimulation implants. The advantage of this electrode is its three-dimensional configuration that not only improves the anchorage inside the nerve but also can stimulate spatially different fibres. The current version is made of flexible polyimide with twelve stimulating active sites. A drawback of this polymer is the high rigidity compared with the host tissue, which induces the formation of a fibrotic capsule around the device, reducing its functionality. To limit the foreign body reaction, in this work, an OpticSELINE was created in a biocompatible and softer resin: off-stoichiometry thiol-ene-epoxy (OSTE+). Once this polymer was mechanically characterised, the design was optimised by using ANSYS, with the introduction of structural changes related to the substrate variation. In particular, two design versions have been realised with dimensions respectively 1.1 and 1.86 times greater in width than the current device and having sixteen electrodes in total. The design enlargement could allow us to increase the number of electrodes to twenty-four and to improve the device mechanical stability. Once the process flow of new OpticSELINE had been optimised, the mechanical characterisation was carried out through tensile test and insertion/extraction tests in/from the rabbit explanted optic nerve. Additionally, the supports for the device fabrication and mechanical characterisation, as well as a possible optic nerve phantom to substitute the explanted nerve during the mechanical tests performed for the device optimisation, were realised.

Abstract

La cecità è una malattia che interessa circa 39 milioni di persone nel mondo. La perdita della vista può attribuirsi al danneggiamento di uno o più componenti del sistema visivo a causa di malattie come la Retinite Pigmentosa e la Degenerazione maculare legata all'età, infezioni e/o traumi. Un possibile approccio terapeutico sono le protesi visive, il cui principio di funzionamento è la stimolazione elettrica basata sulle informazioni principali ricevute dal mondo esterno. Le protesi retiniche sono quelle maggiormente sviluppate tra gli impianti visivi, anche se soggette a molteplici criteri restrittivi che ne limitano l'impianto. A queste si affianca la stimolazione del nervo ottico la quale, bypassando l'intero network retinico, consente di ampliare i casi da trattare. Tra le tipologie d'impianti per la stimolazione del nervo emerge OpticSELINE, un nuovo tipo di elettrodo intraneurale attualmente testato sui conigli. Il vantaggio di tale elettrodo è dovuto alla sua configurazione tridimensionale che permette non solo un migliore ancoraggio all'interno del nervo, ma anche la stimolazione di fibre spazialmente differenti. La versione attuale è realizzata in poliimmide flessibile con un totale di dodici siti attivi di stimolazione. Un limite di tale polimero è la rigidità elevata rispetto al tessuto ospite che induce la formazione di una capsula fibrotica attorno al dispositivo riducendone la funzionalità. Al fine di evitare ciò, in questo lavoro si è realizzato l'OpticSELINE con un polimero biocompatibile e più soft: off-stoichiometry thiol-ene-epoxy (OSTE+). Una volta caratterizzato meccanicamente tale polimero, si è ottimizzato il design, mediante l'utilizzo di ANSYS, con l'introduzione di modifiche strutturali legate a suddetta variazione di substrato. In particolare, si sono realizzate due versioni di design con dimensioni rispettivamente 1.1 e 1.86 volte maggiori in larghezza rispetto al dispositivo corrente e aventi sedici elettrodi in totale. L'allargamento del design consentirebbe, inoltre, un ulteriore incremento del numero di elettrodi fino ad un massimo di ventiquattro e un miglioramento della stabilità meccanica dell'impianto. Una volta ottimizzato il processo di fabbricazione del nuovo OpticSELINE, si è proseguito con la sua caratterizzazione meccanica mediante test di trazione e di inserzione/estrazione effettuati sul nervo ottico espiantato del coniglio. Inoltre, sono stati realizzati i supporti necessari alla fabbricazione e alla caratterizzazione meccanica dell'elettrodo, e si è fabbricato un possibile modello artificiale di nervo ottico utilizzato durante i test meccanici per l'ottimizzazione del design.

Acknowledgements

I would like to thank my supervisor Eleonora Borda, for having guided me every single day in the realisation of this project and for her countless advice. Your support has been indispensable and precious. I would like to express my gratitude to Professor Diego Ghezzi for allowing me to carry out this innovative project at the LNE laboratory. My sincere thanks also to Professor Danilo Demarchi for allowing me to develop the Master Thesis abroad, for supporting me and for being always kind and available.

A special thank to Adele Fanelli, for introducing me to LNE laboratory, for her essential support not only for professional matters and for being available in every single moment. I would also like to thank Marta Airaghi and all LNE Team. My gratitude is for the engineers Valérian Ruhaut and Anthony Guillet about the technical help they gave me during the microfabrication processes. I would also like to acknowledge Christian Vivori and Giulia Mongardi, with whom I have shared this memorable experience abroad and for making it too exciting.

I would like to express my gratitude to my Turin friends: Elena Vergori, Fabio Pontrandolfo, Simone Scutti, Silvia Pepe, Vito D'Orazio, Federica Miola, Giulia Merola, Sofia Milanese, Alessandro Gaeta, Matteo Di Bonaventura and Francesco Semeraro. Thank you for the unforgettable moments spent together that have made the five years in Turin tremendously exhilarating. I would like to thank all my friends of Collegio Einaudi, Anna Grosso, Max Carcia, Matteo Nicoletti, Cops, Gian Franco Piredda, Silvia Cosentino, Marianna Loffredo and Chiara Di Michele, the first people I met and who made me feel at home from the first day. I am so lucky to meet you.

I would like to thank my university friends, Valerio Votta, Alessia Sacco, Federica Amato, Elena Rondoni, without whom the lessons would not have been the same. I would like to express my gratitude to my friends Daniela, Gigi, Claudia, Valentina, Franco, Gianni, Babbe and Fracasso. A special thank to Valeria, a friend and companion since high school, point of reference and support. Thank you very much for all your time together.

A deep thank to my Mom, Dad, Luigi and Marco: your unconditional love and your daily support were necessary to live far from home. A sincere gratitude to my grandparents Luigi and Lucia and, in particular, Gino and Marina. You are for me an example of life, my second family. Finally, I would like to profoundly thank my boyfriend Gino, who has been always by my side during these years despite the distance, whom I have stressed particularly because of the exams and not only, who has always believed in me and without whom I would have never been the person I am today.

Contents

List of Figures

List of Tables

Glossary

ABSplus Acrylonitrile Butadiene Styrene

AMD Age-related Macular Degeneration

ASTM American Society for Testing and Materials

CE European Conformity

DI deionized water

EEPs electrically-evoked potentials

FDA Food and Drug Administration

FEA finite element analysis

FINE Flat Interface Nerve Electrode)

IPA Isopropanol

LIFE Longitudinal Intrafascicular Electrode

OpticSELINE Self-opening Intraneural Interface for optic nerve

OSTE+ off-stoichiometric thiol-ene epoxy thermosets

OSTE+ CC OSTEMER 322 Crystal Clear

OSTE+ Flex OSTEMER 324 Flex

PDMS polydimethylsiloxane

PET polyethylene terephthalate

PGMEA Propylene glycol monomethyl ether acetate

PI polyimide

PNS Peripheral Nervous System

PSS poly(4-styrenesulfonic acid)

Pt platinum

RGCs Retinal Ganglion Cells

RP Retinitis Pigmentosa

SELINE Self-opening Intraneural Interface

SNR Signal-to-Noise-Ratio

TBE tris/ borate/EDTA buffer

Tg glass transition temperature

Ti titanium

TIME Transverse Intrafascicular Electrode)

USEA Utah Slanted Electrode Array

VEPs visually-evoked potentials

Ai nonni Gino e Marina...

1 Background

Globally, there are about 253 million of people with vision impairment and 39 million of them are blind. Blindness has a significant impact both at the social and economic level: it reduces people's quality of life and increases health care cost [1].
Since ancient times, one has highlighted the value of visual perception, which allows us to understand the reality surrounds us, more than other senses do. *"All men by nature desire to know. An indication of this is the delight we take in our senses; [...] and above all others the sense of sight [...] The reason is that this, most of all the senses, makes us know and brings to light many differences between things"* (Aristotle, Metaphysics, Book I, 980a21).
Thus, the importance of sight has encouraged a profound study of eye's diseases and possible solutions to intervene in vision restoration. In particular, in the last 50 years, researchers focused on the stimulation of the visual system to partially restore the eyesight. It is necessary to analyse the working principle of the visual system to understand how electrical stimulation can produce visual perception.

1.1 Eye anatomy

The human eye is constituted by the eyeball, a spherical sac of 25 mm mean diameter and 6.5 cc volume. A cross-section in Figure 1.1 shows how the structure is organised into three levels:

- External layer: constituted by the sclera on the back and by the cornea on the front;
- Intermediate layer: composed of the iris and ciliary body located in the anterior area, and the choroid placed in the posterior one;
- Internal layer: corresponding to the retina, that covers two-thirds of the choroid.

The ocular structure forms three regions: anterior chamber (between cornea and iris), posterior chamber (among iris, ciliary zonula and crystalline lens) and vitreous body (between crystalline lens and retina) [2, 3].
The first two are filled with aqueous humour, whereas the vitreous body with vitreous humour which is a more viscous liquid. The crystalline is a transparent lens maintained in its position by a circular ligament also called crystalline ligament, which is connected to the ciliary body on the anterior side of the choroid. As a consequence of the ciliary muscle action, the ligament contraction and relaxation change the lens' curvature: this process is called accommodation and allows to form a clear image on the retina.

It is possible to distinguish three types of tissues [4]:

- Refracting tissues, that focus entering light onto the light-sensitive tissues. They include lens, iris, pupil, cornea, vitreous and aqueous fluid;

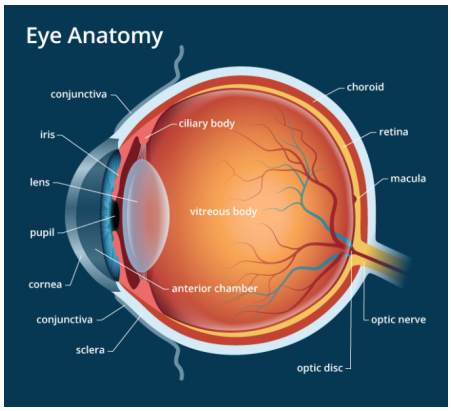

Figure 1.1: Cross-section of human eye anatomy. *From Liz Segre.*

- Light-sensitive tissues (retina), that convert the detected light into electrical stimuli;
- Support tissues, including choroid, conjunctiva and sclera which support and lubricate the eyeball.

The retina is the most internal membrane of the eyeball formed of a retinal pigment epithelium (RPE) and 200 μm thick. It is composed of about 126 million photoreceptor cells (i.e. rod and cone cells) and other four types of neurons: ganglion cells, bipolar cells, amacrine cells and horizontal cells [5]. In the macula, the retinal central area, there are the cone cells that are used for chromatic vision and give images of high spatial resolution. Whereas, the rod cells around the retina's edges are responsible for achromatic view with low spatial resolution in semi-darkness. RPE cells provide nutrients to photoreceptors to ensure their functions. Through the synapses, cone and rod cells are directly connected to the bipolar cells, which, in turn, form synapses with the ganglion cells [6].

At the back of the eye, ganglion cells axons converge and form the optic disk, the starting point of the optic nerve. The fibres reach the optic chiasm, where some of them continue on the same side towards thalamus and the others cross the chiasm. This disposition produces a binocular vision. The fibres of the same side compose the optic tract and target the lateral geniculate nuclei that form, instead, the optic radiation. They are headed toward the primary visual cortex, located in the occipital lobe, which maps the information to the original image [7].

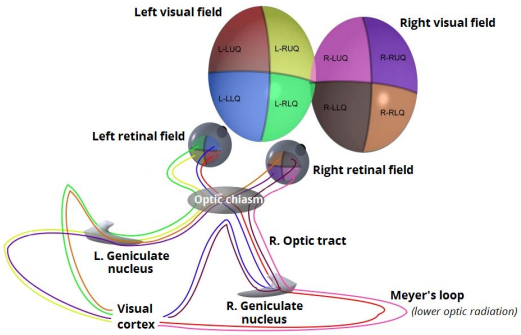

Figure 1.2: Overview of Visual Pathway. The fibers start from the back of the eye, reach the optic chiasm where they divide, continue towards the geniculate nucleus up to the visual cortex. After chiasm, the fibers on the same side form the optic tract. *From Dr. Melanie Gibson et al.*

Light-sensitive tissues include also the optic nerves, which are not considered as the peripheral ones because they are wrapped by myelin produced by oligodendrocytes. They are cylindrical and paired structures containing about one million of fibres, enclosed by three layers: pia mater, arachnoid, dura mater. The optic nerve is divided into four parts [8, 6, 9]:

- the intraocular segment (i.e. optic nerve head). It is within the walls of the eyeball, 1 mm long and with myelinated axons;
- the intraorbital segment. It is 20 – 25 mm long between the eyeball's back and the optic canal;
- the intracanalicular segment, which is 4 – 10 mm in length inside the optic canal;
- the intracranial segment, which is 4 – 16 mm long.

The nerve's average length is in the 35– to 55-mm range and the average diameter is about 3 – 7 mm. It functions as a bridge that transfers the afferent pulses from the retina to the brain.

1.2 Visual perception

The process of visual perception creation starts when the light, getting through the pupil, is focused by the crystalline lens on the pigment epithelium, that constitutes the deep layer of the retina. The result is the projection of an object's image, reduced and upside down, on photoreceptors. They start the conversion of luminous signals coming from the external world into electrical potentials, through a sequence of enzymatic processes. This process is called *phototransduction* and allows this conversion thanks to light-sensitive proteins called opsins. Through the synapses, the cone and rod cells are directly connected to the bipolar cells linked via synapses with the ganglion cells. Ganglion cells axons converge and leave the eye, forming the optic nerve with glial cells. The latter transmits the visual signals through the lateral geniculate nucleus to the primary visual cortex, which interprets and processes them to evoke the visual perception [4].

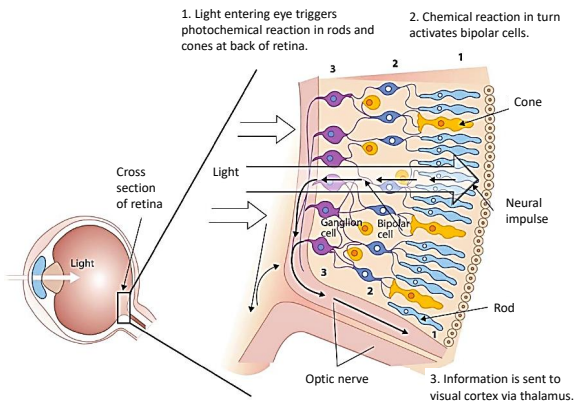

Figure 1.3: Main steps of visual perception. Light arrives to the retina, triggers photochemical reaction. Electrical signal passes through the bipolar cells connected to the ganglion cells and arrives to the optic nerve, which transmits it to visual cortex. *From Jennifer Walinga et al.*

1.3 Diseases of the eye

Blindness is a consequence of an impairment in one of many structures of the visual pathway. The two most frequent degenerative diseases of the retina are *Age-related Macular Degeneration (AMD)* and *Retinitis Pigmentosa (RP)* [10]. In these circumstances, it is possible to restore the sight, because the eye is not completely destructed and the neural connections are preserved [11].
The *AMD* represents over 50% of the visually impaired in western countries. It involves the macula, that facilitates the central vision with high visual acuity, thanks to the elevated content of photoreceptors. Therefore, AMD progression implies the loss of central vision, maintaining the peripheral one [10]. The more important risk factors are represented by smoking and age, and the principal causes are inflammatory processes, mitochondrial dysfunction and oxidative stress [10].
The *RP* is a genetic disease, characterised by a gradual degeneration of the retinal photoreceptors. The degeneration usually starts from the mid-periphery of the pigment epithelium and progresses towards the macula and the fovea. The most common form of *RP* is the dystrophy of cones and rods, in which the first symptom is the loss of nocturnal vision with difficulties in dim light, followed by a gradual loss of the peripheral visual field and the development of a "tunnel vision" [12].
In the last years, more than 200 million persons are either affected by low vision or are

(a) *AMD* **(b)** *RP* **(c)** *Normal*

Figure 1.4: Comparison of visual fields in normal condition and in pathological ones: AMD and RP. *From Shepherd et al.*

blind because of these diseases. In Figure 1.5 it is reported the number of patients affected by AMD and RP in Europe and the US [10, 12].

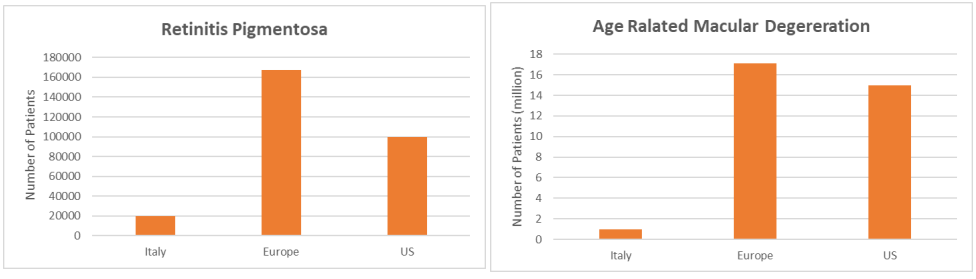

Figure 1.5: Number of patients affected by RP (*left*) and AMD (*right*) in Italy, Europe and the US. *Data from NanoRetina.*

1.4 Methods of treatment

The above diseases, as well as lesions to main elements, are not treated with medication or surgery, but another treatment is necessary. Nowadays, the most effective method consists of stimulation of the visual system, which recovers only a limited part of the patients' sight. Nevertheless, there are further methods to tackle these problems to improve the quality of life of the affected patients [12].

The first is known as *optogenetics*. Its purpose is to replace the damaged photoreceptors transforming the inner retinal cells into photosensitive cells. Thus, embedding Channel Rhodopsin-2 or Halo Rhodopsin in these cells, neurons become sensitive to light, even if the lack of sufficient sensitivity to light could limit the visual benefit [13].
The second approach is the *transplants of the stem cells*. Thanks to cells' ability to differentiate into other types, it is possible to reconstruct the retina with lesions. Nevertheless, there are some issues to overcome before this therapy may be used [13].
The third method under investigation uses *ultrasound waves* to stimulate ganglion cells. Indeed, it has been proven that sound waves can induce a response in the retinal cells [14].
Another possible approach is *gene therapy* that may not be realised for decades, because it is difficult to demonstrate safety, but has shown some promising results in AMD patients [13].

Unlike the above approaches, the electric stimulation guarantees two advantages: low risks during electrode implantation and signal propagation similar to natural visual pathway [13]. It is able to partially restore the sight thanks to the fact that neurons are electrically excitable. For these positive aspects, researches are focusing on this method that has reached clinical practice, developing different types of visual prostheses [13].

1.5 Fibrotic capsule

A prosthesis or any medical device implantation requires a careful analysis of the biomaterials they are made of and their properties. The main goal of engineering is to fabricate long-term device characterised by numerous electrodes and limited cross-section to reduce tissue damage [15]. Biomaterials characteristics modulate the inflammatory response and the foreign body reaction that develops when the tissue comes into contact with the device.

Analysing in detail the process which evolves after an implant [16], we can see how the inflammatory response is characterised by different stages (Figure 1.6), the last of which is the fibrotic capsule formation. A few minutes after the implant, the device comes into contact with blood and its proteins. In this phase, the absorption of the proteins on the biomaterial's surface leads to the formation of a protein layer that covers it. Thanks to hydrophilic and hydrophobic structures, as well as the residues with positive and negative charges, proteins can adhere to different surfaces. During protein-surface interaction, proteins can be denatured by cancelling their functionality, or they can rearrange themselves by altering their function. An important effect is the Vroman effect which occurs during this phase. Vroman demonstrated the serum absorption on a surface is a dynamic process in which low weight and high concentration proteins arrive first. They are, then, replaced by larger proteins in lower concentration but with greater affinity for the surface. In the temporal range of an hour - one day after implantation, neutrophils and macrophages interrogate the biomaterial with input/output signal exchanged between cells and proteins bound to the device surface. Subsequently, after one to five days, the cells emit signal proteins and, then, different reactions occur according to these. If the ma-

terial is considered foreign, after about three weeks of implantation, a fibrotic capsule is formed to isolate it from the tissue. Otherwise, if the material is not considered as foreign, after about five to fourteen days from the implant, it is integrated into the newly formed tissue. In the case of a foreign implant, acute inflammation occurs after protein absorption and it generally lasts less than a week depending on the extension of the injury. It is followed by a short-term chronic inflammation response characterised by the presence of mononuclear cells at the implant level. The last stage of the inflammatory response sees the macrophage reaction, their interaction with the foreign body giant cells and the formation of the fibrotic capsule. These reactions induce corrosive effects that lead to device degradation and reduce its efficiency and lifetime.

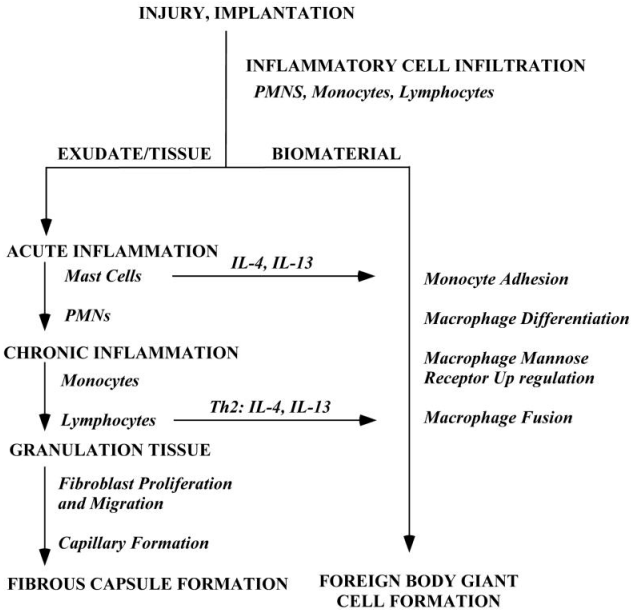

Figure 1.6: Main events that occur when a "foreign" device comes into contact with the tissue. An important role is played by Mast Cells and Lymphocytes which can lead to the formation of the fibrotic capsule. *From James M. Anderson and Chang.*

Overall, one of the main causes of the fibrotic capsule formation is the mechanical mismatch between neural tissues (Young's modulus of 100 - 1500 kPa) and stiff implants characterised by an elastic modulus of two - five orders of magnitude greater [17]. Knowing that the interactions with the biomaterial affects the viability and differentiation of cells, precise surface strategies are needed to control them. In particular, attempts are being made to create more functional, non-rigid surfaces suitable for both microscopic and macroscopic tissue motions able to reduce their mechanical mismatch [17]. A study on long-term biointegration was conducted by Minev et al., in which the soft implants in silicone and the plastic and stiff implants made in polyimide, 25 μm thick, were compared. The stiff implants showed deterioration over time and induced motor impairments after two weeks of implantation. Moreover, the material stiffness triggered the foreign body reaction, highlighted by the astrocytes and microglia accumulation around the device surface. Of course, it is possible to reduce the implant thickness to improve the device flexibility, but that, in turn, could cause the device failure. These drawbacks have been overcome with soft implants, instead. The induced inflammatory response did not differ from the sham-operated animals, highlighting the long term biocompatibility of soft implants [17]. In addition to the biomaterial analysis, it is also possible to adopt other approaches

to reduce an inflammatory response. Modification of implant shape, cross-section area and electrode sites could help to increase SNR and elicit the smallest tissue response [18]. Moreover, the method used for fastening the implant also influences the possible inflammation [19]. To sum up, an implant design has to take into account surface biocompatibility, structural biocompatibility and biostability of materials [20].

1.6 Visual prostheses

The visual prostheses are implantable devices, capable of partially restoring the sight thanks to electrical stimulation.
In 1929, Foerster demonstrated the possibility of having bright spots, scientifically called phosphenes, with electrical stimulation of the cerebral cortex. In particular, he showed the stimulation points correspond, more or less, with the position of phosphenes [21].
Thanks to this, Brindley realised the first prototype in 1968. He implanted eighty platinum electrodes enclosed in a silicon cap into the right visual cortex of a blind patient, observing the formation of phosphenes in the left half of the visual field [22]. The position and brightness of these spots are influenced, respectively, by stimulation site and pulses characteristics [21]. However, the main problem of this prototype was the possible risk of epileptic seizures.
In 1974, Dobelle et al. changed the prosthesis model by including a camera. In this way, patients were able to identify simple figures [21].
Later, in 1998, M. Humayun (UCS) demonstrated that a blind patient could see light thanks to the retinal nerve ganglia stimulation. Thus, the idea of translating the images into electrical pulses to restore vision was central to the visual prostheses development [23].

Generally, these prostheses are characterised by (Figure 1.7):

- **External Module**, which allows images to be pre-processed to extract the main information;
- **Internal Module**, which transfers the information to the stimulator back-end to generate the electrical impulses for target tissue stimulation [23].

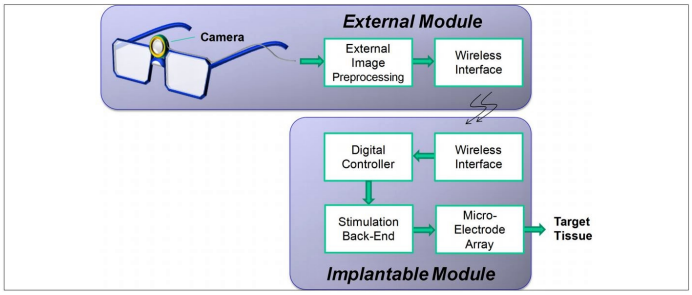

Figure 1.7: Main components of a prosthesis structure grouped in External Module and in Internal Module. *From Mohammad Riazi-Esfahani et al.*

There are several types of implants classified by the anatomical location along the visual pathway where the electrode array is implanted, as shown in Figure 1.8. It includes [11, 23, 22]:

- Epiretinal prosthesis (electrodes located to the inner retinal surface);
- Subretinal prosthesis (electrodes implanted between bipolar cells and the retinal pigment epithelium);

- Suprachoroidal prosthesis (electrodes located in a tissue pocket between the choroid and sclera);
- Optic nerve prosthesis;
- Thalamic prosthesis;
- Cortical prosthesis.

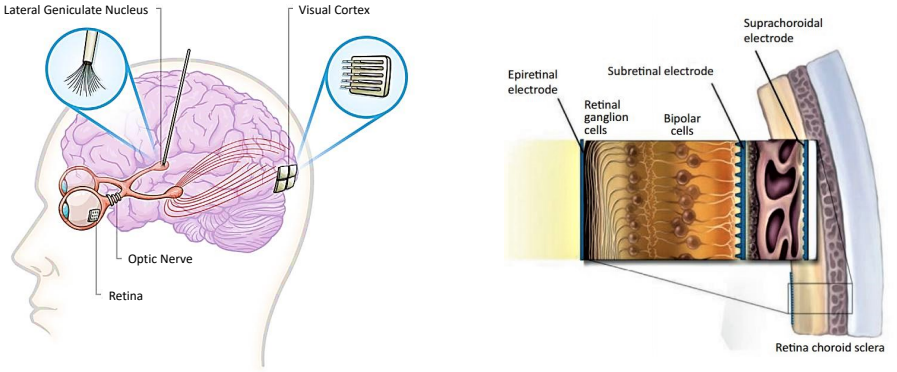

Figure 1.8: Differentiation of prostheses based on location of the stimulated area. It is graphically represented the anatomical region along visual pathway where they stimulate. General visual prostheses (*left, modified from Lewis et al.*) and retinal prostheses (*right, modified from Shepherd et al.*) are illustrated.

The **retinal prostheses**, capable of preserving the signal's natural processing, represent a growing market: more than 250 retinal prostheses have been implanted. Although one of their main limitation is the restricted range of diseases that can be treated (i.e. only diseases affecting retinal photoreceptors), the interest in these prostheses is increasing thanks to the simple surgical access and the less complex algorithm to convert visual information in spatial one [21]. Another issue is the quality of vision which depends on the number and dimension of the electrodes. In the central macular region, the ratio between cones and ganglion cells is 1:1. Such a ratio cannot be preserved with prostheses, because the diameter of the electrodes cannot be reduced too much, lest the current density becomes too high damaging the surrounding tissues [14]. At best, these patients may recover part of their sight (max 15 – 20 degrees) with low resolution, and the images will look to them as sequences of black and white photograms made of pixels [24]. There are other prostheses which consist of micro-photodiodes instead of electrodes, located inside the eyeball to stimulate the ganglion cells. These arrays convert the incoming light in nanoampere currents that are, unfortunately, insufficient to stimulate neurons, whose stimulation threshold is about 10 mA. Unlike other retinal prostheses, it does not require an external image and data processing as well as an eye-tracker to obtain the eyes positions in real-time [23].
One of the pioneer companies is Second Sight. Its main product is *Argus II*, epiretinal prosthesis with sixty electrodes, which is approved for marketing by the European Union (CE, March 2011) and the US Food and Drug Administration (FDA, February 2013) [23]. The epiretinal approach guarantees easy surgical procedure and low thermal risks thanks to the dissipation of heat in the vitreous chamber [21]. Its main issue is mechanical stability, unlike the subretinal implant. An example of this type is the *Boston Retina Implant*, characterised by polyimide electrodes with sputtered iridium oxide [23]. It exploits the natural visual pathways avoiding visual distortion due to ganglion cells stimulation. However, its

main problem is the high possibility of thermal injury that could cause retinal detachment. In addition to it, the German firm Retina Implant developed a subretinal prosthesis with photodiodes. Thanks to its 1500 photodiodes, it can guarantee a more detailed visual perception. Good stability and safe implantation are offered by suprachoroidal prostheses which, unfortunately, require a high stimulus threshold due to the distance between electrodes and retina [22].

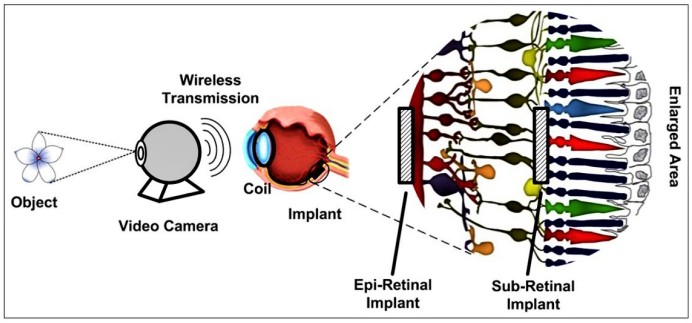

Figure 1.9: Main components of a retinal prosthesis structure. *From Mohammad Riazi-Esfahani et al.*

The **cortical prostheses** have the advantage of bypassing the entire visual pathway and treating patients suffering from damage of both retina and optic nerve. The disadvantages of this approach are the high surgical risk, the high invasiveness and the extra complicated image processing due to the high complexity of visual field organisation [11, 23]. Moreover, direct cortical stimulation could induce the risk of focal seizures. An example of this typology is the cortical prosthesis developed by Dobelle, that is characterised by sixty-four electrodes in platinum, a television camera and a battery-powered transmitter. Subsequently, the Dobelle Institute team succeeded in developing and miniaturising the cortical implant by increasing the computing power and battery life [23].

Regarding the **thalamic prostheses**, the electrodes are located in the Lateral Geniculate Nuclei. They have a surgical procedure similar to deep brain stimulation's one. However, they have not been clinical trials yet. Their main issues are the limited number of electrodes that it is possible to implant as well as the low visual resolution obtained [22].

The **optic nerve prostheses** are an interesting approach because they guarantee an easier implantation than other prostheses and allow nerve fibres to be directly activated bypassing the entire retinal network. Therefore, they can treat a wider range of diseases than retinal prostheses, suitable also for patients with total retinal degeneration. The stimulation of a small area allows to activate a large portion of the visual field because the ganglion cells axons are a bundle. The drawback is the difficulty to achieve a focal stimulation and detailed perception through a cuff electrode [23]. This electrode type, made in silicon, is used in the prototype of optic nerve prosthesis, realised by C. Veraart in 1998. One stimulates with charge-balanced single pulses and pulses trains obtaining low selectivity and irregular phosphenes [25]. Whereas, H. Sakaguchi et al. developed a system based on three-wire electrodes, implanted into the optic disc of patients with RP. This type of electrodes has the advantage of having a better localisation of the phosphenes. The main problem is the surgical procedure during which the electrodes are displaced. To overcome this problem, they have developed a system with seven wire electrodes and a return electrode coated with polytetrafluoroethylene instead of parylene. In this way, they have simplified the implantation during the study conducted on rabbits [26]. Moreover, C-Sight realised a prosthesis with four penetrating multi-electrode arrays in platinum-iridium, im-

planted at the intraorbital level and able to guarantee high temporal and spatial resolution through small currents [23, 27].
The frequent issue of all these prostheses is the mechanical mismatch due to the high stiffness of electrodes compared with the surrounding tissue. To overcome these drawbacks, we are focusing on a new type of electrodes, the OpticSELINE.

Figure 1.10 and Figure 1.11 show an overview of different research groups and their respective prostheses developed over time.

Country	University	Researchers	Group name	Approach
USA	University of S. California (Doheny Retina Institute) and University of California	M. S. Humayun, W. Liu, and J. D. Weiland	Artificial Retina	Epi-retinal
Germany	RWTH Aachen University and Fraunhofer Institute of Microelectronic	W. Mokwa	N/A	Epi-retinal
Germany	IMI Intelligent Medical Implants andInst. of Microelectronics, University of Ulm	R. Hornig and M. Ortmanns	Intelligent Medical Implants	Epi-retinal
Iran	K. N. Toosi University of Technology	A. M. Sodagar, A. Lashay and M. Riazi	ICAS	Epi-retinal
USA	Massachusetts Institute of Technology and Massachusetts Eye and Ear Infirmary	J. Rizzo, J. Wyatt and W. A. Drohan	Boston Retinal Implant	Sub-retinal
Germany	Tübingen University, Eye Hospital	E. Zrenner	Retina Implant	Sub-retinal
USA	Loyola University of Chicago, School of Medicine	Alan and Vincent Chow	Artificial Silicon Retina	Sub-retinal
Japan	Osaka University, Medical School	Y. Tano, T. Fujikado and H. Sawai	Japanese Consortium for an Artificial Retina	Suprachoroidal-transretinal stimulation
USA	Stanford University	D. Palanker	Optoelectronic Retinal Prosthesis	Photovoltaic retinal prosthesis
Australia	Centre for Eye Research Australia at the University of Melbourne, the Bionic Ear Institute and the Vision Sciences Group at the Australian National University	N. Lovell and G. Suaning	Australian Vision Project	Optic nerve stimulation/ retinal
Belgium	Catholique Université de Louvain	C. Veraart	Vision Project	Optic nerve stimulation
China	Shanghai Jiao-Tong University	X. Chai and Q. Ren	C-Sight	Optic nerve stimulation
Portugal	Dobelle Institute	W. Dobelle	N/A	Cortical
Canada	Polytechnique Montreal University	M. Sawan	Polystim	Cortical
USA	University of Utah	R. Normann	Utah Artificial Vision	Cortical
USA	Illinois Institute of Technology	P. R. Troyk	N/A	Cortical

Figure 1.10: Overview of artificial vision projects with respective research groups and prosthesis approaches. *From Riazi-Esfahani, Maghami et al.*

Visual prostheses	Retinal prostheses				Optic nerve head prostheses	Cortical prostheses
	Argus® II	Alpha-IMS	IMI, IRIS	EPI-RET 3 ('wireless' implant)		
Image capture	Extrinsic video camera	Intrinsic optical system	Extrinsic video camera	Extrinsic video camera	Extrinsic video camera	Extrinsic video camera
Light waves transduction into electrical signals	Extrinsic conversion by an external VPU	Intrinsic conversion by direct activation of micro-photo-diodes (MPDA)	Extrinsic conversion by an external processing unit	Extrinsic conversion by an external processing unit	Extrinsic conversion by an external processing unit	Extrinsic conversion by an external processing unit
Number of electrodes	60	1500 micro-photodiodes, each connected to an amplifier and electrode	61	25	Spiral nerve cuff (MiViP);[1] 3 (AV-DONE): 16[3]	Dobelle: 64 Normann: 100
Field of vision	Up to 20°	11° × 11°	Up to 40°	Not available	14° × 41°	Not available
Site of stimuli	Inner retina with epiretinal electrodes	Outer retina with subretinal electrodes	Inner retina with epiretinal electrodes	Inner retina with epiretinal electrodes	Optic nerve head	Striate cortex of occipital lobe
Visual processing	Extrinsic processing by computer algorithms	Intrinsic intra-retinal processing	Extrinsic processing by computer algorithms	Extrinsic processing by computer algorithms	Extrinsic processing by computer algorithms	Extrinsic processing by computer algorithms
Status	Commercially available in Europe (CE mark March 2011) and the USA (FDA approval February 2013). Trials identifier: NCT01490827	Commercially available in Europe (CE mark in July 2013). Trials identifier: NCT01024803	Phase II clinical trial commenced January 2007. Clinical Trials identifier: NCT00427180	Completed acute clinical study. Awaiting further development and approval for chronic study	Experiments performed on volunteer human subjects	Experiments performed on volunteer human subjects

Figure 1.11: Overview of different visual prostheses and their main characteristics. *From Yvonne H.L. Luo et al.*

1.7 Electrodes typologies

There are several typologies of PNS neural interfaces subdivided on their invasiveness. It is possible to use and adapt them to optic nerve stimulation. Moreover, it is important to analyse the longevity and the spatial resolution they can guarantee, and the electrode-tissue interaction that could affect stimulation due to the inflammatory reaction, to assess the quality of the electrode. The PNS neural interfaces are distinguished in [28]:

- **Extraneural (or Surface) Electrodes**, that have been used in several human studies [29]. Their localisation is around the nerve, so they can measure the electrical potential at the exterior of the nerve and stimulate only the fibres near to surface, obtaining a low selectivity [30]. On the other hand, their main advantage is the low invasiveness, therefore they are suitable for acute and chronic implantation and they represent a stable interface with the nerve. In 2017, Christie et al. demonstrated the electrodes ability to operate for just over ten years, the entire experiment duration. There are different types of these electrodes: split-cylinder and spiral type. The first type consists of a flat ring, made in biocompatible polyimides, split in one side and located around the nerve [29]. Another variant of the first type is FINE (Flat Interface Nerve Electrode), made of silicone with platinum electrode sites, as shown in Figure 1.12a. It is characterised by a fixed diameter to be adapted to the nerve. Moreover, it remodels the nerve, improving the selectivity and spatial resolution thanks to the possibility to be closer to fascicles, but it could increase the possible damages due to mechanical pressure that causes changes in axons and myelination. Nevertheless, it was noticed that the electrodes don't have significant chronic effects, because the nerve can recover after implantation [29]. The spiral type, instead, self-adapt to the size of the nerve, but it needs a more complex surgical procedure [30].

- **Regenerative Electrodes**. The nerve is forced to grow inside this electrode [28]. There are two types: sieve electrodes (in Figure 1.12b) and regenerative multi electrode array [29]. The first type, located between the ends of the nerve, is characterised by conductive micro-pores that allow nerve regeneration. The second type, instead, is characterised by several spikes, such as USEA which will be described later. In general, these electrodes require nerve excision and, therefore, they are very invasive. A high spatial resolution can be obtained, depending on the number of micro-pores for the first type. However, these electrodes have not yet been used for neuroprosthetic [29].

- **Intraneural (or Penetrating) Electrodes**. They are implanted inside the nerve, in direct contact with the fascicles and, therefore, they reduce the stimulation threshold guaranteeing greater selectivity than other electrode types. LIFE (Longitudinal Intrafascicular Electrode), TIME (Transverse Intrafascicular Electrode) and USEA (Utah Slanted Electrode Array) belong to this group.
  LIFE, a flexible electrode, is characterised by an insulated wire of 25 – 50 μm in diameter and an uninsulated part, that is adjacent to the fibres after insertion performed through a needle. The wires are made of platinum-iridium or platinum and are insulated with Teflon. Thin-film LIFEs is another variant of this electrode realised in micropatterned polyimide with eight electrode sites [29]. The stiffness of LIFE reduces the signal's quality due to the electrode's motion into the nerve and the consequent inflammation which is, instead, limited by thin-film LIFE. Moreover, it is difficult to achieve a good spatial resolution because of the longitudinal model, in which the electrode sites are only close to a fascicle [29].
  TIME (Figure 1.12c) is inserted transversely into the nerve, so guarantees a good spatial resolution, good selectivity and minimum motion of electrodes within the fascicles. It is characterised by a substrate in polyimide with ten electrode sites in

platinum. Moreover, this implant reduces the inflammation and surgical damages, as Kund et al. demonstrated in studies on pigs [29].
USEA is a variant of Utah electrode array (Figure 1.12d), characterised by a plane with several platinum electrodes at different heights to stimulate fascicles in different positions. The high quantity of wires increases the probability of chronic damage and makes the device fragile, reducing the quality of the signal over time. The device longevity, evaluated by some implants, has brought several results, showing little inflammation after weeks, months or a year from implantation. Besides, they allow to stimulate with high spatial resolution [29].
Overall, the main drawback is the electrodes' displacement because of their higher stiffness compared with the surrounding tissue. This causes the reduction of the Signal-to-Noise-Ratio (SNR) and increases stimulation [28].

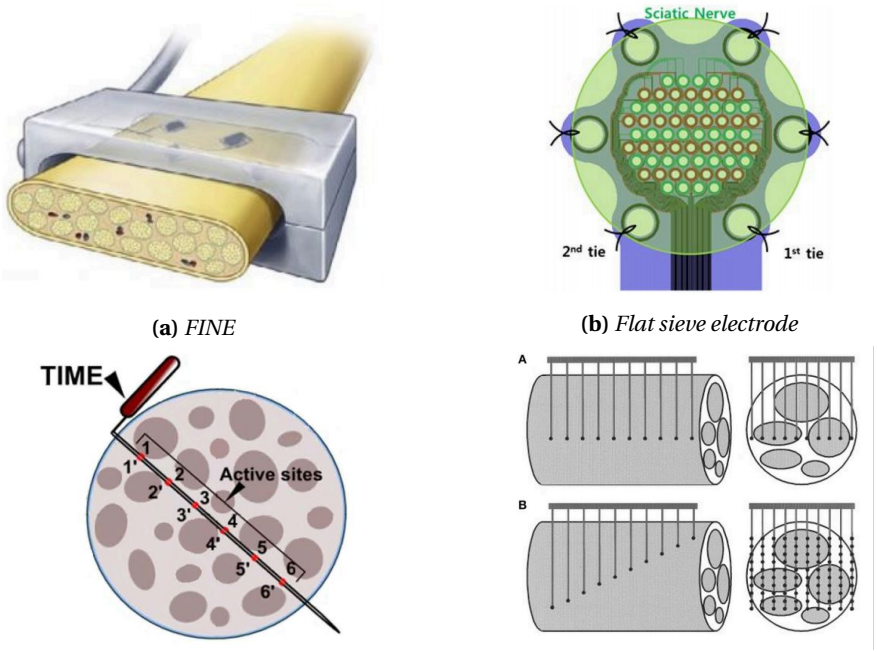

(a) *FINE*

(b) *Flat sieve electrode*

(c) *TIME*

(d) *Utah Electrode Array (A) and USEA (B)*

Figure 1.12: Schematic representation of different electrode typologies. *From Rijnbeek et al.*

To overcome these issues (i.e. spatial resolution and longevity) a new typology of intraneural electrodes has been developed: **Self-opening Intraneural Interface (SELINE)**. This device is a three-dimensional closed-loop structure and consists of a main body with four flaps, two per side. Moreover, it has ten active sites located on the wings (two per each wing) and the main body (one per each side), as shown in Figure 1.13a. The wings are plastically deformed with a specific opening angle (30° with the main shaft) to facilitate the anchoring to the nerve, to guarantee chronic stability and to reduce the displacement of the electrical contacts. The greater the distance between electrode and tissue, the worse the signal and the stimulation. The memorization of the wings (Figure 1.13b) is made using a 10 N load cell that constrains the base and a vertical panel to open the wings on one side [28]. The dimensions of main shaft (20 mm x 0.36 mm x 11 μm) and the wings were evaluated based on both theoretical and finite element results obtained by Cutrone et al. The configuration of SELINE allows the wings to come into contact with different axons from several sub-fascicles, ensuring excellent selectivity, and facilitates the insertion of the device thanks to an apical part with reduced width.

Electrodes	Recording	Stimulation # individual muscles	Longevity
Cuff	Up to five fascicles (Spatial Filtering)	Up to 10 and 15 percept areas triggered (spiral cuff)	Stable stimulation (after up to 10.4 years)
LIFE	No quantitative data available	2.00±0.89	Slight and reversible damage (after 3 months)
TIME	No quantitative data available	3.68±1.49	Fibrotic layer around the implant, no necrosis or inflammatory cells (after 30 days)
USEA	13 different movements (Offline Decoding)	5 to 10	Mild or no inflammatory response after 8 weeks and 7 months. Inflammatory reaction after 1 year study
Regenerative	Due to high number of holes, high specificity may be possible	At least three	Fascicles regeneration can take up to a month and is not guaranteed. When regenerated, long-term recording and stimulation may be possible up to 3 or 4 months

Table 1.1: Comparison of spatial resolution and longevity among different types of electrodes. *Modified from Rijnbeek et al.*

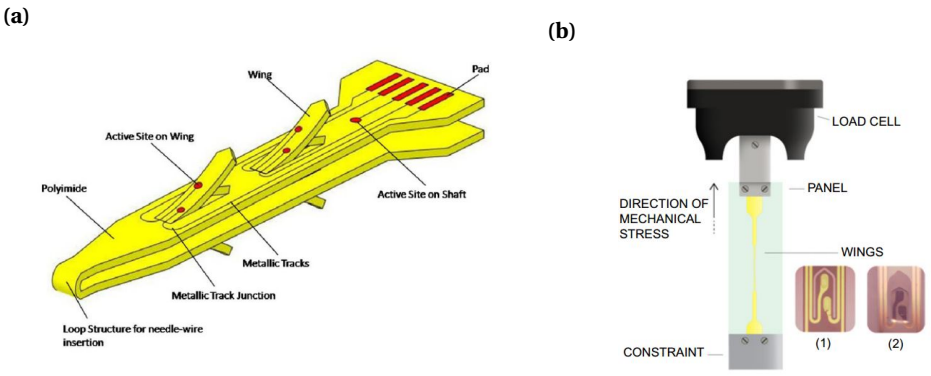

Figure 1.13: *(left)* Schematic drawing of SELINE. The 3D closed-loop structure consists of main body, four wings and ten active sites. *(right)* Sketch of setup for wings memorization: a 10 N load cell, a press to constrain the base and a vertical panel to open the wings on one side. *From Cutrone et al.*

During implantation, the device enters the nerve through the hole made previously by needle and, then, it is slightly pulled back to allow the wings to anchor to the nerve, as shown in Figure 1.14. It can be implanted both transversely and obliquely to the nerve axis. However, a transversal implant is preferred because it reduces the invasiveness and facilitates the opening of the wings, that becomes more difficult in a longitudinal implant [31].

This device, made in polyimide with electrical contacts in gold with titanium, is biocompatible, flexible and electrically efficient [28]. Furthermore, it has been demonstrated that SELINE provides good mechanical stability without any sign of degeneration or variation in the fascicular organisation. During implantation, there is the formation of a fibrotic capsule which causes an increment of the nerve diameter, but without varying its conduction characteristics. This capsule grows for the first four weeks after implantation but remains stable after. Despite this foreign bodies reaction, the functionality of the device has been demonstrated for the entire duration of the experiments conducted on the sciatic nerve of rats (six months). Indeed, there is a reduction of fibrotic encapsulation than other devices because the wings move the active part away from the central body [32].

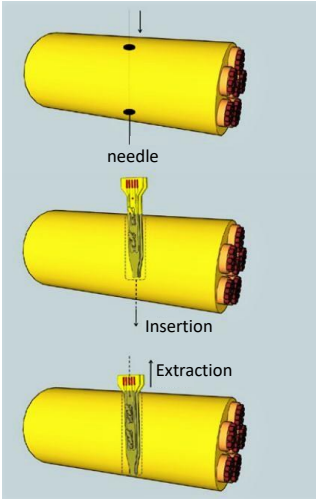

Figure 1.14: Schematic drawing of implantation procedure. The device enters the nerve and, subsequently, it is slightly pulled back to open the wings. *Modified from Cutrone et al.*

Starting from this new type of electrodes, thanks to promising advantages, V. Gaillet et al. have modified the design adapting it to the size of the rabbit optic nerve [33].

1.8 OpticSELINE

The **OpticSELINE** is the new neural interface used for optic nerve stimulation. Its structure is similar to that of SELINE, described in Section 1.7 and implanted in rats sciatic nerve. It has a 3D closed-loop geometry with two wings and six electrodes per each side, a reference and a ground electrode in the main shaft outside the active area, i.e. the region in contact with the nerve and where the electrodes are positioned. The total size of the current version is 33 mm in length plus 2 mm to connect the electrodes to the head plug connector, 3 mm in width an 12 μm in thickness. The active area is 0.43 mm wide and 1.39 mm long, while the wings are 0.15 mm wide and 0.48 mm long and are spaced 0.43 mm apart. V. Gaillet et al. have sized the entire device based on the dimensions of the rabbit optic nerve, which has an average diameter of about 1.5 mm (1.45 $\pm$ 0.04 mm) [33].

The device is a thin film of polyimide (PI-2611) made using the micro-fabrication techniques on a silicon wafer as a sacrificial layer. The traces, pads and active sites are made of titanium and gold, instead.
Regarding the wings memorization, the thermal treatment was carried out at 200 °C for an hour to have a three-dimensional structure, instead of the mechanical treatment done for SELINE. For this purpose, a specific mould was utilised as support, characterised by holes at wings level and needles to keep them in their respective positions. However, this type of procedure does not open the wings at a specific angle [33].

The implant steps are the same as that of SELINE: the insertion, during which the device passes through the hole made by the suture needle, and the subsequent slight extraction to allow the wings to fasten inside the nerve. The OpticSELINE is implanted transversely to the optic nerve axis in the intracranial trait instead of intraorbital one. This latter region is critical for the movement of the eyes and, therefore, would subject the electrodes to greater stress and probable damage. Furthermore, other problems related to intraorbital

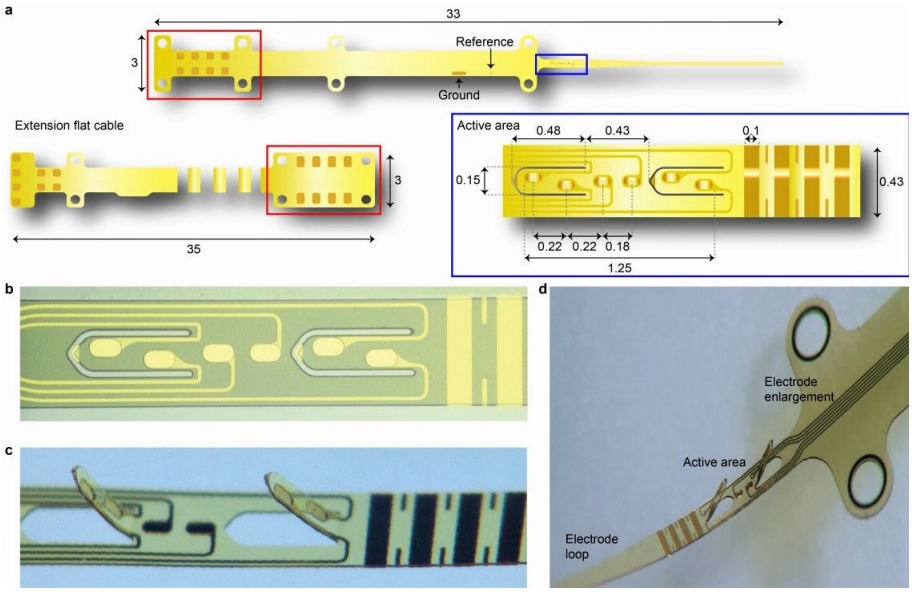

Figure 1.15: *(a)* Schematic representation of the OpticSELINE with its dimensions in mm. The red rectangle encloses the connection area between the electrodes and the cable for the connection to the stimulator. The active area, enclosed in the blue rectangle, is represented with the respective dimensions in mm. It is characterised by 2 wings and 6 electrodes. *(b)* Enlarged view of the active area after microfabrication. *(c)* Magnification of active area with wings, electrodes and alignment bars after wings memorization. *(d)* Representation of one side of OpticSELINE. The lateral stoppers correspond to the electrode enlargement and are used for limiting the device insertion within the nerve. *From Gaillet et al.*

implantation are the presence of the vein and the artery that could be damaged as well as the need to stimulate with higher intensities due to the greater stimulation threshold [33].

The device has been mechanically and electrically tested. In particular, mechanical tests were carried out using a 10 N load cell and setting a speed of 0.25 mm/s to evaluate the insertion and extraction forces, from which the device compatibility and stability in the nerve can be deduced. During the first phase, two main insertion forces develop linked to the loop insertion and the enlargement of the structure at the active area level. In the second phase, instead, the extraction force, that is the force necessary to dislocate the electrodes from the nerve, reaches its maximum during the wings extraction. It demonstrates the wings importance to ensure greater mechanical stability.
Regarding the electrical analysis (cyclic voltammetry and impedance spectroscopy) no significant differences were found [33].

Once the device was implanted, it was characterised by visual and electrical stimulation, and the stimulation selectivity was evaluated.
In the trait preceding the chiasm, the centre of the rabbit optic nerve is mostly composed of large diameter fibres than the periphery. Most of them decussate at the optic chiasm. For this reason, subjecting the rabbit to light stimuli, visually-evoked potentials (VEPs) were recorded mainly for contralateral stimulation with values comparable to those present in the literature.
Regarding electrical stimulation, an ECoG array was implanted in the contralateral part of the cortex for recording electrically-evoked potentials (EEPs). An asymmetric cathodic 1:5 stimulation with a pulse train frequency of 1 kHz was applied to have a good efficiency.

This frequency is chosen taking into account the frequency of the action potentials generated by the Retinal Ganglion Cells (RGCs) (a few hundred hertz) to reproduce the natural code. The modulation of the number of pulses allows the cortical activation to be varied. Furthermore, due to the conformation of the nerve and the arrangement of the fibres, the electrodes on the wings have a lower stimulation threshold than those in the main body because they are in contact with fibres of small diameter [33].

Overall, analysing the activation map, the electrodes in contact with both the central and peripheral parts of the nerve can stimulate different fibres, thanks to the 3D configuration, guaranteeing good selectivity and stability [34].

1.9 Soft biomaterials

The biomaterials used for manufacturing the implant are a crucial aspect that must be considered to avoid the foreign body reaction and, therefore, the subsequent clinical failure of the device. The mechanical symbiosis between implant and host tissue is critical to achieve, so it is important to analyse which material is most compliant with neural tissue in order to not be rejected by the body. For this purpose, soft materials are used for creating a device conformed to the dynamics of neural tissue. They make the device stretchable, able to reversibly expand and relax like host tissue [35].

The material commonly used for implants is **polydimethylsiloxane** (PDMS). Its flexibility allows electrodes to be bent and stretched thousands of times without electrical failure of the device [36]. PDMS is a low-cost elastomer with a Young modulus of few MPa (about 6.7 MPa), chemically inert, thermally stable, and oxidation-resistant [37]. It is a biocompatible polymer of the siloxane family [38, 39]. The mechanical properties strongly depend on the thickness of the layer, only if it is smaller than 200 μm, and on the curing temperature. The thickness-dependent trend is mainly due to the reorganisation of polymer chains during its curing and to the the formation of the cross-links [40]. On the other hand, one of its main problems is the sophisticated fabrication techniques needed to pattern it.

The **polyimide** also known as PI is a polymer currently widely used as both structural and insulating material due to its flexibility and biocompatibility. The main advantages are the high resistance to solvents which makes it suitable for encapsulation, the capability to be processed using standard microfabrication techniques and its good adhesion to metal oxide [15]. The polymer is characterised by the imide functional group (CO-NR_2), therefore the π electrons presence makes it resistant to solvents and moisture [37]. The preparation process consists of the reaction between diamines and dianhydrides, whose structures influence the polymer final properties. Furthermore, these monomers play a fundamental role in determining its Tg [41]. It is characterised by low stress (2 MPa for 10 μm thick film), high storage modulus (8.5 GPa), a Poisson ratio of 0.4, a high Tg (360 °C) and guarantees good dielectric properties (2.9 dielectric constant) [42]. One of its main disadvantages is its high Young's module that makes the implant stiff and, therefore, unsuitable for long-term implants [17].

Another material of great interest that can be used for neural probes is **OSTE+**, a photopatternable polymer with tunable mechanical properties based on the off-stoichiometric thiol-ene epoxies. The manufacturing process consists of two curing steps: radical polymerization and anionic polymerization.
The radical polymerization, triggered by the photoinitiator plus UV illumination, consists of the reaction between the thiol groups (-SH) and the ene groups of the monomers. Polymerization takes place after the UV exposure of prepolymer mixture, poured in a mould

or coated onto a wafer. It ends with recombination reactions among radicals. If the ratio between thiol groups and ene groups is the same, one talks about stoichiometry in which there are no reactive group remained, and so it is necessary to use plasma activation to have reactive surface. Instead, it is defined as off-stoichiometry if the ratio between functional groups is different. This ratio is important because it influences the final mechanical properties of the polymer without changing the composition of monomers. In this latter situation, unreacted groups are regularly distributed on the surface and in bulk. Therefore, an UV-illumination can induce click reactions of thiol-ene in which other functional monomers graft by covalent bonds. Thereby, a surface modification is carried out by dry-bonding without the need for heat treatments, plasma treatments or solvents application that could induce deformations. This property can also be used for varying the surface wetting. Regarding neural prostheses, it is taken advantage to perform electrode encapsulation through the photolithography technique [43, 44].
As for the second curing step, the anionic polymerization consists of the reaction between the excess of the unreacted thiol groups of the previous step and the epoxy resin, that bind at room temperature. This stage is the so-called thiol-epoxy reaction. The resins have good mechanical properties and good chemical resistance. A different wavelength of UV light is used for activating this second step thanks to a photobase presence. Thereby, it allows greater control and separation of the two polymerizations [44].

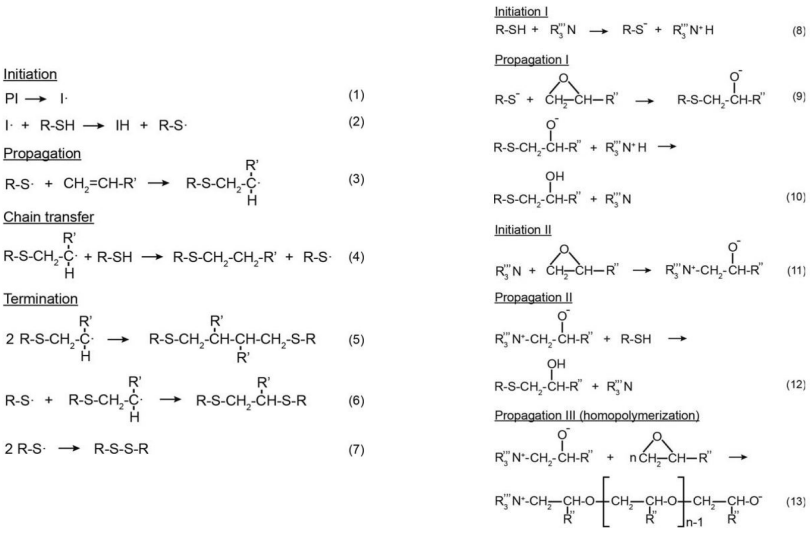

Figure 1.16: Main steps of the radical polymeritazion between thiol and ene groups (*left*), and of the anionic polymeritazion between thiol groups and epoxy resin (*right*). *From Carlborg et al.*

At the end of the last curing step, the surface loses the reactivity that it had after the first curing step. Moreover, the mechanical properties are little influenced by the relationship between thiol-epoxy and thiol-ene, not bringing significant variations even for Tg, as can be seen in Figure 1.18.
It has been shown by Ejserholm et al. that the dilution of OSTE+ in water for 7 days reduces toxicity and has no negative effects on cell proliferation. Instead, if an OSTE+ specimen is implanted without washing with water, it can be toxic even not showing any morphological changes. The number of viable cells is reduced by rising the concentration of the assay, i.e. it increases the toxicity mainly due to the presence of the impurities. Furthermore, the use of purer chemicals during fabrication minimizes the toxicity of an implant made in OSTE+ rather than in other polymers [45].

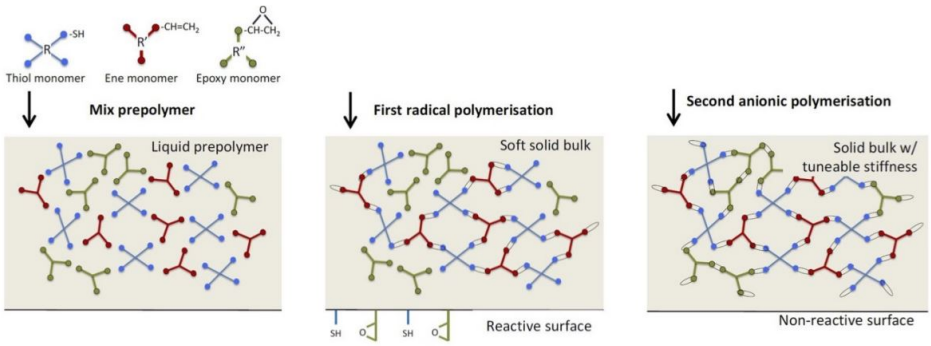

Figure 1.17: Overview of two polymerisation. After the prepolymer mix, first radical polymerisation is followed by a second anionic one. *From Borda E.*

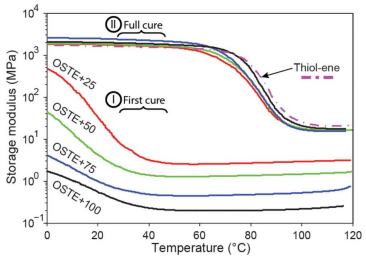

Samples within 5 h after first cure				
Formulation	Storage Modulus at 25 °C (MPa)	n^a	T_g (°C)^b	n
OSTE + 25	14 ± 1	3	23 ± 1	3
OSTE + 50	3 ± 0.2	3	11 ± 2	3
OSTE + 75	0.8 ± 0.1	3	N/A	N/A
OSTE + 100	0.4 ± 0.1	3	N/A	N/A
Samples after full cure				
Formulation	Storage modulus at 25 °C (MPa)	n	T_g (°C)	n
OSTE + 25	1700 ± 50	3	86 ± 1	3
OSTE + 50	1800 ± 200	3	87 ± 1	3
OSTE + 75	2400 ± 430	3	86 ± 4	3
OSTE + 100	2000 ± 140	3	87 ± 1	3
Thiol-ene	1600 ± 150	3	90 ± 2	3

Figure 1.18: Averaged Storage modulus and Tg of OSTE+ with different thiol-ene ratio after the first and the full curing. After the full curing, mechanical properties are little influenced by thiol-epoxy and thiol-ene ratio. *Modified from Carlborg et al.*

1.10 Optic nerve phantom

The purpose of the phantom's realisation is to use it as a substitute for human/animal parts or organs that can be employed to optimise prosthesis design, to mechanically test the device or in training purpose. In this case, to facilitate the fabrication of the phantom adequately to its main goal, a simplified model of optic nerve was used. It consists of a neural tissue made up of axons bundles surrounded by a thin layer of pia mater. In agreement with what was done by Shin et al., due to the difficulty in mechanical characterisation of the intrinsic connective tissue linked with the pia mater, two total Young modulus for the optic nerve and the pia mater were taken into account [46]. Specifically, the optic nerve was considered to be a composite material with 0.03 MPa of elastic modulus surrounded by 60 μm thick pia mater with an elastic modulus of 3 MPa [46, 47]. The mechanical properties of neural tissue and pia mater, as well as the sclera and lamina cribrosa that characterise the optic nerve head of several living beings, have been analysed by many authors, as can be seen in Figure 1.19 [48].
The mechanical properties of the rabbit optic nerve are similar to human ones [49]. In normal conditions, the nerve has fibres arranged parallel and evenly distributed. In pathological situations, instead, they organise themselves in a disorderly and irregular way, varying both mechanical and morphological properties.
The common materials used for the fabrication of the neural tissues phantom are reported below with their main mechanical properties.

The **gel wax** is a material used for the realisation of the nerve and vessel phantom. Its main

Tissue/Species	Author(s)	Young's Modulus (MPa)
Sclera		
Tree Shrew	Phillips and McBrien[23]	2.28
Tree Shrew	Siegwart and Norton[24]	0.69–18.3
Bovine	Smolek[25]	3.8–9.0
Human	Woo et al.[26]	5.5
Human	Friberg and Lace[27]	1.8–2.9
Monkey	Downs et al.[28]	2.9–5.5
Porcine	Spörl E, et al. *IOVS* 2003;44:ARVO E-Abstract 3318	0.3
Human	Battaglioli and Kamm[29]	4.76
Human	Kobayashi et al.[30]	5.5
Neural tissue		
Porcine brain	Miller[31]	0.03
Bovine brain	Guillaume et al.[32]	0.046
Monkey brain	Merz et al.[33]	0.010
Bovine retina	Jones et al.[34]	0.020
Cat spinal cord	Chang et al.[35]	0.2–0.6
Rabbit spinal cord	Ozawa et al.[36]	0.035
Lamina cribrosa		
Porcine	Spörl E, et al. *IOVS* 2003;44:ARVO E-Abstract 3318	0.1
Fit to human	Edwards and Good[6]	0.14–0.38
Monkey	Bellezza et al.[37]	0.077–0.405
Pia mater		
Human	Zhivoderov et al.*[38]	1.44–4.65
Human	Our computations based on measurements by Mazuchowski and Thibault[39]	2.5–65
Human	Brands[40]	1.86 (Shear modulus)

Figure 1.19: Summary of Young Modulus of optic nerve tissue for different species and the respective authors. *From Sigal et al.*

application field is about ultrasound analysis thanks to its tunable properties. The elastic modulus of the native material is 17.4 ± 1.4 kPa and is characterised by a stress-strain curve whose trend is linear for deformations less than 40% and non-linear for greater ones. Concerning the fabrication procedure, the gel is dissolved at about 95 °C and, then, added 2 w/w% glass spheres and 5 w/w% paraffin wax, used for improving the acoustic properties. After 30 s sonication and 2 min degassed, the substance is poured into 2.5 mm radius cylindrical moulds made with the 3D printer [50].

Other usual materials, especially for the brain phantom fabrication, are agarose (0.6%), gelatin gel and agar [51, 52, 53]. The brain, however, is characterised by lower mechanical parameters than the optic nerve. Nevertheless, it is possible to vary the **agarose** concentration to mimic the optic nerve properties. Increasing the agarose concentration, the cross-links distance is reduced and, therefore, it rises shear stress, viscosity, stiffness, and Young's modulus [53, 54]. According to the Pearson and Graessley model, the relation (Equation 1.1):

$$E \propto \frac{\lambda - \mu}{N} RT[agarose] \tag{1.1}$$

shows that the elastic modulus E is proportional to the agarose concentration and it also depends on the number of chains (N), the gas constant (R), the temperature (T), the number of stands (λ) and cross-links (μ) [55]. The elastic modulus, strain and stress values over concentration and viscosity are reported in Figure 1.20 [55].
Not only its concentration but also the thermal history and the cooling rate influence the final mechanical properties. After cooling down to room temperature, if it is kept at 37 °C overnight, it has an equilibrium stress lower than if the material is left at 25 °C overnight at the same concentration [56]. The hydrogel fabrication technique consists in dissolving the agarose and the buffer (tris/ borate/EDTA buffer), heating them to a temperature around 90 °C and, in the meantime, mixing them to guarantee the solution homogeneity. For high concentrations, greater than 10%, it is advisable to heat the solution under vacuum for several hours to avoid the formation of the bubbles and to make it homogeneous [57, 55]. Regarding the realisation of the phantom with dimensions similar to the nerve, the solution can be poured in stainless still cylindrical moulds with a specific diameter or

[agarose] $\times 10^4$ (mol·L^{-1})	% (w/w)	tension modulus (KPa)	compression modulus (KPa)
1.08	1.0	83.7 ± 15.2	76.0 ± 8
1.63	1.5	184.8 ± 18.6	-
2.18	2.0	288.5 ± 38.6	235.0 ± 28
2.73	2.5	451 ± 48.4	-
3.31	3.0	629.0 " 88.0	516.0 ± 48

(a) *Elastic Moduli for high viscosity agarose*

[agarose] $\times 10^4$ (mol·L^{-1})	% (w/w)	tension modulus (KPa)	compression modulus (KPa)
0.48	0.30		1.5 ± 0.7
0.79	0.50		5.3 ± 0.25
1.12	0.70		14 ± 1
1.60	1.00		38 ± 2
4.06	2.50	435 ± 23	254 ± 20
8.33	5.00	1340 ± 121	929 ± 48
12.84	7.50	2450 ± 46	1900 ± 230
17.59	10.0	3690 ± 60	2580 ± 225

(b) *Elastic Moduli for low viscosity agarose*

[agarose]		tension		compression	
		failure		failure	
$\times 10^4$ (mol·L^{-1})	% (w/w)	stress (KPa)	failure strain	stress (KPa)	failure strain
1.07	1.0	48 ± 8	0.208 ± 0.025	55 ± 3	0.43 ± 0.015
2.16	2.0	126 ± 13	0.209 ± 0.017	129 ± 10	0.44 ± 0.026
3.31	3.0	227 ± 22	0.213 ± 0.019	225 ± 12	0.43 ± 0.028

(c) *Stress and Strain for high viscosity agarose*

[agarose]		tension		compression	
		failure		failure	
$\times 10^4$ (mol·L^{-1})	% (w/w)	stress (KPa)	failure strain	stress (KPa)	failure strain
4.06	2.50	77.7 ± 15	0.143 ± 0.01	104 ± 6	0.36 ± 0.02
8.33	5.00	214 ± 26	0.142 ± 0.01	280 ± 31	0.33 ± 0.02
12.84	4.50	302 ± 11	0.11 ± 0.002	488 ± 27	0.378 ± 0.006
17.59	10.0	453 ± 20	0.12 ± 0.01	606 ± 53	0.36 ± 0.01

(d) *Stress and Strain for low viscosity agarose*

Figure 1.20: Elastic modulus, strain and stress values over concentration (from 0.3% to 10%) and viscosity (low and high viscosity), measured in tension and compression conditions. *Modified from Normand et al.*

in syringes that are then cut to obtain the desired size. It is possible to cover the mould walls with vaseline to prevent the agarose from sticking to them. In this way, it is facilitated the removal of the phantom once it has solidified [55].

2 Main Goals

The main goal of this project is based on the optimisation of the device structure, realised by Gaillet et al., to make the OpticSELINE more compliant with neural tissue. To do so, a first significant change concerns the variation of the substrate material: the use of soft and stretchy off-stoichiometric thiol-ene epoxy thermosets (OSTE+) in place of the flexible polyimide. Thanks to OSTE+ tunable properties, it is possible to vary the stoichiometry of its monomers to decrease Young's modulus from a few GPa to tens of MPa, comparable to the nervous tissues one [58]. In this way, the replacement of the PI with OSTE+ could improve the long-term stability and increase the biointegration of the device. Besides, OSTE+ is preferred to PDMS, which is the polymer most widely used for the fabrication of soft and stretchable implants. It is characterised, in fact, by a Young's modulus of hundreds of kPa - few MPa [38]. However, one of the main reasons for not using PDMS is the need for more complicated fabrication techniques for encapsulation [37]. OSTE+, by contrast, is a photopatternable polymer, and so it is suitable also for encapsulation.

The principal tasks required and developed in this thesis are:

- Optimisation of the OpticSELINE design in terms of geometry and size to realise it in OSTE+. To do so, finite element analysis (FEA) is performed to evaluate the stress distribution and the possible deformations to which the device is subjected.
- Optimisation of the process flow to fabricate the OpticSELINE structure in OSTE+.
- Realisation of the metallic mould to perform the thermal treatment for wings memorization. In this way, a more reliable reproduction of the wings is expected.
- Optimisation of the set-up used during the mechanical tests, i.e insertion and extraction of the device in/from the optic nerve. This set up keeps the nerve in tension for a correct forces analysis during these tests. Thereby, a good evaluation of the device compatibility with insertion forces and the interface anchoring can be done.
- Perform mechanical insertion and extraction tests with rabbit optic nerves in ex-vivo, according to what described by Gaillet et al., to understand the effect of the device on the nerve, to evaluate possible failures during penetration and to analyse the design effectiveness.
- Realisation of a possible nerve phantom to substitute the fresh optic nerve during the mechanical tests performed for the device optimisation. In this way, one avoids the use of ex-vivo optic nerves. This requires an analysis of the anatomy and mechanical characteristics of the optic nerve to identify one or more combinations of materials and a method to reproduce the nerve's shape and size.

3 Materials

3.1 Substrate materials

The present section illustrates the main materials which have been used for the fabrication of the implant substrate.

3.1.1 Polyimide

The polymer generally used is PI-2611 (HD MicroSystems) whose precursors are biphenyldianhydride and 1,4 phenylenediamine. The polyamic acid precursor is provided and it must be cured to obtain a fully aromatic PI film. In this case, the 12.5 μm thick polyimide film (50HN Kapton) supplied by Lohmann is utilised to speed up the manufacture of the OpticSELINE specimens (without electrodes and connections) in order to assess their mechanical behaviour during insertion/extraction tests.

3.1.2 OSTE+

The OSTE+, supplied by Mercene Labs AB, requires a preparation process in which Pentaerythritol tetrakis (3-mercaptopropionate), component A with thiol groups, and 1,3,5-Triallyl-1,3,5-triazine-2,4,6(1H,3H,5H)-trione, component B with allyl group, the epoxy resin, a base catalyst and a photoinitiator, must be mixed.
The two types of OSTE+ used are:

1. OSTEMER 322 Crystal Clear (OSTE+ CC), with an A:B ratio of 1.09:1;

2. OSTEMER 324 Flex (OSTE+ Flex), with an A:B ratio of 1.24:1.

They differ in the ratio of the two components and, therefore, have different mechanical properties. As for OSTE+ Flex, it is more flexible than OSTE+ CC, has a uniform elastic behaviour and it suitable for integrating electronic components. It is also used for encapsulation thanks to its lower exposure dose required during direct writing photolithography unlike OSTE+ CC. OSTE+ CC, in contrast, is characterised by elastic and plastic deformation and, therefore, it is suitable for wings memorization. Overall, as far as the mechanical aspect is concerned, OSTE+ CC could be considered similar to PI, while OSTE+ Flex could be comparable to PDMS.

3.2 Masks materials

The main materials used for realising the different masks for photolithography are:

- polyethylene terephthalate (PET) film, 23 μm thick, supplied by Lohmann. This film is UV-light transparent and, so, it is used as mask support, on which metal (Pt or Ti) has been sputtered or black PDMS spin-coated.
- polydimethylsiloxane (PDMS) (Sylgard 184) supplied by DOW. The fabrication process consists of mixing two parts, a base (component A) and a curing agent (component B). It is used for its transparent optical properties at a wavelength less than 250 nm [38].
- carbon black microparticles (Norit Activated Carbon Ultra E153), supplied by Cabot, 100% natural origin for use as a colour additive. Carbon black microparticles are mixed with PDMS to realise black PDMS, flexible and able to absorb UV-light, thanks to the particles average Relative Coloring Power (RCP) of 75 ± 5 [59].

3.3 Phantom materials

The materials used for fabricating optic nerve phantom are:

- agarose (Agarose Standard supplied by ROTH), which is a viscoelastic polysaccharide composed of two basic units: β-1,3 linked D-galactose and α-1,4 linked 3,6-anhydro-αL-galactose.
- PDMS (Sylgard 184) supplied by DOW, obtained by mixing the base with the curing agent.

4 Methods

4.1 Mechanical properties of OSTE+

A series of tensile tests were performed at the MTS machine for a more in-depth analysis of the mechanical properties of OSTE+. The tests were carried out on specimens of OSTE+ Flex and OSTE+ CC manufactured with different fabrication steps and parameters in order to optimise and standardise the fabrication process. Samples were fabricated in block in agreement with the main process flow reported in Section 4.3. The dog-bone specimens dimensions were in accord to the American Society for Testing and Materials (ASTM) standards: 30.6 mm in overall length with 10.1 mm for reduced section, 4.9 mm in width of grip section, 0.9 mm in width of reduced section and 4.2 mm of fillet radius. Specimens thickness depend on the value of spin coating speed. Once we fabricated them, they were tested with MTS machine from LSBI Laboratory. A 10 N load cell was used and the speed was set to 1% of the original gauge length (L_0), evaluated before the tensile test. The estimated parameters are Young modulus, maximum stress and maximum strain, calculated using Matlab software. The strain was determined by specimens elongation as Equation 4.1:

$$\varepsilon = \frac{\Delta L}{L_0} = \frac{L - L_0}{L_0} \tag{4.1}$$

where L is the final length and L_0 is the initial specimen length.
The stress was evaluated using Equation 4.2:

$$\sigma = \frac{Fn}{A} \tag{4.2}$$

where Fn is the normal force and A is the specimen nominal cross-section. A stress-strain curve was estimated by these two parameters.
The Young modulus, which indicates the material stiffness, was calculated in accord with Hooke's law as described in Equation 4.3:

$$E = \frac{\Delta\sigma}{\Delta\varepsilon} \tag{4.3}$$

This value represents the slope of a stress-strain curve in the linear range in which stress is proportional to strain. For this reason, it was estimated in the strain range of 0.1 – 0.5% for OSTE+ CC specimens and in the strain range of 20 – 35% for OSTE+ Flex specimens. Tests are performed at room temperature.
The different processes analysed for OSTE+ Flex are reported in Table 4.1. Note that each layer is 30 μm thick (1000 rpm spin-coated) and if not specified, the wafer is not cooled down to room temperature.

	First layer		Second layer	
#	1° curing	2° curing	1° curing	2° curing
Wafer1	2 min UV box	/	2 min UV box	overnight at 100 °C
Wafer2	2 min UV box	overnight 100 °C	2 min UV box	overnight at 100 °C
Wafer3	2 min UV box	2 days at 100 °C		
Wafer4	3 min UV box	14 h at 100 °C + cooling		

Table 4.1: Characterisation of fabrication process of OSTE+ Flex specimens, with single or double layers. Each layer is 30 μm thick.

The tests performed for OSTE+ CC are reported in Table 4.2. Also, in this case, each layer is 30 μm thick (1000 rpm spin-coated). If not specified, the second curing doesn't have a cooling step.

	First layer		Second layer	
#	1° curing	2° curing	1° curing	2° curing
Wafer1	6 min MJB4	/	6 min MJB4	overnight at 100 °C
Wafer2	6 min MJB4	overnight 100 °C	6 min MJB4	overnight at 100 °C
Wafer3	12 min MJB4	overnight at 100 °C		
Wafer4	5 min UV box	2 days at 100 °C		
Wafer5	6 min MJB4	14 h at 100 °C + cooling		
Wafer6	5 min UV box	14 h at 100 °C + cooling		
Wafer7	7 min UV box	14 h at 100 °C + cooling		

Table 4.2: Characterisation of fabrication process of OSTE+ CC specimens, with single or double layers. Each layer is 30 μm thick.

These several trials can underline the influence of baking and UV exposure.
The last tests have been carried out on a sample composed of two layers of OSTE+ Flex and a single non-patterned layer of OSTE+ CC. The first and the third layers of OSTE+ Flex is cured 2 min UV box and then at 100 °C overnight, while the second layer of OSTE+ CC is cured 120 s MJB4 and then at 100 °C overnight. In this process, that allows us to have an idea of mechanical characterisation of three layers sandwich, each layer is about 5 μm thick (3000 rpm spin coating).

4.2 Optimisation of OpticSELINE design

Starting from the first version of OpticSELINE developed by Gaillet et al. and described in Section 1.8, two modified versions of the device substrate have been implemented, one 1.1 times bigger in width than the original version, here referred to as "Design 1", and one 1.86 times bigger in width, referred to as "Design 2". Devices with both two designs have been produced in OSTE+ and PI, whose process flows are described in Section 4.3. The purpose of PI samples is to compare their mechanical performances with those of OSTE+, material of interest in this project. The use of a soft and stretchy material such as OSTE+ rather than PI is due to the desire to create increasingly compliant devices. Initially, the substrate made in OSTE+ CC has been fabricated and analysed, because it is more similar to the PI for its mechanical properties. Subsequently, a softer substrate consisting of three sandwiched layers has been tested. This is characterised by a bottom and a top layer in

OSTE+ Flex and a middle patterned layer in OSTE+ CC. The role of this patterned layer is to reinforce the wings and to plastically deform them in an open configuration, that it is impossible to achieve with OSTE+ Flex-only substrate. A thermal treatment has been carried out to memorize the wings through an analogues strategy to that described by Gaillet et al. In this case, a specific mould, discussed in detail in Section 4.6, has been used.

Moreover, the use of OSTE+ requires some structural variations compared with the PI version of Gaillet et al. First of all, the thickness of the substrate has been increased from 12 μm in PI to 30 μm in OSTE+. The total size for both designs is 4 mm in width and about 37 mm in length, including the area to connect the electrodes to the head plug connector that is, instead, about 10 mm wide.
The width of the active area (the region where the wings are located) has been slightly enlarged from 0.43 to 0.49 mm for Design 1, compared with the current version in PI. Its length is the same as the current version, equal to 1.39 mm in accord to the diameter of the rabbit optic nerve of 1.5 mm. As for Design 2, the active area width has been increased to 0.8 mm. This enlargement has been selected after different insertion tests performed on ex-vivo nerve with different active area widths (0.48, 0.67, 0.73, 0.8 and 1.075 mm).
The size of the wings has been chosen to take into account the size of the traces (15 μm) and their distance (20 μm) to avoid cross-talk. A trade-off of all these parameters has allowed us to introduce eight electrodes (about 80 μm in diameter) per side. Wings are 0.185 mm wide, 0.48 mm long and are 0.43 mm apart for the Design 1, while they are 0.36 wide and 0.48 long with the same distance between them for Design 2.
The dimension of the tip has been reduced from 0.29 mm to 0.14 mm for both versions. The section between the tip and the active area has been modified. A pronounced slope has been introduced to gradually increase the hole diameter of the nerve, previously made by suture needle. Metal reinforcements in platinum, 100 nm thick, have been placed between the tip and the active area to ensure the insertion and to prevent undesired deformations for OSTE+ substrate. The three types of metal reinforcements, assessed by FE simulations and tested in ex-vivo, are (1) the central holes surrounded by a sputtered metal, (2) the metallized tip and (3) the addition of metallic transversal bars.
Four alignment bars, 0.1 mm wide and made of Pt, have been added per each side to guide the insertion, ensuring the placement of active sites within the nerve.

4.2.1 Finite element analysis

The purpose of FE analysis is to model the insertion of OpticSELINE and to evaluate the maximum force, that one could apply without breaking the device. FE simulations have been performed on two different sizes of device (Design 1 and Design 2) and compared with the current version. Two different values of thickness (30 μm and 15 μm) have been considered for OSTE+ substrate, while a thickness of 12 μm has been used for the PI model.

The model consists of half electrode, from tip to active area, characterised by a principal body with two holes that correspond to the empty region where the flats are attached. The thickness of the model is double to simulate the closed-loop configuration. The material properties used for substrate model are 8 GPa of Young's modulus, 0.4 of Poisson ratio and 350 MPa of maximum tensile stress for PI, and 30 MPa of Young's modulus, 0.4 of Poisson ratio and 15 MPa of maximum tensile stress for OSTE+. About metal reinforcements for OSTE+ substrate, platinum has been considered for these simulations (Young's modulus of 168 GPa, maximum tensile strength of 205 MPa and Poisson ratio of 0.385 [60]).
The element type used for modelling the entire structure is PLANE82, an 8-node element with two degrees of freedom at each node. This element provides a mixed mesh suited to curved regions. The mesh has been made using 219 8-node elements. A plane stress analysis with thickness as input real constant has been carried out. This approximation is

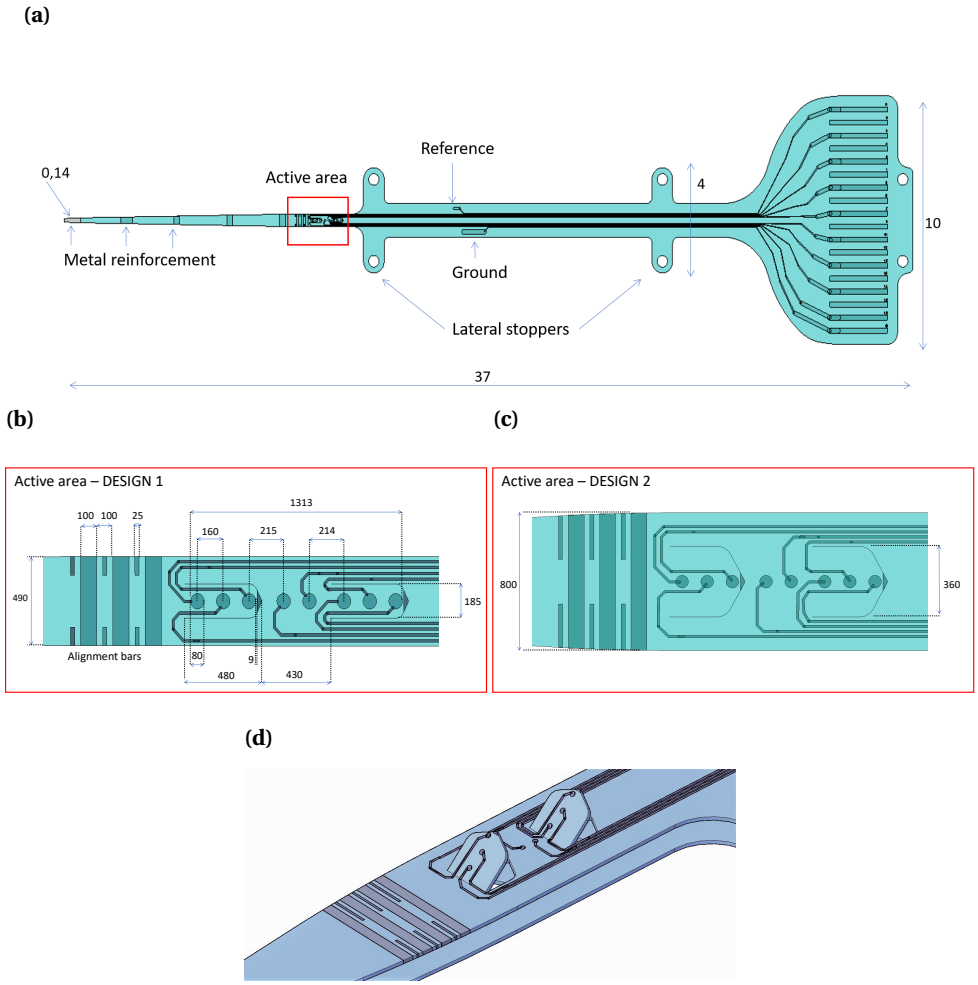

Figure 4.1: *(a)* Schematic AutoCAD drawing of OpticSELINE design with pads, electrodes and traces. Dimensions are in mm. Active area is enclosed in the red rectangle and it is characterised by two wings and eight electrodes. *(b-c)* Magnification of active area of Design 1 and Design 2 with metal bars for alignment during insertion. Dimensions are in μm. *(d)* Enlarged view of active area of Design 2 with wings, electrodes and metal bars after thermal treatment. Wings are opened 45° from the base.

possible because the thickness is too small than other dimensions and, therefore, it could be considered as a thin flat plate with load forces parallel to it. The main body is subjected to insertion force, applied to its tip, and lateral compression forces due to the contact of device's sides with internal wall of nerve hole, made previously by the needle. The insertion force has been approximated to a punctual one because of the too-small diameter of suture thread. The lateral forces have not been considered because of the size of the device tip, comparable to the hole, instead. Furthermore, they act mainly on the tips of the wings, which are not modelled, and on active area side. This region undergoes to minor stress than the tip because of its enlargement and, for this reason, these forces have been ignored. Moreover, the dynamic friction forces have been neglected due to the low speed with which the device is inserted into the nerve. The model has been constrained on the left side, the active area edge. An x-y constraint is applied in the middle node, while all other nodes have been blocked along the x-direction. As for OSTE+ substrate, at first, an insertion force of 400 mN has been imposed to determinate a better configuration of

metal reinforcements to prevent the device break. In this FE model, a 30 μm thickness has been considered. Afterwards, the maximum insertion force has been determined for both designs, 15 μm thick. As for PI, the maximum force has been evaluated for 12 μm thick model, in both designs. Von Mises stress and x displacement have been evaluated.

Figure 4.2: FE model for OpticSELINE analysis during insertion. The mesh element is PLANE82 (8-node element), the insertion concentrated force is 400 mN and the model is constrained along x-axis for all nodes and along y-axis for only middle node of the left side.

4.3 Fabrication

The fabrication of OpticSELINE in OSTE+, with and without electrodes, was carried out on a 100 mm diameter silicon wafer at the cleanroom of Campus Biotech. As for specimens in PI, only substrate has been analysed.
The parameter used for spin-coating and laser cutter, as well as the process flow steps, are reported in Appendices.

PI substrate

The 12.5 μm thick polyimide films (50HN Kapton) was used for speeding up the fabrication process of the only substrate. Then, the substrate was shaped by laser cutter (Optec MM 200-US) at Campus Biotech. Finally, samples were cleaned by Isopropanol and dried by nitrogen flow. The last step was the thermal treatment for wings memorization performed at 160 °C for 2 h in the oven.

OSTE+ CC substrate

The first step was to clean the wafer to remove both organic and inorganic impurities by oxygen plasma treatment (PCCE – RFG 13.56/300, supplied by Diener electronic). The recipe used was 0.2 mbar of pump-down pressure, O_2 gas injection for 10 s at 15 m^3/hr speed and 30 s at 87 W of plasma.
The second step was the spin-coating of PSS (supplied by Sigma Aldrich) at 2000 rpm and the following baking at 145 °C for 10 min. This layer was useful to allow the release of the device by DI at the end of the microfabrication process. The spin coater used was EL200 by Solarsemi.
The third step consisted of OSTE+ CC deposition. The component A was mixed with the component B in 1.09:1 ratio for at least 3 min by Thinky ARE 250. Then, the prepolymer was spin-coated at 1000 rpm (about 30 μm thick).
Once the mixed resin has been poured, the next step was the UV exposure at 365 nm in UV box (Gie-Tec by GmbH, intensity of 10 mW/cm^2) for 7 min. It takes about 1 min to reach this intensity value and, therefore, stabilise.
To conclude the polymerization of OSTE+, the second cure was a baking overnight (14 h at 100 °C plus cooling down to room temperature).
For metal reinforcement, 100 nm of Platinum were sputtered[1] on OSTE+ CC for 15 min

[1]The sputtering is a physical vapour deposition (PVD), which consists in evaporating a condensed material which comes back in a condensed state after deposition. In the sputtering chamber, there are the substrate and

at 100 W (ratio 6.4 nm/min), low stress and without Argon activation. The sputter used is AC450, supplied by Alliance Concept. In this step, a 50 μm thick PI mask (200HN Kapton, supplied by Lohmann) shaped at laser cutter was used.
Then, the substrate was shaped by laser cutting and removed from the wafer by PSS dissolution in DI. To guarantee the flatness of the device and to avoid possible bending of the lateral stoppers, the sample was located between two tissues with a weight placed on top until it was completely dry.
The last step was the thermal treatment for wings memorization that was performed at 40 °C for 5 h in the oven.

This process flow, without the Pt sputtering and the thermal memorization steps, is performed to fabricate specimens in OSTE+ CC and OSTE+ Flex for mechanical characterisation of the polymer. The specific parameters used are reported in Section 4.1.

Figure 4.3: Schematic cross-view of OSTE+ CC substrate after the release step. Pt is sputtered for metal reinforcement.

Three layers substrate

The process consists of creating three layers, two of them in OSTE+ Flex and a single patterned layer of OSTE+ CC in the middle as support for wings deformation.
The first two steps were the same as those described above. After the PSS spin-coating, OSTE+ Flex (1.24:1) was coated at 2500 rpm, UV cured for 2 min in UV box at 365 nm, baked at 100 °C for 14 h and cooled down to room temperature. The thickness was about 6-7 μm.
The second layer of OSTE+ CC (1.09:1), about 4-5 μm thick, was deposited at 3000 rpm. Before the photolithography[2], a 250 μm thick layer of PDMS was cast on uncured OSTE+ CC, which behaves as a negative photoresist. It was photo-patterned by MJB4 Mask aligner, from SUSS MicroTec, for 120 s (2 cycles of 60 s each) in hard contact mode[3]. This step is described in detail in Section 4.4. Then, it was developed[4] in Ethyl-l-lactate (≥ 99%; Sigma Aldrich) for 5 min at 70 rpm. During this step, PDMS film detached from the wafer. After rinsing in IPA to remove last unexposed material from wafer, a bake at 100 °C for 14 h plus cooling down to room temperature were performed.
The third layer was OSTE+ Flex coated at 1500 rpm, UV cured for 2 min in UV box, baked at 100 °C for 14 h and cooled down to room temperature. The thickness of the last layer

the target made of any material to deposit. An electrical field is applied between them to ionize the gas, generally Argon. The ions are accelerated to the target and detach target particles which deposit on the wafer [61].

[2]The photolithography technique transfers a geometric pattern from photomasks to a photo-sensitive film deposited on a wafer, known as photoresist. When it is exposed, UV light passes through the transparent regions of the photomask. After exposure, if the irradiated photoresist becomes soluble in the developer solution it is called positive, otherwise, if it is cross-linked, it is negative.

[3]In the hard contact mode, the photomask is brought into direct contact with the wafer, guaranteeing a high resolution but also possible damage to the mask. Other lithography modes are proximity lithography when there is a small gap between mask and photoresist that slightly decreases the resolution for light diffraction, and projection lithography when the pattern is projected onto resist thanks to a double lens system increasing the resolution.

[4]The photoresists development consists in removing the uncrosslinked regions. If the development time is too high, the structures can be damaged by the developer solution, reducing the adhesion. In contrast, if it is too short, some uncrosslinked material can remain on the wafer, reducing the resolution of features.

was about 20-21 μm.
As for metal reinforcement, 100 nm Pt was sputtered on third layer at 100 W for 15 min without Argon activation (AC450, Alliance Concept). Also, in this case, a 50 μm thick PI mask was used.
The device, about 30 μm thick, was shaped by laser cutter, released in DI and located between the tissues with a weight above to keep it flat during drying.
Finally, thermal treatment for wings memorization was performed at 40 °C overnight in the oven.

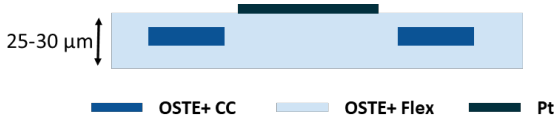

Figure 4.4: Schematic cross-view of three layers substrate, characterised by a first layer of OSTE+ Flex, a second patterned layer of OSTE+ CC and a third layer of OSTE+ Flex, after the release step. Pt is sputtered for metal reinforcement.

OpticSELINE in OSTE+

The process reported concerns the realisation of OpticSELINE with flat electrodes.
The first step was the fabrication of the OSTE+ CC or three-layer substrate, as described above. As for OSTE+ CC substrate, the prepolymer was spin-coated at 2000 rpm (about 15 μm thick), 7 min UV cured and baked at 100 °C for 14 h. As for the three-layer substrate, the first OSTE+ Flex layer was spin-coated at 2500 rpm (about 5 μm thick), 2 min UV cured and baked at 100 °C for 14 h. The second OSTE+ CC layer was coated at 3500 rpm (about 4 μm thick), patterned by MJB4 and baked at 100 °C for 14 h. The last OSTE+ Flex layer was deposited at 2000 rpm for a longer time than standard recipe used (about 10 μm thick) and full-cured like the first layer.
The patterning of electrodes, metal reinforcements and transversal bars to guide the insertion was performed by sputtering Pt onto the last layer using direct writing photolithography. Positive photoresist (AZ1512, 2.5 um thick) was coated and baked at 110°C for 2 min. After, it was cooled down to room temperature and patterned using MLA150 (Heidelberg Instruments). The wavelength was 405 nm and the exposure dose was 104 mJ/cm^2 dose. 100 nm thick Pt layer was sputtered for 15 min at 100 W low stress by AC450. Then, lift off was performed in PGMEA ($\geq$ 99.5%, supplied by Sigma Aldrich) with sonication bath at room temperature to remove the excess of Pt, followed by the rinse in DI and, then, in IPA. OSTE+ Flex was then spin-coated at 2500 rpm (5-6 μm thick) and patterned with MLA150 to realise the encapsulation. The wavelength was 375 nm and the exposure dose was 650 mJ/cm^2. The development in Ethyl-l-lactate for 4 min at 70 rpm and the rinse in IPA were performed. Then, the wafer was baked at 100 °C for 14 h and cooled down to room temperature.
The device was shaped at laser cutter and released from the wafer by PSS dissolution in DI. After the device was dried with weights placed on top, the thermal treatment was performed at 40 °C overnight for three layers substrate or 5 h at 40 °C for OSTE+ CC substrate.

4.4 Photolithography parameters and techniques

The principal goal is to fabricate a patterned flat layer of OSTE+ CC, between two layers of OSTE+ Flex. OSTE+ CC behaves as a negative photoresist. It was patterned by MJB4 Mask aligner from SUSS MicroTec at 365 nm UV light, 10 mW/cm^2 of intensity. Then, it

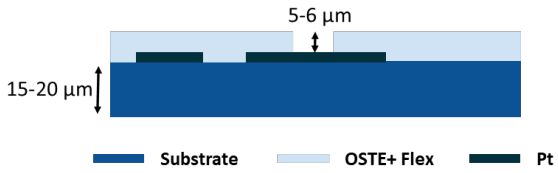

Figure 4.5: Schematic cross-view of OpticSELINE with electrodes and OSTE+ Flex encapsulation after the release step.

was developed in Ethyl-l-lactate, rinsed and baked at 100 °C.
To reach the main goal, several exposure techniques with different time exposure and photomasks, gathered in four groups, were tested (Figure 4.6).

The first tests group was performed on a single layer of OSTE+ CC spin-coated at 1000 rpm (about 30 μm thick). The exposure mode analysed was the soft contact mode with a chrome mask. The exposure parameters were 60 s of time exposure, 6 cycles, 10 s of wait time. The different techniques of this group were related to the presence or not of a PET film in addition to the chrome mask. PET film was cleaned by Isopropanol, dried by nitrogen flow and cast onto an OSTE+ CC layer before exposure. The effect to remove PET film before or during development was also tested. It is important to try to avoid air bubbles forming between OSTE+ CC and PET film. Moreover, uncured OSTE+ CC layer was very sticky and viscous, so the development time was increased from 5 to 10 min if the PET film was peeled off during development, and it was necessary to remove it very slowly to avoid damaging the small features. The exposure parameters were already optimised for 30 μm thick OSTE+ CC. The profile was measured with mechanical profilometer (DektakXT supplied by Bruker) and with optical profilometer (ContourGT Bruker).

In the second tests group, carried out on a single layer of 30 μm thick OSTE+ CC, the chrome photomask was substituted by a flexible one. It was directly located onto the OSTE+ CC layer and removed during development that lasted about 10 min. The exposure mode was the flood exposure while the exposure parameters were the same as the first group tests (60 s time exposure, 6 cycles, 10 s wait time).
The two types of flexible masks tested were:

1. PET film with UV-opaque material deposited above, in the regions not to be exposed to UV light. The pattern to transfer on the wafer, i.e. the wings, was shaped cutting the entire flexible mask by laser cutter. So, the light passes through the mask openings and the layer crosslinks. The masks tested were PET film with sputtered metal (Ti, Pt or Al) and PET film with coated black PDMS.

2. Full PET film and UV-opaque material deposited with a specific pattern. In this case, the light passes through the transparent regions of PET, where there is not UV-opaque material. The masks tested were PET film with open aluminium foil and three layers of full PET/black PDMS/open PET film.

In the third group of tests, the two mask typologies described above were used on a 5 μm thick OSTE+ CC layer, coated at 3000 rpm onto the first layer of OSTE+ Flex, 5 μm thick, already fully cured. In this way, it was possible to analyse the total performance. Furthermore, it has been observed that depositing 5 μm thick OSTE+ CC directly on Si wafer does not guarantee good adhesion of features during development, and this compromises the final profile. The exposure parameters have been changed because the thickness of the layer to exposure has been reduced from 30 μm to 5 μm. Therefore, an initial test was carried out for the assessment of the dose exposure. The total exposure time was in a range

# Test	Substrate	Exposure Parameters	Techniques	Development
1	30 µm OSTE+ CC	Soft Contact 60 s x 6 cycles + 10 s wait time	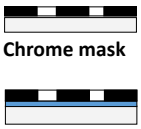	• 5 min without PET or PET removed before • 10 min to remove PET during development
2	30 µm OSTE+ CC	Flood Exposure 60 s x 6 cycles + 10 s wait time	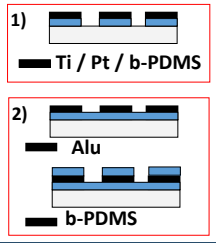	10 min to remove flexible mask during development
3	5 µm OSTE+ Flex + 5 µm OSTE+ CC	Flood Exposure 60 s x 2 cycles + 10 s wait time		
4	5 µm OSTE+ Flex + 5 µm OSTE+ CC	Hard Contact 60 s x 2 cycles + 10 s wait time	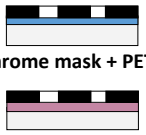	• 10 min to remove PET during development • 5 min to remove PDMS during development

Figure 4.6: Summary of the performed test groups with their respective exposure parameters, photomasks and development time.

of 80 – 140 s for 5 μm layers. The chosen exposure parameters are 60 s of exposure time, 2 cycles and 10 s of wait time.

After the best technique was chosen and the exposure parameters (60 s exposure time, 2 cycles and 10 s wait time) were defined, the last test group was carried out on 5 μm OSTE+ CC, coated on fully cured OSTE+ Flex. The exposure mode was hard contact with the chrome mask. The effect of using the PET or the PDMS film, cast on an OSTE+ CC layer and removed during development, was also evaluated. The development time was reduced from 10 min to 5 min in case of PDMS film.

4.4.1 Masks fabrication

Chrome mask

The chrome mask was composed of a glass substrate with a chrome layer on one side. Firstly, it was coated with anti-reflective and photosensitive resist. Then, it was patterned using a direct writing photolithography. Once it has been developed to dissolve the unexposed resist, it was etched to remove chrome parts selectively. The final step was the stripping of remaining resist, obtaining a chrome mask with glass pattern, covered by anti-reflective film.

PET/metal-based mask

The 23 μm thick PET was cast on a sticky glass wafer, i.e. a glass wafer with 50 μm 20:1 PDMS (Sylgard 184 supplied by DOW), coated at 1000 rpm and cured at 80 °C for 2 hours. It was laminated through a pouch laminator to remove trapped air bubbles that formed during the deposition of film onto the wafer. The temperature of the roller was about 100

°C, able to destroy small bubbles, and the speed was 6 mm/s. This process can be repeated several times to obtain a good result. The laminator system used was SKY-335R6. After, a metal (Ti or Pt) was sputtered on PET film. The recipe used for 250 nm Ti deposition was low stress sputtering at 150 W for 50 min (ratio 5 nm/min) without Argon activation. Instead, 250 nm Pt was sputtered at 100 W for about 40 min (ratio 6.3 nm/min) without Argon activation. Then, masks were shaped by laser cutting.

PET/black PDMS-based mask

The first step was the 23 μm thick PET lamination on a sticky glass wafer, as described above. Once the oxygen plasma treatment was performed (0.2 mbar of pump-down pressure, 30 s at 87 W of plasma), the second step was the black PDMS spin-coating at 1000 rpm and the following baking at 80 °C for 2 hours. To fabricate black PDMS, microparticles of carbon black (Cabot Norit 153) at 5% of concentration were used. The microparticles were mixed with hexane (Sigma Aldrich) to decrease carbon black's viscosity. After pouring PDMS-base into this solution, it was sonicated for 20 min at 30 °C by Branson model 5510 Ultrasonic cleaner, to make the blend uniform and to reduce lumps formation. The curing agent was poured in the blend and mixed for 3 min. The proportion of PDMS:curing agent:hexane for 5% of carbon black is 10:1:2. After spin-coating black PDMS onto PET film, it was cured at 80 °C for 2 hours and shaped by laser cutting.

PET/black PDMS/PET-based mask

This mask was characterised by PET/black PDMS based mask (described above) with a full PET film, 23 μm thick, laminated on it at 100 °C. Before the lamination, the oxygen plasma treatment was performed at 87 W.

PDMS film

After Si wafer was treated by oxygen plasma, PSS was spin-coated at 2000 rpm and baked at 145 °C for 10 min. This is a sacrificial layer to allow the release of the PDMS layer. PDMS 10:1 was mixed and spin-coated at 325 rpm to obtain a layer of about 250 μm thick. The wafer was baked at 100 °C for 15 min to increase the PDMS stiffness. The thickness of PDMS film was a good trade-off between the gap dimension that affects the resolution of features and its manageability. If the layer is too thin, it is difficult to cast it onto OSTE+ CC layer. Then, it was released from the wafer by PSS dissolution in DI water and dried by nitrogen flow.

4.5 Analysis of three layers profile and thermal memorization performance

The profile of the final three-layer substrate also must be flat to avoid problems during the electrodes' fabrication.

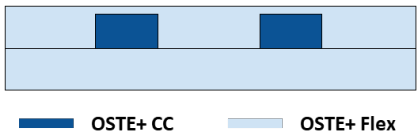

Figure 4.7: Cross-section of an ideal substrate characterised by two layers in OSTE+ Flex and a sandwiched patterned layer in OSTE+ CC.

Several tests were carried out changing the thickness of each layer. The entire profile of this

substrate was measured to assess its flatness. Then, the thermal treatment was performed to ensure that the wings remain in an open configuration. In this way, it is possible to evaluate if OSTE+ CC thickness is sufficient to memorize the open position of the wings. The main fabrication procedure was the same as that reported in Section 4.3, only spin-coating parameters were changed. The shape of the samples, cut by a laser cutter, has been simplified to a rectangular shape with two wings. The tests performed can be grouped into:

- For 5 μm thick OSTE+ CC layer (spin-coating at 3000 rpm), it was tested to spin-coat OSTE+ Flex at 2000 rpm, 1500 rpm and 1000 rpm, respectively from 5 μm to 30 μm of thickness.
- For 4 μm thick OSTE+ CC layer (3500 rpm spin-coating speed), it was tested to spin-coat OSTE+ Flex at 2000 rpm and 1500 rpm, respectively from about 10 μm to 20 μm.
- For 3 μm thick OSTE+ CC layer (4000 rpm spin-coating speed), it was tested to spin-coat OSTE+ Flex at 2000 rpm (10 μm thick).

In the 2000 rpm recipe of the two last tests, polymer is spin-coated for longer time than the standard recipe to uniformly distribute it onto OSTE+ CC layer. Recipes are reported in detail in Appendices.
The profile was measured by mechanical profilometer (DektakXT supplied by Bruker), optical profilometer (ContourGT Bruker) and scanning electron microscope (Hitachi SU5000). The thermal memorization was carried out in an oven at 40 °C overnight using a 3D printed mould. It was characterised by several blind holes with needles, inserted inside them to keep wings open, and steel washers to block specimens during the thermal treatment. A visual evaluation was performed to understand the minimum thickness of the OSTE+ CC layer able to perform the memorization.

4.6 Metallic mould

The main purpose of the metallic mould is to perform the wings memorization by thermal treatment, guaranteeing a reliable reproduction of the wings opening. This mould is used for specimens made both in OSTE+ and in PI.

The mould is composed of a base and a lid. The base is characterised by 5 mm deep blind holes inside which 0.4 mm diameter pins are inserted. They are located in correspondence with the lateral stoppers of device. Their role is to keep the specimen in place avoiding possible displacements during the thermal treatment. To support the wings in a 3D configuration, we constructed 0.2 mm diameter blind holes with the same depth (3.78 mm) placed at the wings tip, inside which 4 mm long cylindrical pins are glued. The pins used for wings support have the same nominal length equivalent to 45° of wings opening. The lid, instead, is characterised by 0.45 mm diameter cylindrical through-holes in correspondence with the lateral stoppers pins and by 0.7 mm diameter cylindrical through-holes in correspondence with the wings tip. It is essential to ensure that the specimen remains flat. The size of the mould is in accord with both versions of OpticSELINE design (Design 1 and Design 2). The mould is constructed at EPFL Atelier AT and the guaranteed tolerance is +0.005/+0.009 mm. As for the external pins, they are produced by UNIMED S.A and are:

- Stainless steel wire in AISI 304 with dimensions Ø (0.20 mm - 0.01 mm) x 4 mm ± 0.05 mm;
- Stainless steel wire in AISI 302 with dimensions Ø (0.40 mm - 0.015 mm) x 10 mm ± 0.2 mm.

The adhesive used to fix the cylindrical pins withstands temperature up to 175°C.

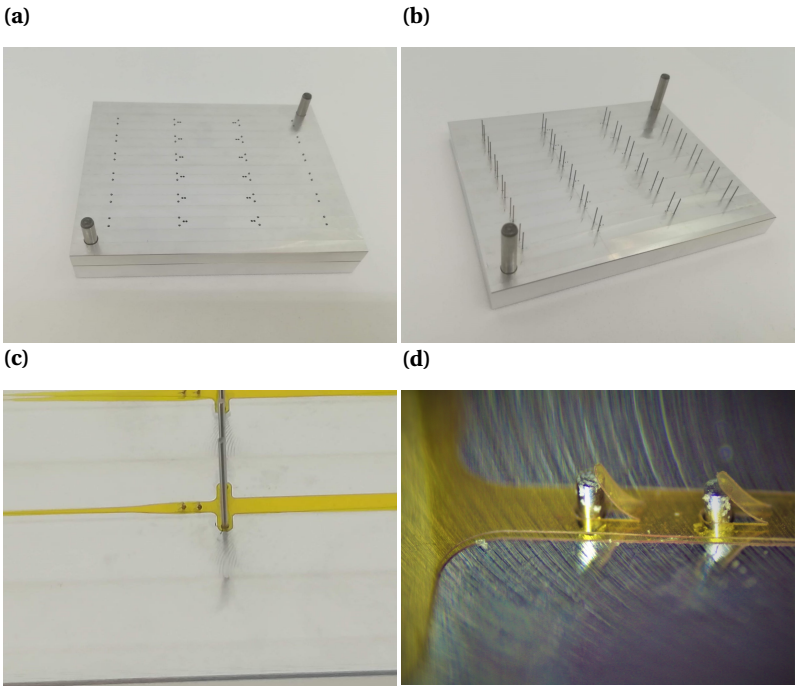

Figure 4.8: Metallic mould for wings thermal memorization. *(a)* Base and lid of the metallic mould. *(b)* Base and stainless steel wires to keep the device in place and to open the wings with a specific angle. *(c)* Magnification of mould with PI sample at the level of wings area. *(d)* Magnification of pins used for memorizing the open configuration of wings.

4.7 Setup for mechanical test

The mechanical setup is used for performing the mechanical tests of insertion and extraction like those carried out by Gaillet et al.
It is characterised by (Figure 4.9):

1. two 3D-printed supports;
2. one metal base with threaded through holes;
3. two metal clamps;
4. two needles.

The two supports were produced with Uprint Stratasys 3D printer at the Campus Biotech Mechanics Workshop. The material used is Acrylonitrile Butadiene Styrene (ABSplus), a high-performance thermoplastic material, very resistant with a Young's modulus of about 2.2 GPa and a glass transition temperature of 108 °C. The single support consists of a base (72 mm x 78 mm) with four through holes to screw it to the metal bar. Furthermore, it has a decentralised hole at 8 cm of height from the base used for screwing the clamp. The screws used are M6 (6 mm diameter) x 20 mm (length). The total height of support is about 114 mm. The metal bar (6 cm x 26.4 cm) is a solid and resistant steel structure used for fixing the two supports at the MTS machine base. It consists of a series of threaded through holes spaced to adjust the position of the two supports. The two metal clamps,

on the other hand, allow us to lock two needles inserted into the nerve to keep it in tension during the tests. The metal clamps are also supported and kept in place thanks to a small protrusion of the support.
The individual parts dimensions were chosen to keep the nerve in tension at about ten centimetres from the MTS machine base and in such a way that the axis of the nerve was perpendicular and central to load cell axis. Moreover, it was decided to fabricate two separate supports to eventually reuse them in other contexts, by adjusting their distance through the metal bar.

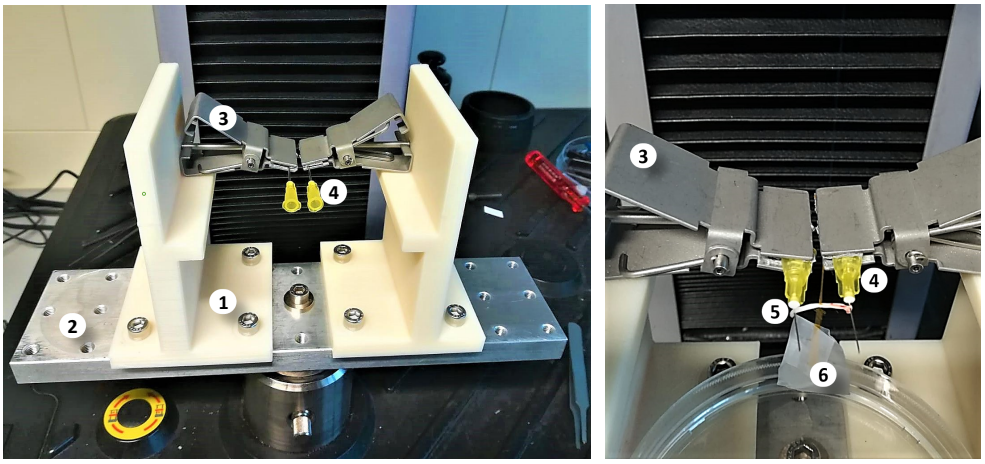

Figure 4.9: *(left)* Setup for mechanical tests of insertion and extraction. It consists of two ABS supports (1), a metal bar (2), two metal clamps (3) and two needles (4). *(right)* Magnification of setup with rabbit optic nerve (5) and OpticSELINE in PI (6).

4.8 Mechanical characterisation of OpticSELINE

The mechanical tests of insertion and extraction were carried out using the MTS machine of LSBI Laboratory at Campus Biotech, the explanted optic nerve of New Zealand White rabbits (> 16 weeks, > 2.5 kg) and the mechanical setup described in Section 4.7. The explanted nerves were harvested and stored at 8 °C in PBS (Phosphate-Buffered Saline) before the experiments and utilised within 12 – 14 days of explant.

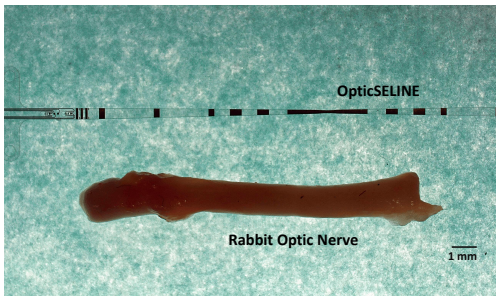

Figure 4.10: Optical microscope image of OpticSELINE (Design 1) in OSTE+ CC and rabbit optic nerve (diameter of 1.324 ± 0.046 mm).

Insertion Test

The specimens analysed were in PI, OSTE+ CC and three layers characterised by only substrate without electrodes. Both versions (Design 1 and Design 2) were evaluated. The tests were performed on six samples for each condition. The two main structures of the device were superimposed to perform the closed-loop configuration and fixed with adhesive tape at the lower ends to keep them in this configuration. The nerve was kept in tension thanks to mechanical support and was initially pierced by the suture needle (Prolene 10-0, GS-12 5.5 mm 3/8 curvature; Ethicon). After that, the device was inserted inside the nerve at a constant speed of 0.25 mm/s until all four alignment bars were visible. A 10 N load cell was used for measuring the insertion forces. The results were, then, analysed using Matlab software and the mean and standard deviation values of maximal insertion forces have been calculated.

Extraction Test

The experiments were performed on specimens in both versions (Design 1 and Design 2) made in PI, in OSTE+ CC and three layers without electrodes, only substrate. Three configurations per each substrate have been tested to assess the efficacy of the wings memorization during the device anchoring inside the nerve. The configurations are:

- No wings: device without wings like TIME;
- Non-memorized wings: device with wings in a passive configuration;
- Memorized wings: device with wings in an active configuration.

Five trials per each condition were tested.
Furthermore, the extraction tests were carried out on Design 1 in OSTE+ substrate (both OSTE+ CC and three layers) with flat electrodes and memorized wings (configuration of interest) to assess the extraction forces and, therefore, the anchoring of the device. Four trials were performed for each condition.
During these tests, the closed-loop device was initially inserted into the nerve and slightly pulled back as described by Cutrone et al. Once the device was inserted, it was extracted at a constant speed of 0.25 mm/s. Also, in this case, the extraction forces were measured by a 10 N load cell and examined with Matlab software. Mean and standard deviation values of maximal extraction forces have been calculated.

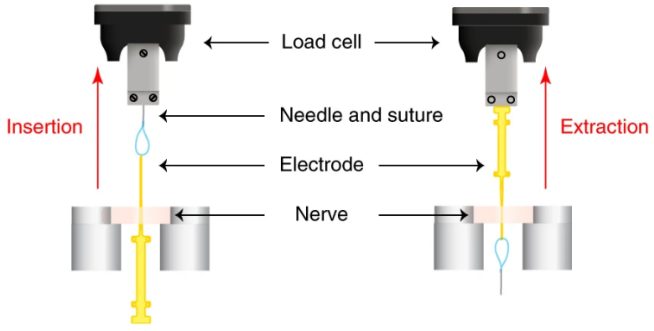

Figure 4.11: Representative scheme of mechanical test of insertion and extraction of OpticSELINE in/from explanted optic nerve of rabbit. *Image modified from Gaillet et al.*

Tensile test

Tensile tests were carried out on four samples in PI, OSTE+ CC and three-layer substrate to evaluate the mechanical performance and maximum force before breakage. MTS machine of LSBI was used. The device was closed in a loop that is the working configuration. The loop was inserted into a needle bent like a hook and attached to a 10 N load cell. The lower ends were fixed to a press linked to the MTS. The electrode was pulled at a constant speed of 0.25 mm/s until it was completely broken. The measured forces were, then, examined with Matlab software and the mean value and the standard deviation have been calculated.

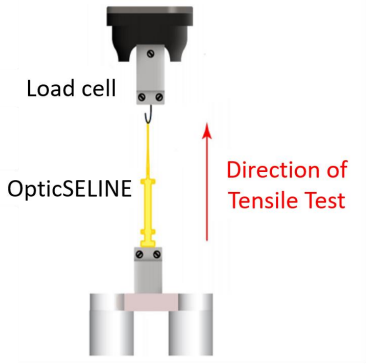

Figure 4.12: Scheme of tensile test of OpticSELINE until breakage. *Image modified from Gaillet et al.*

Test	Substrate	Design	Configuration	# Trail
Insertion	PI, OSTE+ CC, 3 Layers	Design 1 and Design 2 without electrodes	No wings	6
Extraction	PI, OSTE+ CC, 3 Layers	Design 1 and Design 2 without electrodes	No wings, non-memorized and memorized wings	5
	OSTE+ CC, 3 Layers	Design 1 with electrodes	Memorized wings	4
Tensile	PI	Design 1 without electrodes	Memorized wings	4
	OSTE+ CC, 3 Layers	Design 1 with electrodes		

Table 4.3: Summary of mechanical tests (insertion, extraction and tensile tests) performed on different configurations. Tipology of substrate, design, configuration and number of trial are reported.

4.9 Optic nerve phantom

Analysing the main materials used for phantom fabrication and comparing their mechanical properties with rabbit optic nerve ones, whose characteristics are summarised in Table 4.5 and in Table 4.6, it is possible to mimic the optic nerve internal tissue with 1-1.5% agarose or gel wax with the addition of glass spheres and paraffin, while one can use the 50 μm thick PDMS or 10% - 15% agarose to mimic the pia mater.

	Young Modulus (kPa)	Poisson Ratio
Neural Tissue	10 - 90	0.49
Pia Mater	1000 - 9000	0.49

Table 4.4: Young modulus and Poisson ratio of neural tissue and pia mater. *From Sigal*

Substitute Material for Neural Tissue		
	Young Modulus (kPa)	**Poisson Ratio**
Agarose 1-1.5%	20 - 60	0.5
Gel Wax	18 - 22	-

Table 4.5: Young modulus and Poisson ratio of possible substitute materials of neural tissue: 1-1.5% agarose and gel wax with the addition of 2w/w% glass spheres and 5w/w% paraffin. *From Maneas et al., Normand et al., Buckley et al., Mao et al.*

Substitute Material for Pia Mater		
	Young Modulus (kPa)	**Poisson Ratio**
Agarose 10-15%	000 - 3700	0.5
PDMS 10:1	1400	0.45 - 0.5

Table 4.6: Young modulus and Poisson ratio of possible materials as substitute of pia mater: 10-15% agarose and PDMS 10:1. *From Liu et al., Johnston, Normand et al.*

Different phantoms in agarose or PDMS were fabricated using several techniques to understand which guarantees a mechanical trend similar to the optic nerve one during insertion and extraction tests. The strategies that have been tested consist of:

1. **Technique 1** Cylinder/parallelepiped of 1.5% agarose wrapped from 50 μm of 10:1 PDMS. Regarding the production of 1.5% agarose, 1.5 g of agarose was mixed in a beaker with 100 ml of TBE buffer, then placed in the microwave at 100 °C and mixed until a clear solution was obtained. After that, the mixture was poured into suitable containers and allowed to cool to room temperature. Thus, the material obtained was kept in the fridge at 4 °C and cut into parallelepipeds or in cylinders with appropriate pipettes when it had to be used. As regards the fabrication of 50 μm of PDMS, PSS was first coated at 2000 rpm on a Si wafer and cured at 145 °C for 10 min. After that, the PDMS base and the curing agent were mixed in a mixer for 3 min and spin-coated on the wafer at 1500 rpm. Subsequently, the wafer was cured in the oven for 2 hours at 80 °C. The release was carried out with DI. Then, the layer obtained was treated with the oxygen plasma for surface activation to improve adhesion with the agarose. Just before the mechanical tests, the phantom was made by rolling the layer around the 1.5% agarose cylinder.

2. **Technique 2** PDMS layer over which 1.5% agarose was cured. The realisation of the PDMS layer is similar to that described in technique 1. The main difference consists in pouring the 1.5% agarose solution, properly mixed and heated, in a 55 mm diameter petri dish, whose walls were covered with the PDMS layer previously treated with oxygen plasma. Then, it was left to cool to room temperature.

3. **Technique 3** PDMS cylinder. The main interest in mechanical tests is to analyse the forces peaks that develop when OpticSELINE crosses the membrane, the pia mater. Therefore, phantoms were made only in PDMS. The uncured PDMS was poured into a glass petri dish, baked at 80 °C for 2 hours and then cut into a cylinder.

4. **Technique 4** 10%-15% Agarose cylinder, fabricated for the same reason of technique 3. The fabrication process is similar to that described in technique 1, changing only the ratio between base and buffer (10 or 15 g of agarose mixed with 100 ml of TBE buffer).

5. **Technique 5** Thin layer of 50 μm thick PDMS. The layer, manufactured as described in technique 1, was mechanically tested to evaluate the insertion force peaks.

Mechanical insertion tests were performed with samples in PI, OSTE+ CC and three layers, both in ex-vivo nerve and in nerve phantom, to assess which is more mechanically similar to the rabbit optic nerve. Extraction tests were also carried out for PI samples with memorized wings. The samples, free of traces and electrodes to characterise only the substrate, were fabricated in accord with the process flow described in Section 4.3. Mechanical tests were conducted as reported in Section 4.8. The trends and peaks obtained with nerve phantom were then compared with those of ex-vivo optic nerve.

5 Results and Discussion

5.1 Mechanical properties of OSTE+

The goal of tensile tests is to characterise the thin layers of OSTE+ Flex and OSTE+ CC. For this purpose, the mechanical tests were carried out by varying some microfabrication parameters to standardise the fabrication process of OSTE+ samples, taking into account the mechanical properties reported in datasheets.
Regarding OSTE+ Flex samples results, no significant difference has been noted in different fabrication conditions. The OSTE+ Flex is subjected to elastic deformation, with a Young's modulus of about 13 -15 MPa, a maximum stress of 12-15 MPa and a maximum elongation of about 70%. The results' homogeneity among samples of different batch shows that the microfabrication parameters don't influence the performance of polymerization and, so, the prepolymer is completely polymerized. Moreover, the mechanical properties (Table 5.1) are also comparable to those reported on the datasheet (E = 28 MPa).

Different values were found, instead, for OSTE+ CC. These results have led us to standardise the baking process: 14 h at 100 °C plus cooling down to room temperature to reduce the residual stresses, instead of 100 °C overnight. In the absence of the cooling step, a different trend of the stress-strain curve was noticed, probably due to incomplete polymerization and a missed relaxation between polymer chains (Figure 5.2). The first part of the curve, related to the elastic deformation, is similar among all the analysed samples with and without cooling step. About the second region of the curve, it is characterised by a more pronounced plastic deformation with high elongation if samples weren't cooled down to room temperature, characteristics absent in the case of new standardise baking. The high elongation is a behaviour attributable to OSTE+ Flex. Moreover, the parameters calculated in both two situations are comparable except for the maximum elongation, as it is shown in Table 5.2. The baking standardisation not only guarantees the mechanical properties comparable to that reported in the datasheet (E = 1 GPa and ε_{max} = 2%), but also limits the residual stresses, avoiding problems with metal deposition. If OSTE+ is not completely polymerized, the metal usually doesn't remain above the OSTE+ surface but it "sinks" inside the polymer, after its deposition.
According also to the parameters reported in the datasheet, we can conclude that OSTE+ CC has a Young modulus of about 1.5 GPa with a maximum strain of 3 - 5% and a maximum stress of about 20 - 25 MPa.

As for three layers specimens, i.e. two layers of OSTE+ Flex (5 μm thick each) and a sandwiched non-patterned layer of OSTE+ CC (5 μm thick), the trend of the stress-strain curve is uniform among all samples and it is characterised by a first elastic deformation plus a plastic behaviour due to the presence of different material stiffness. The Young modu-

lus (1.3 GPa) and maximum stress (27 MPa) are similar to OSTE+ CC, while the maximum strain (40%) is comparable to OSTE+ Flex.

	Wafer1	Wafer2	Wafer3	Wafer4
E (MPa)	13.62 ± 0.94	15.38 ± 0.54	17.05 ± 3.01	13.25 ± 0.43
σ_{max} (MPa)	12.79 ± 1.93	15.83 ± 3.24	14.23 ± 0.85	13.07 ± 4.01
ε_{max} (%)	68.30 ± 5.85	71.05 ± 7.86	65.41 ± 13.58	73.15 ± 14.01
# specimen	12	12	2	5

Table 5.1: Mechanical properties of OSTE+ Flex specimens for different conditions presented in Section 4.1. Mean values and standard deviation of Young modulus, maximum stress and maximum strain are reported.

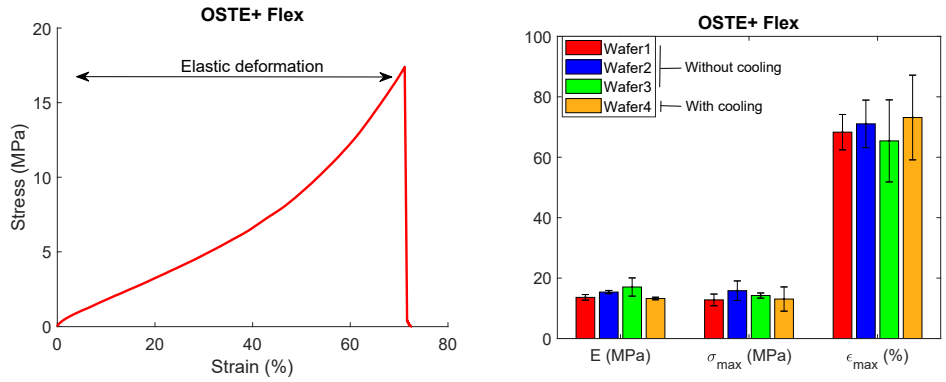

Figure 5.1: (*left*) Stress-strain curve from a sample of OSTE+ Flex. (*right*) Bar diagram of Young Modulus, maximum stress and maximum strain of different fabrication processes.

	Wafer1	Wafer2	Wafer3	Wafer4	Wafer5	Wafer6	Wafer7
E (GPa)	1.38 ± 0.09	1.50 ± 0.05	1.55 ± 0.13	1.37 ± 0.13	1.47 ± 0.11	1.58 ± 0.13	1.54 ± 0.14
σ_{max} (MPa)	22.54 ± 3.47	25.57 ± 4.11	25.98 ± 2.24	24.69 ± 1.35	21.36 ± 5.18	27.18 ± 7.37	21.42 ± 7.42
ε_{max} (%)	49.24 ± 5.96	36.12 ± 10.15	41.36 ± 14.89	48.01 ± 9.76	5.01 ± 3.05	3.06 ± 0.68	3.11 ± 1.68
# specimen	11	12	12	3	11	10	11

Table 5.2: Mechanical properties of OSTE+ CC specimens for different conditions presented in Section 4.1. Mean values and standard deviation of Young modulus, maximum stress and maximum strain are reported.

5.2 Optimisation of OpticSELINE design

Two designs were proposed: Design 1 with an active area of 1.1 times larger than the current version of Gaillet et al., and Design 2 with 1.86 times greater active area. Design 2 was implemented to realise bigger wings and, therefore, to increase the number of electrodes for better stimulation. Tests were carried out on ex-vivo rabbit nerve to evaluate the new active area dimensions. Their results have shown that the width of 0.8 mm allows the implant to enter completely, remaining flat at the level of the active area, as it is represented

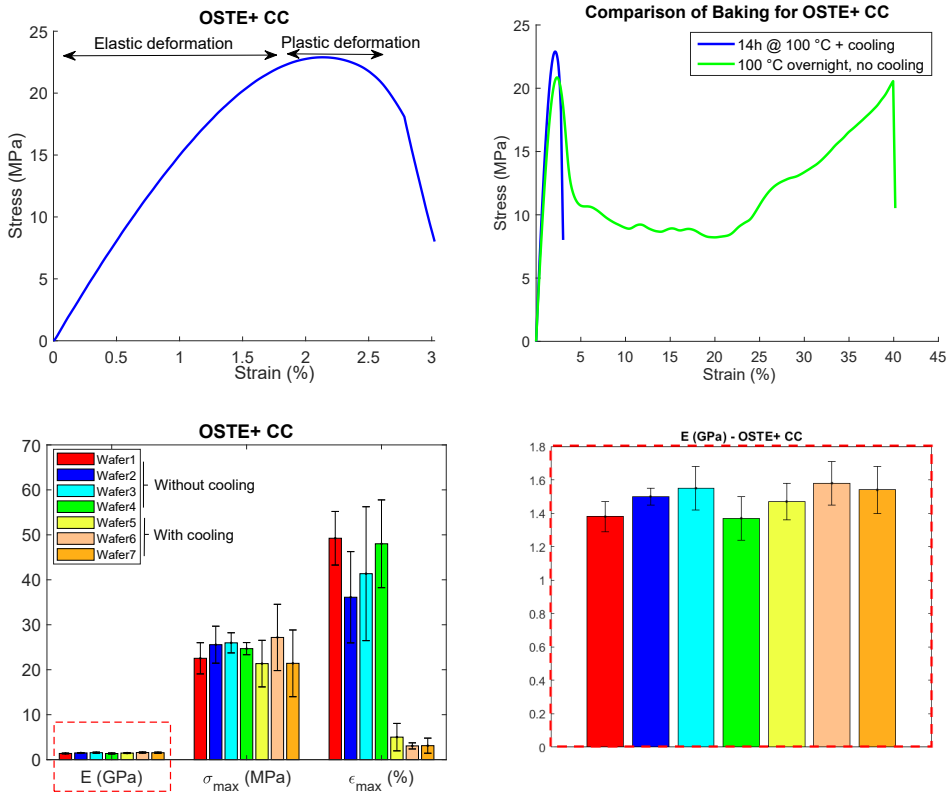

Figure 5.2: (*top*) Stress-strain curve from a sample of OSTE+ CC and comparison of stress-strain curves between the standardised baking (14h at 100 °C and cooling down to room temperature) and the baking at 100 °C overnight. (*bottom*) Bar diagram of Young Modulus, maximum stress and maximum strain and magnification of Young Modulus bar diagram of different fabrication processes.

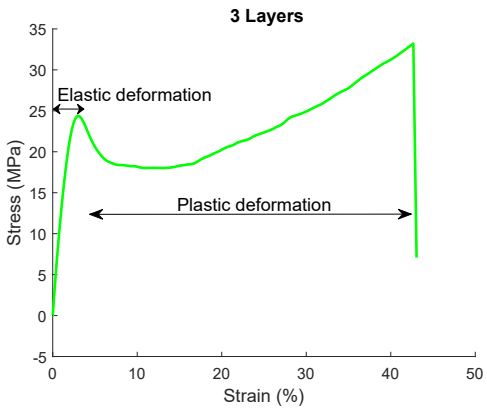

	3 Layers
E (GPa)	1.32 ± 0.07
σ_{max} (MPa)	27.25 ± 6.63
ϵ_{max} (%)	42.25 ± 7.48
# specimen	7

Figure 5.3: Stress-strain curve from single sample and Young modulus, maximum stress and maximum strain in terms of mean and standard deviation of three layers specimens (two OSTE+ Flex layers and a sandwiched non-patterned OSTE+ CC layer, each 5 μm thick).

in Figure 5.4.
To realise a more compliant OpticSELINE with neural tissue, PI has been replaced by

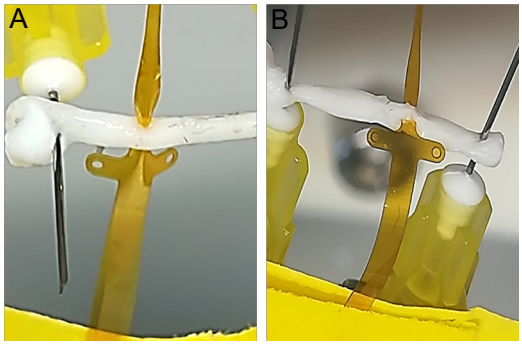

Figure 5.4: PI substrate characterised by 1.075 mm wide active area (*A*) and 0.8 mm wide active area (*B*) after insertion. Device with a larger active area (1.075 mm) bends after insertion.

OSTE+. Thanks to its tunable mechanical properties, a softer interface with a Young's modulus comparable to the tissue one can be fabricated by adjusting the stoichiometry of its monomers. The purpose is, in fact, the reduction of the foreign body reaction around the implant to improve its biointegration. Besides, OSTE+ have several advantages as:

- Photopatternable. It acts as a negative resist that is cross-linked with UV exposition. For this reason, during the microfabrication processes, it is easier to pattern it than PDMS, which requires more complicated techniques for the encapsulation of the electrodes. The SU8 is also a photostructurable polymer, but it is necessary to fabricate a thin film to make it flexible [43, 44].

- Tunable mechanical properties. A variation of stoichiometry (the ratio of the monomers functional groups) induces a Tg and Young's modulus (E) change [43, 44].

- Low sensibility to moisture absorption. OSTE+ is hydrophobic and not very sensitive to oxygen unlike PI [43, 62].

- Adhesion with metals. The surface can well adhere with metal, without the need for additional bonding techniques, thanks to the presence of the epoxy groups [63, 43].

Of course, the realisation of the device in OSTE+ requires some structural changes as the introduction of the metal reinforcement to avoid tip breakage during insertion. The maximum stress to which an OSTE+ Flex substrate can be subjected is equal to about 15 MPa, unlike PI substrate characterised by limit stress of 350 MPa. For this reason, the definitive OSTE+ designs include metallized tip and transversal bars in platinum (100 nm thick) added along the insertion zone. The thickness of 100 nm has been chosen because it was observed that high thicknesses of metal, sputtered on the device's tip, broke it when the device is closed in a loop configuration. The FE simulations results of the original design compared with the two versions (Design 1 and Design 2) in OSTE+, with and without metallization, are reported in order to understand the choice of the metal support configuration.
In Figure 5.5, one can notice that the original design in OSTE+ is subjected to a maximum stress of about 76 MPa, which is far greater than the OSTE+ Flex limit stress and, therefore, the device certainly breaks. Stresses are localised in the tip, that is the point of the concentrated force's application, while they are reduced in the active area because of the enlargement of the cross-section area. To overcome this drawback the design has been modified. The reduction of tip dimensions from 0.29 mm to 0.14 mm and the gradual expansion from the tip to the active area are proposed for both versions to ease the insertion. Moreover, they reduce the maximum stress of a little more than 10 MPa in the

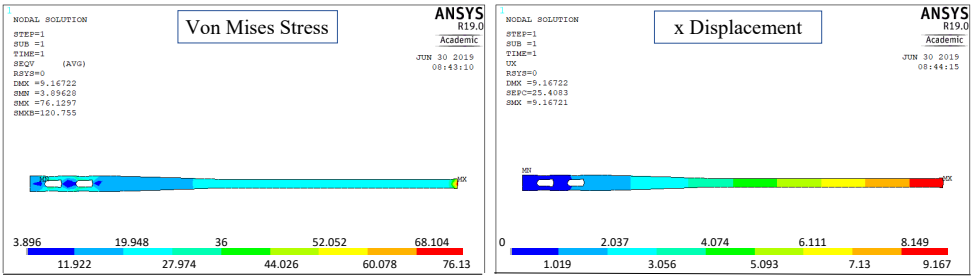

Figure 5.5: FE simulation during insertion of original design in OSTE+, 30 μm thick. Von Mises stresses and x-displacement are represented when F=400 mN is applied. The maximum stress, located on device tip, is 76 MPa, greater than OSTE+ Flex limit stress (15 MPa).

case of Design 1. However, these two changes are not enough to reach our goal. Therefore, the deposition of platinum has been introduced as support during insertion because it can better withstand traction, limiting the probability of breakage. Among the support's configurations, the central holes surrounded by metal don't allow a good performance because the maximum stress exceeds the metal breaking modulus (205 MPa). Instead, as for other two configurations (metallized tip with and without the addition of platinum transversal bars), the maximum stresses, placed in the regions where platinum has been deposited, are lower than its breaking point. There are no differences between these two types of metallic supports. Furthermore, taking into account the displacement along the x-axis that is the direction of the insertion, the oblique deformation of the tip can be observed for the central holes based support. This bending was also highlighted during the mechanical tests. The presence of these central holes, in fact, hinders the insertion since the device tries to enter laterally. The x-axis displacement is reduced switching from the configuration without any metallic support to one with the metallized tip and transversal bars. The Von Mises stresses distribution and x-displacement for Design 1 with tip and transversal bars in metal are reported in Figure 5.6. The stress distribution and x-displacement for the other reinforcement configurations are reported in Appendices.
A similar trend has been also observed for Design 2 (Figure 5.6). In this case, the maximum stress (about 144 MPa) is about twice than that obtained in Design 1 due to the greater enlargement of the active area: it augments from 0.49 mm to 0.80 mm in width. Likewise, the need for the metal reinforcement to better withstand traction during insertion is highlighted for Design 2. Furthermore, it is shown that the presence of central holes surrounded by metal is a poor choice both for the deformation of the device and for the high stresses located at the tip. The above-mentioned results are referred to 30 μm thick device in OSTE+ Flex with an insertion force equal to 400 mN, the maximum force evaluated by Cutrone et al. for SELINE in PI [31].
Besides, a further assessment of the applicable maximum force has been analysed for both designs with a thickness of 15 μm. For Design 2, the maximum insertion force applied with metallized tip is equal to 180 mN. While, in the case of absence of reinforcement it is reduced to 20 mN, double than usual insertion forces (10 mN Cutrone et al.). As for Design 1, it is 50 mN in the absence of a metal support and goes up to 200 mN with metallized tip. From this first analysis about maximum applicable force, it would seem possible to reduce the design thickness from 30 μm to 15 μm to increase OpticSELINE biocompatibility. However, to tests it, experimental implants are needed, also to understand possible microfabrication problems. FE simulations for 12 μm thick PI model have shown that the maximum applicable force is 380 mN for Design 2 and 850 mN for Design 1. These values are greater than OSTE+ substrate's ones due to higher limit stress of PI.
Finally, the FE model's limits must be taken into account: a static analysis has been per-

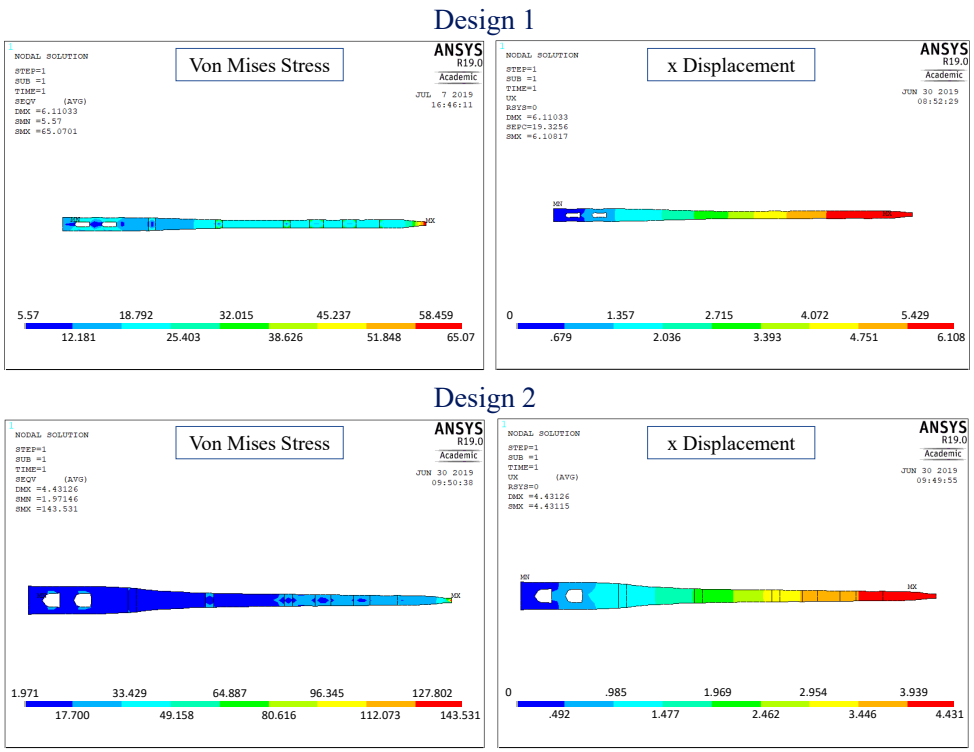

Figure 5.6: Von Mises stresses distribution and x-displacement of Design 1 and Design 2 in OSTE+ Flex with tip and transversal bars metallized in platinum. Insertion force is 400 mN.

formed ignoring the inertial forces. These effects are negligible due to the low insertion speeds. However, a more precise model can be developed to take into consideration the dynamic aspect in case of greater speed and the presence of traces and electrodes, that could affect the stress distributions.

5.3 Fabrication

The fabrication of OpticSELINE, characterised by three layers substrate, faced two major difficulties: the sputtering of platinum and the release of the device.
As for the first problem, it has been observed that platinum, once it was deposited on the last layer of OSTE+ Flex, didn't remain above the substrate but it "sank" into the polymer. This complication didn't occur with OSTE+ CC based substrate if it fully polymerized. Pt profile was measured in correspondence with the traces by mechanical profilometer and a "sinking" effect of few microns was estimated only for three layers substrate (Figure 5.7). Moreover, platinum layer contained some ripples more evident in extensive areas and on OSTE+ Flex. This surface roughness could improve platinum electrochemical properties, thanks to the increment of the effective surface area and, therefore, of the active site capacitance [64]. Comparing the two opposite results and their respective mechanical characteristics, a presumable explanation of this effect could be due to different density and stiffness of the two materials contrasted with platinum properties. Even if the curing and baking time have been varied for a probable incomplete polymerization of OSTE+ Flex, the final effect didn't change. Thus, the problem is not caused by incomplete polymerization.
Regarding the release of three-layer based OpticSELINE, the main difficulty is to remove it

(a) Three layers substrate **(b)** OSTE+ CC substrate

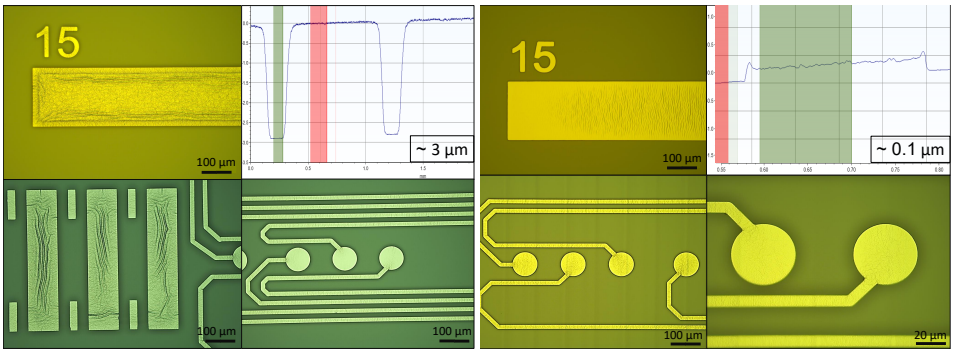

Figure 5.7: Profilometer and optical images of sputtered platinum for three layers substrate (*a*) and OSTE+ CC substrate (*b*).

from the wafer, avoiding that the lateral stoppers bend and stick each other. The sample was placed between the two tissues with a weight above to dry it flat, even if this bending sometimes occurred as soon as the tissue was removed. The above-mentioned negative aspect influences the subsequent memorization of the wings because, if the lateral stoppers fold and the device is not flat, it complicates the device positioning in the metallic mould. Therefore, the result of the thermal treatment could be not positive and, the reproducibility of OpticSELINE is compromised. We tried, also, to modify the sacrificial layer, replacing PSS with silanization in order to not use DI for release. Two types of silane were tested Trichloro(1H,1H,2H,2H-perfluorooctyl)silane and Chlorotrimethylsilane, without solving the drawback. In particular, the former didn't allow OSTE+ Flex to be well spin-coated. The latter, instead, made the release impossible. However, we noted that thin layers of OSTE+ Flex without sputtered platinum remained flat after release. Therefore, the main problem could be found in the platinum, which hinders the pattern of the electrodes and the release of the device. Moreover, its stiffness (50-500 GPa modulus) increases the electro-tissue mismatch deteriorating electrical performance, even if this material is widely used in biomedical application. To overcome this issue, the gold-coated titanium dioxide nanowires, a stretchable material suitable for substrates such as OSTE+ Flex, could be integrated into OpticSELINE.

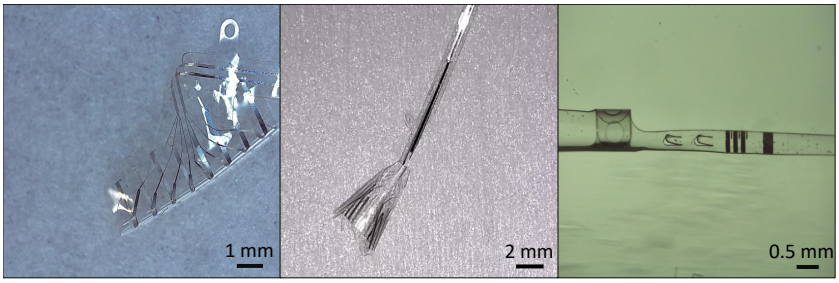

Figure 5.8: Optical images of some issues occurred after release of OpticSELINE characterised by three layers substrate. The bending of lateral stoppers hinders the wings memorization.

As far as wings memorization is concerned, the parameters used for the PI-based substrate have been varied compared with those of Gaillet et al. (1h at 200 °C). The temperature has been reduced to 160 °C and the treatment time doubled to 2 hours since the mould withstands up to 175 °C. However, this change did not affect the results of the PI treatment. The wings were open at an angle of about 30°- 35° both for PI and OSTE+ CC substrate.

For the wings memorization of the three layers substrate, the final angle was reduced to about 20°- 25°. Moreover, for this latter substrate, it would be better to leave the device in the mould for a few days to make it flat as much as possible.
Finally, after memorization, some wrinkles were presented in the traces without, however, breaking them.

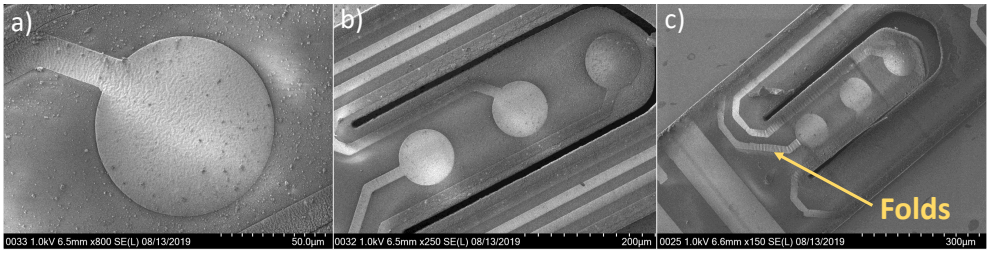

Figure 5.9: SEM images of OSTE+ CC based OpticSELINE. (*a*) Magnification of electrodes with some ripples. (*b-c*) Image of wings before memorization (*b*) and after memorization (*c*). After memorization, some folds are presented on traces at the level of wings bending.

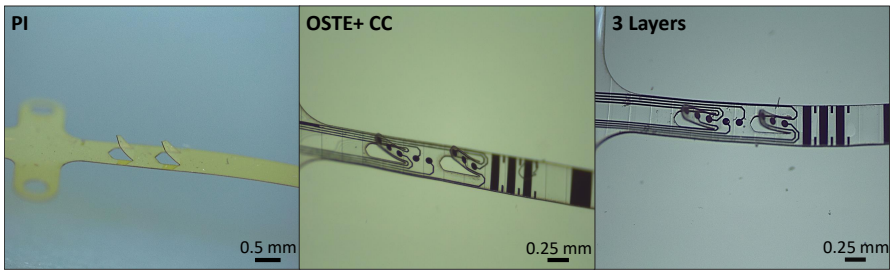

Figure 5.10: Wings memorization of PI, OSTE+ CC and three layers substrate. The effective opening angle is about 20°-25° for three layer substrate and 30°-35° for PI and OSTE+ CC substrate.

5.4 Optimization of photolithography parameters

The viscosity of uncured OSTE+ CC needs a technique able to pattern it with MJB4, obtaining a flat profile and avoiding that it adheres to photomask during polymerization. Moreover, it is not convenient to use the direct writing lithography due to OSTE+ CC high exposure dose required.

The first group of tests evaluates the presence of a PET film placed on the OSTE+ CC layer before exposure and its removal before or during development. This film, mainly used for preventing the wafer from sticking to the chrome mask during photolithography, allows to obtain a profile of the wings flatter than a soft contact exposure in the absence of this layer. However, the problems encountered with this technique concern the presence of small bubbles observed under the microscope, due to air trapped between OSTE+ CC and PET and light diffraction. The used PET film would seem to be not completely transparent but has an internal pattern which is transferred to the OSTE+ CC during photolithography. Moreover, if the film is removed before development, some features move due to the high adherence of the OSTE+ CC to the PET film damaging, thus, the wings' profile. Finally, the contours are not well defined, probably due to the increased gap with the addition of PET film.

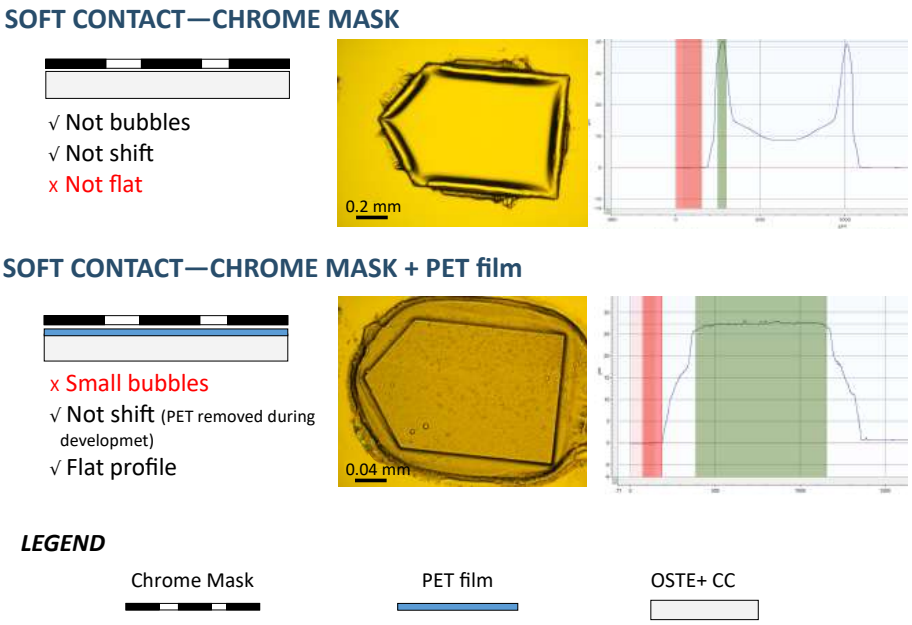

Figure 5.11: Results of first group of tests: soft contact exposure with or without PET film onto uncured OSTE+ CC layer. The pro and cons of tests with images under the microscope and the mechanical profilometer are reported. The OSTE+ CC thickness is 30 μm.

To improve the wings profile with well-defined contours, we tested two different types of masks as substitutes for the chrome one, since we observed as PET film can be a possible solution to guarantee a flat patterned layer. The idea is to create flexible masks, which can be removed during development to prevent small features, such as wings, from being shifted or removed. Additionally, the mask is put in direct contact with the layer to be exposed and, therefore, the resolution could improve. These techniques have been tested both on 30 μm thick single layer of OSTE+ CC (second tests group) and on 5 μm thick layer of OSTE+ CC coated onto OSTE+ Flex (third tests group). The total exposure time is reduced from 6 min for thickness of 30 μm to 2 min for 5 μm of OSTE+ CC. The two types of masks, described in Section 4.4, consist in open PET film with UV opaque material (Technique 1), and PET whole film with UV opaque pattern material (Technique 2). In the case of 30 μm thick layers, both techniques have qualitatively produced the same result, i.e. the profile continues to be approximately flat with undefined shapes. The unique difference is the absence of small bubbles through Technique 1 because the light passes through the openings of the mask, and not through the PET, as mentioned above. Nevertheless, the discrepancies between the two techniques are more marked in case of the 5 μm layer (third group of tests). As for Technique 1, the wings are shifted/removed due to the attraction forces between OSTE+ CC and metal used for making the PET film non-transparent to UV light. To solve this difficulty, a mask made of PET plus black PDMS instead of metal was produced. However, the effect is the same: the OSTE+ CC adheres to the walls of the mask's openings, causing the wings movement. It appears as thick black contours around the wings, evident under the microscope, since the OSTE+ CC detaches from the wafer and adheres to the mask; this is more or less noticeable depending on the interaction forces between OSTE+ and mask. As for the mask characterised by full PET/b-PDMS/open PET (Technique 2), it ensures a flat profile, without any movement of wings,

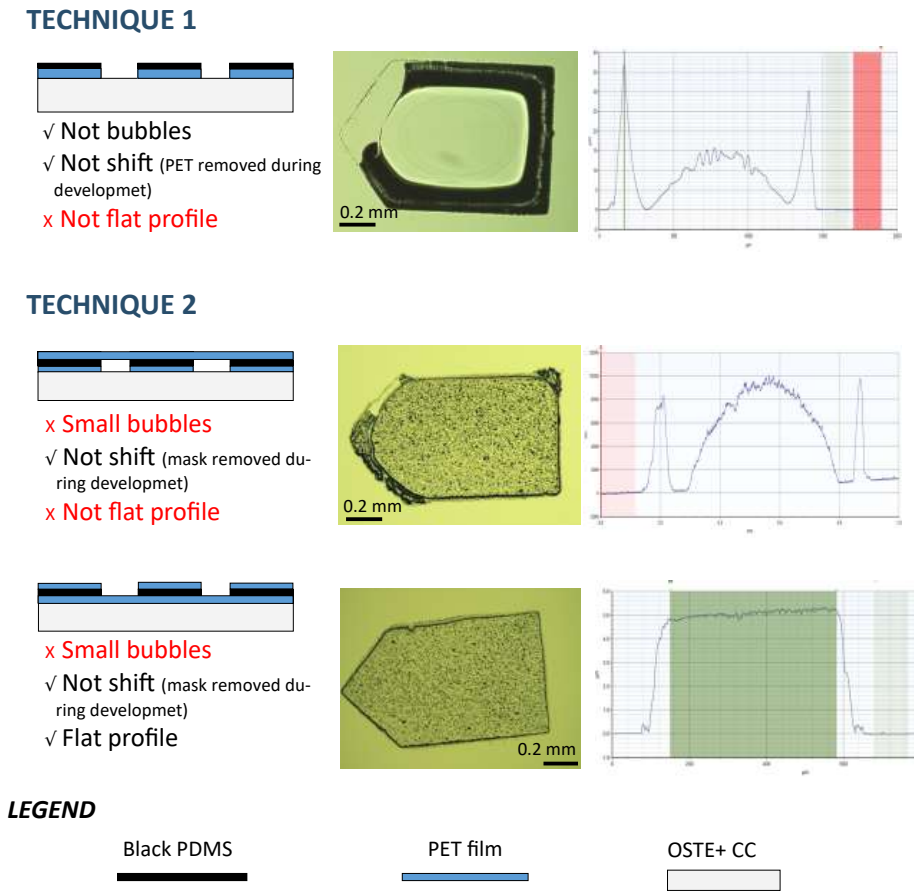

Figure 5.12: Results of third group of tests: the technique 1 and the technique 2 results are reported, with the respective pro and cons and with images under the microscope and the mechanical profilometer. The OSTE+ CC layer is 5 μm thick.

only if the entire film of PET is in direct contact with the OSTE+ CC. The same mask has been tested in two directions, full and open PET in contact with the layer to be patterned, maintaining the same exposure parameters of 60 s x 2 cycles. The reason why we want to put the open PET in contact is to create a small gap to try to overcome the problem of bubbles formation and jagged profile, but it doesn't work. Thus, we established that the whole PET must be in contact with the OSTE+ CC. The drawback of this type of mask is that it can only be used one time. In fact, after having exposed it in Ethyl-l-lactate, the contours of the b-PDMS features are damaged and automatically deform the shapes of the wings in the following processes. Moreover, since it is characterised by three layers and, so, it isn't very flexible, it is difficult to remove it during development due to the adhesion of PET with OSTE+.

The last group of tests consists of hard contact exposure with a chrome mask. The use of a layer, placed on the uncured OSTE+ CC, is inevitable to obtain a flat profile. Besides, the use of a rigid mask prevents the deformation of features. This technique guarantees a flat profile, well-defined contours, no shifting or removal of wings. The presence of bubbles was also solved by replacing 23 μm PET with 250 μm PDMS. The reason why a thicker layer of 10:1 PDMS was manufactured is to be easily handled. Finally, regarding PDMS

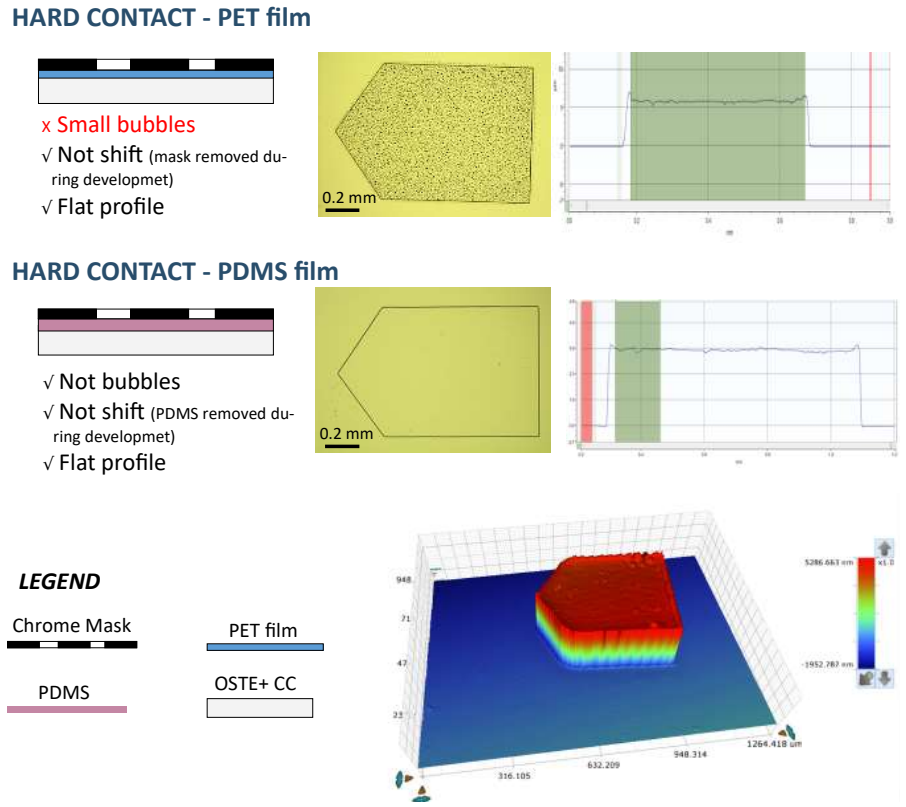

Figure 5.13: Results of fourth group of tests: hard contact exposure with PET or PDMS layer onto uncured OSTE+ CC layer, 5 μm thick. Images under the microscope and the mechanical profilometer are reported for both films with respective pro and cons. Optical profilometer image is refer to the PDMS technique.

usage, the development time is reduced from 10 to 5 minutes and does not require the user's labour as in the case of PET. It detaches autonomously and, therefore, reduces the probability of damage to the features due to possible sudden movements of the operator. From the results obtained, the technique of the OSTE+ CC photolithography, able to create a flat patterned layer, is the last one that consists in the use of the PDMS layer between the uncured OSTE+ CC and chrome mask.

5.5 Analysis of three layers profile and thermal memorization performance

For the realisation of a three layers substrate, it is necessary to verify that the profile of the entire substrate is flat after the spin-coating of the last layer of OSTE+ Flex. It limits potential problems with the subsequent patterning of the electrodes. Different thicknesses were tested to understand the value of each layer necessary to satisfy our objective. Figure 5.14 reports the results measured with the profilometer.
Examined the results, no speed value used for spin coating the third layer of OSTE+ Flex would seem appropriate to ensure a flat substrate. Of course, if the thickness of the third layer decreases, the gap value in the wings area increases, as expected. This value is few hundred nanometres in case of 3 - 4 μm thick OSTE+ CC plus OSTE+ Flex spin-coated at

2000 rpm. This recipe has the step at 2000 rpm, which is longer than the standard recipe's one, without a peak at 3000 rpm used for removing the material accumulation at the edges of the wafer.

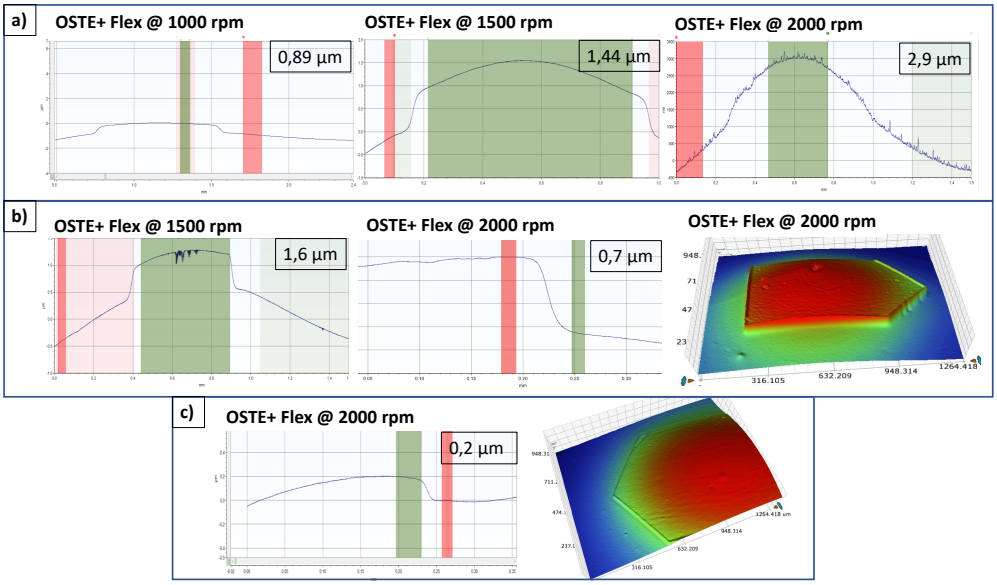

Figure 5.14: Analysis of three layers substrate profile with different OSTE+ Flex thickness spin coated on 5 μm (*a*), 4 μm (*b*) and 3 μm (*c*) of OSTE+ CC. The gap values, measured by mechanical and optical profilometer, are reported.

Besides, observing the profile with SEM, it can be seen that the gap would seem almost null or insignificant in case of 4 μm OSTE+ CC and 3 μm OSTE+ CC with OSTE+ Flex at 2000 rpm. Figure 5.15-a shows a substrate characterised by 4 μm OSTE+ CC plus OSTE+ Flex at 1500 rpm. In this case, the total substrate is not perfectly flat, but also the gap is not as accentuated as measured with a profilometer. By contrast, the gap of the substrate composed of 3 μm OSTE+ CC plus OSTE+ Flex at 2000 rpm seems to be absent (Figure 5.15-b), inasmuch only two "shadows" in correspondence with wings are shown, as a demonstration of substrate flatness.

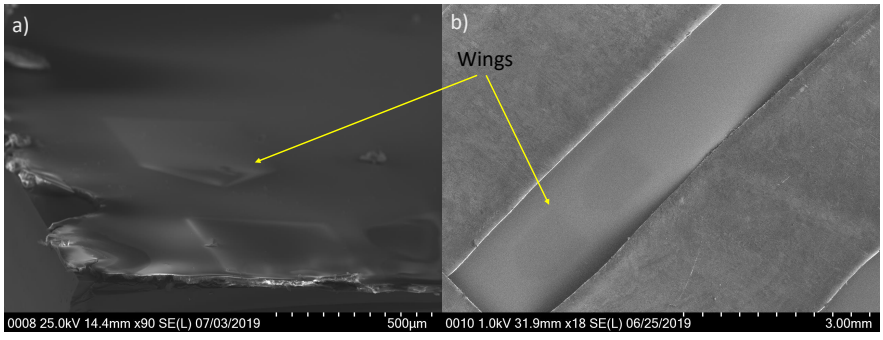

Figure 5.15: SEM images of three layers substrate at wings area. *(a)* The sample is characterised by OSTE+ CC spin-coated at 3500 rpm and covered with OSTE+ Flex at 1500 rpm. The profile in not perfectly flat. *(b)* The sample is characterised by OSTE+ CC coated at 4000 rpm and covered with OSTE+ Flex at 2000 rpm. The wings appear as "shadows".

The difference in results between profilometer and SEM could be due to their respective

measurement modes. The profilometer is more sensitive to the difference in density and stiffness of the material and, therefore, this could affect the measurements. Moreover, observing the subsequent patterning of the electrodes, there is no deformation on the Pt layer at the wings edges.

The following evaluation is whether the OSTE+ CC thickness is sufficient to memorize the 3D configuration of the wings. Figure 5.16 reports the memorization of wings performed with different values of OSTE+ CC thickness.

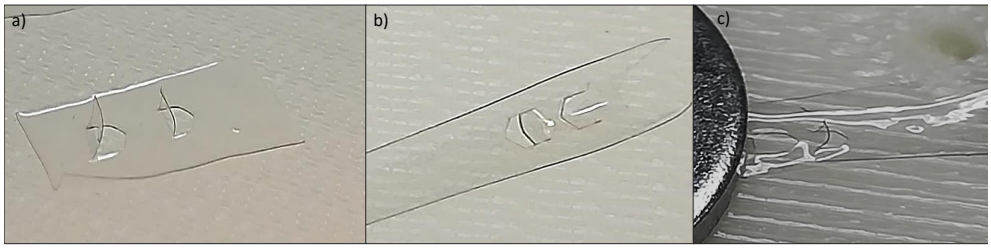

Figure 5.16: Thermal memorization of wings made in three patterned layers, with 5 μm thick *(a)*, 4 μm thick *(b)* and 3 μm thick *(c)* OSTE+ CC, respectively.

Each of these three situations allows the wings to remain in open configuration in the absence of Pt sputtered above.
In the light of the following results, it was decided to cover OSTE+ CC, spin-coated at 3500 rpm, with OSTE+ Flex at 2000 rpm. It is a trade-off between the ease of obtaining a flat sandwich, guaranteed by a thin middle layer, and the best performance of wings memorization, achieved with thick OSTE+ CC. Of course, the total thickness of the substrate must be limited to not augment the device invasiveness.

5.6 Mechanical characterisation of OpticSELINE

The purpose of the mechanical characterisation of OpticSELINE is to evaluate the insertion forces' compatibility with the device and the anchorage of the electrode, inserted into the nerve. To do so, insertion and extraction tests in the optic nerve of New Zealand white rabbits and tensile tests were performed.

Insertion Test

The insertion tests were conducted on samples characterised by only PI, OSTE+ CC and three layers substrate for both designs (Design 1 and Design 2), six specimens for each condition. Analysing the results obtained, we can see the presence of two peaks of force that develop when the electrode tip enters the nerve (Peak 1), and when it reaches the active area corresponding to the device enlargement (Peak 2). As for the Peak 1 values, there are no significant differences between the three different substrates (about 10 - 20 mN, $p > 0.05$). Moreover, they are similar to those obtained by Gaillet et al. (32.5 ± 22.7 mN). As for Peak 2, instead, the values obtained for PI and OSTE+ CC substrates are reduced to 40 - 60 mN ($p > 0.05$), unlike those reported by the current device in PI (223.4 ± 92.2 mN). The reduction is due to the gradual enlargement of the device between the tip and the active area. It allows, in fact, a gradual increase of the hole diameter of the nerve, made previously by suture needle, and therefore a reduction of the maximum insertion force. However, for the three-layer substrate, insertion was not completed due to tip breakage that took place in all tested samples. This rupture happens once the tip has come out from nerve just before reaching the active area. The problem, occurred for both designs,

is due to the reduced stiffness of the substrate material. Nevertheless, the insertion of the three-layers device can be completed if it is made by hand. In this case, once the device tip comes out from the nerve, it is possible to continue the insertion by pulling it from the tip with the use of tweezers. Thus, the force applied is distributed on the device loop, allowing the insertion of the active area, the region of our interest.

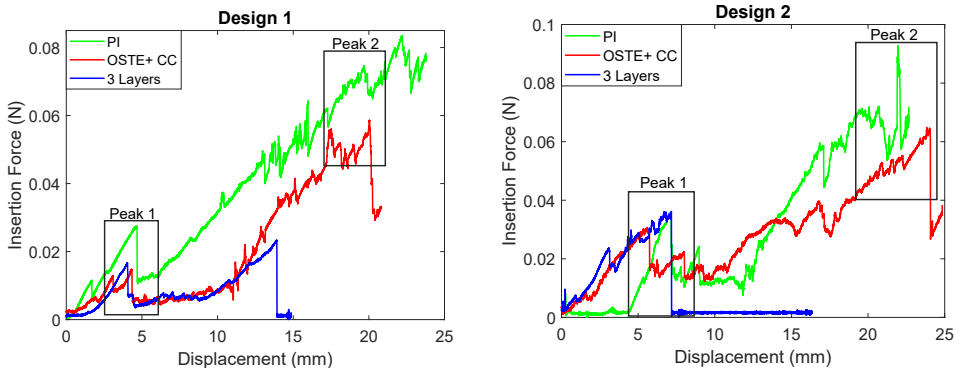

Figure 5.17: Forces developed during insertion of OpticSELINE. The trends of Design 1 and Design 2 in three different substrates (PI, OSTE+ CC and three-layers) are reported for a single sample. Peak 1 is related to tip insertion, while Peak 2 corresponds to the active area insertion.

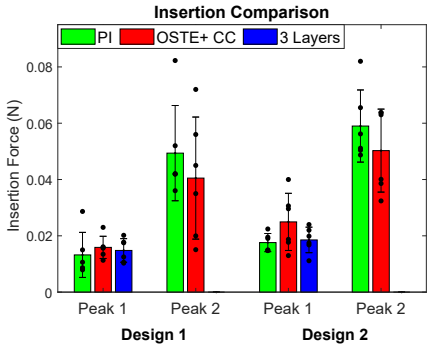

Substrate	Design 1		Design 2	
	Peak 1 (mN)	Peak 2 (mN)	Peak 1 (mN)	Peak 2 (mN)
PI	13.2 ± 8.0	49.4 ± 16.9	17.6 ± 3.2	59.0 ± 12.8
OSTE+ CC	15.9 ± 3.9	40.5 ± 21.7	24.9 ± 10.1	50.3 ± 14.7
3 Layers	14.8 ± 4.2	/	18.5 ± 4.5	/

Figure 5.18: Bar diagram and respective peaks values (mean ± s.d) obtained during insertion test are reported for both designs and three types of substrates (PI, OSTE+ CC and three-layers). Measurements are not statistical different ($p > 0.05$, $n = 6$). For three-layers substrates, the absence of peak 2 is due to the tip breakage after insertion.

Extraction Test

The extraction tests were carried out on the three substrates (PI, OSTE+ CC and three layers), both for Design 1 and Design 2, to assess the efficacy of the anchoring system thanks to the presence of memorized wings. For this purpose, the performance of the device with open wings (active configuration) was compared with those obtained with non-memorized wings (passive configuration) and without wings (TIME configuration). Five samples for each condition were analysed.

If the device is well anchored inside the nerve, the extraction curve has two peaks corresponding to the extraction of the two wings, as demonstrated by Gaillet et al. and Cutrone et al. The higher the value of the maximum extraction force, the better the stability of the device in the nerve. The extraction curves of the three substrate types for Design 1 and Design 2 are shown in Figure 5.19.

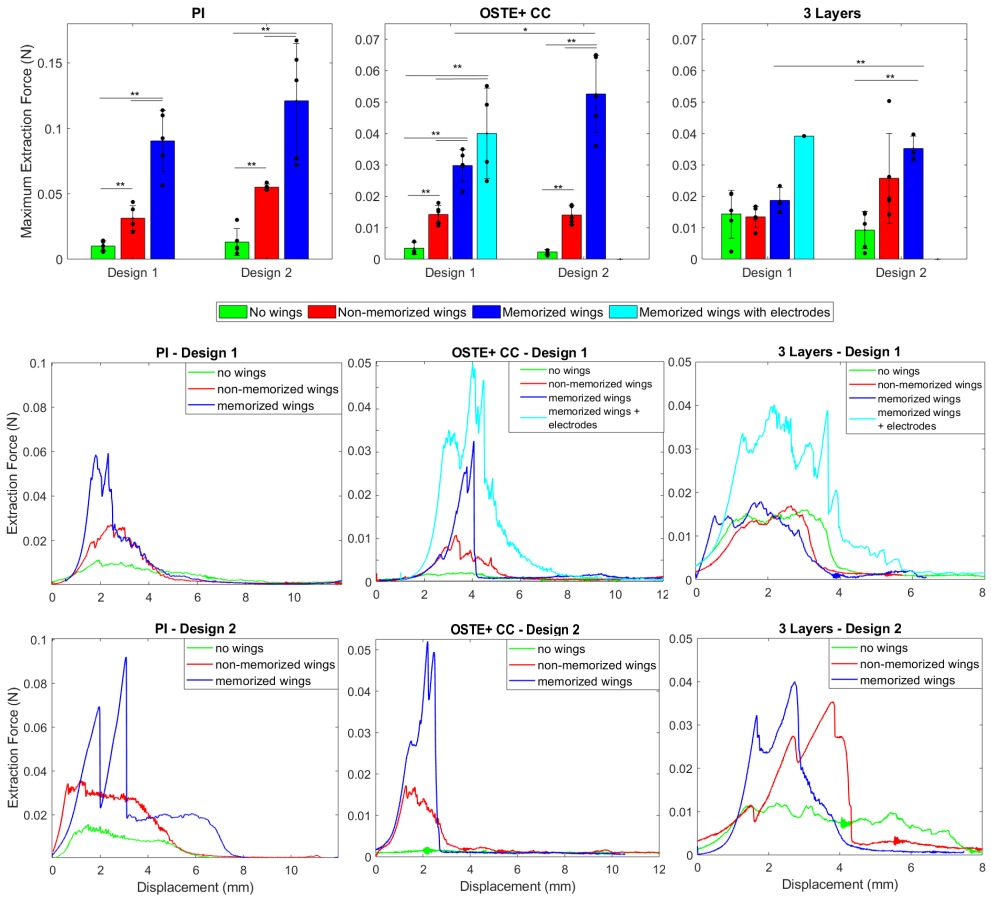

Figure 5.19: Bar diagram (mean ± s.d) of maximum extraction force and curve trend of a single OpticSELINE sample in different conditions. Comparisons between two designs (Design 1 and Design 2) in three different conditions (no wings, non-memorized wings and memorized wings) for the three substrates (PI, OSTE+ CC and three-layers) with and without electrodes are reported. Two peaks are related to the wings extraction (*$p < 0.05$, **$p < 0.01$; n = 5 for each condition, n = 3 for only three-layers memorized wings Design 1 - Design 2, n = 4 for only OSTE+ CC memorized wings with electrodes, n = 1 for only three-layers memorized wings with electrodes).

As for PI and OSTE+ CC substrates, the presence of wings in an open configuration ensures better anchorage than the device with non-memorized wings and in TIME configuration. In fact, for both of these two substrates, the peak values of the device in the active configuration are 2 - 3 times higher than non-memorized wings, and 8 - 9 times higher than those of device without wings. The results are statistically different between the three conditions (no wings, non-memorized wings and memorized wings; $p < 0.01$). Moreover, as for OSTE+ CC wings in the active configuration, a statistical difference is present between Design 1 and Design 2 ($p < 0.05$). It could mean an improvement in mechanical stability due to the increased size of the flaps. By contrast, this difference between Design 1 and Design 2 in the active configuration is not found in the case of PI substrates. Besides, analysing

the values of PI and OSTE+ CC substrates, it can be observed that the extraction forces of PI are 2 - 3 times higher than those of OSTE+ CC. It could be explained by the greater stiffness of PI which allows a better anchorage.
Regarding the three-layer substrate, the results are different from those of PI and OSTE+ CC interfaces. In particular, there is no statistical difference between the three conditions and no peaks are shown in the extraction curves of Design 1. As for Design 2, the only statistical difference is between memorized wings and devices without flaps. Only for Design 2 with memorized and non-memorized wings, the curve shows two peaks related to wings extraction. The maximum extraction force required in the active configuration is about 1.5 times smaller than that of OSTE+ CC substrate. These results could be explained by the substrate which is much softer than the other two and, therefore, it is not able to anchor well in the nerve as OSTE+ CC and PI substrate. Furthermore, the presence of peaks for only Design 2 could be justified by the larger size of the wings. Indeed, an improvement in electrode stability inside the nerve has also been evaluated for Design 2 in OSTE+ CC contrasted with Design 1. Moreover, comparing this extraction curve with those of the other two substrates, we can note that the distance between the two peaks is greater for three-layer substrate, as results of OSTE+ Flex elastic deformation contrasted to OSTE+ CC and PI plastic deformation. For three layers substrate with memorized wings (both designs), three specimens have been examined, instead of five, because of some problems occurred during fabrication/memorization of device.
Specimens in OSTE+ with flat electrodes and memorized wings (Design 1) were also tested to evaluate if there is some variation in the anchoring system. Figure 5.19 shows the results of these tests carried out on four samples in OSTE+ CC and one sample in three layers. It would seem that samples with patterned electrodes on wings are characterised by higher peaks values compared with the condition of the only substrate. This increment could be due to the increase in wings stiffness for the presence of sputtered platinum and, therefore, it could probably improve the device stability inside the nerve. Of course, to ensure such results, it would be advisable to carry out further extraction tests on samples with electrodes.

Substrate	**Typology**	**Maximum Force (mN)**		
		Only Substrate		*With Electrodes*
		Design 1	Design 2	Design 1
PI	*No wings*	9.9 ± 3.8	13.1 ± 10.1	/
	Non-memorized wings	31.3 ± 9.3	55.0 ± 22.2	/
	Memorized wings	90.4 ± 23.5	121.0 ± 43.9	/
OSTE+ CC	*No wings*	3.5 ± 1.9	2.3 ± 0.8	/
	Non-memorized wings	14.2 ± 3.0	14.0 ± 2.9	/
	Memorized wings	29.8 ± 5.2	52.6 ± 12.4	40.0 ± 12.5 (n = 4)
3 Layers	*No wings*	14.4 ± 7.6	9.2 ± 6.0	/
	Non-memorized wings	13.5 ± 3.4	25.8 ± 14.4	/
	Memorized wings	18.7 ± 4.2 (n = 3)	35.2 ± 4.0 (n = 3)	39.2 (n = 1)

Table 5.3: Values (mean ± s.d) of the maximum extraction forces for two designs (Design 1 and Design 2) in three different condition (no wings, non-memorized wings and memorized wings) for the three substrates (PI, OSTE+ CC and three-layers). n = 5 for each condition if not differently specified.

Figure 5.20 represents some specimens after extraction. In particular, the PI sample (Design 1) in passive configuration presents the opening of one of four wings occurred after extraction. It explains the results obtained (lower values in non-memorized wings than in the active configuration) and demonstrates the advantage of memorizing the wings to guarantee good stability in the nerve. The opening of the wings after insertion and the subsequent slight pullback is not ensured by a passive configuration and, therefore, the behaviour is almost comparable to that of TIME. The other two samples are in OSTE+ CC

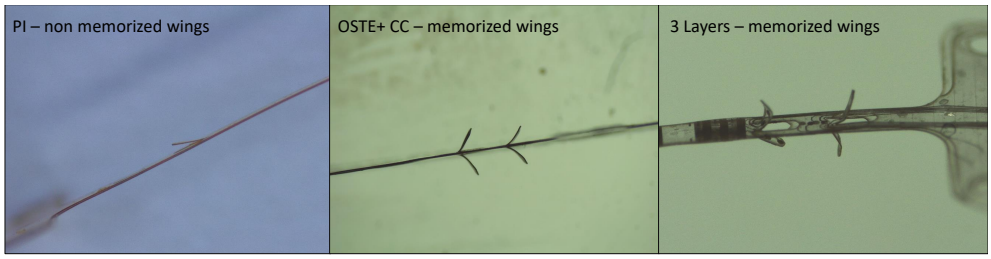

Figure 5.20: Images after extraction of PI sample with non-memorized wings and OSTE+ samples with memorized wings. After extraction the opening angle of wings increase if they anchor inside the nerve.

and three-layers substrate with patterned electrodes and with wings in the active configuration (Design1). In this case, we can note that the flaps opening angle is greater than the starting configuration, demonstrating the anchoring of the device. Furthermore, after extraction, the wings have no breakage or at most some fracture in correspondence with the region where the wings are attached to the main shaft.

To sum up, a better anchoring system is guaranteed by the PI substrate in the active configuration. However, it should be taken into account that, even if the anchorage could be improved with PI, its stiffness triggers the foreign body reaction followed by device deterioration. Thus, it is possible to affirm that a better compromise between mechanical stability and reduction of foreign body reaction can be obtained with OSTE+ CC substrate and with the three-layer substrate (Design 2 in the active configuration). The performance of three-layers substrate is slightly lower than that of OSTE+ CC. Nevertheless, it is important to note that this type of substrate is preferable to OSTE+ CC for the best biocompatibility with the tissue. A potential improvement in mechanical stability for the three-layers substrate could be achieved by increasing the thickness of the intermediate layer of OSTE+ CC. However, this modification could introduce possible difficulties in fabricating of final flat substrate and, therefore, problems with the subsequent manufacture of the electrodes. A thin layer of SU-8 could also be added to OSTE+ CC. SU-8 is a photopatternable and stiffer polymer than OSTE+ CC (2 - 3 GPa versus 1.5 GPa), but it is characterised by an elastic deformation and, so, it is not able alone to memorize wings [65]. For this reason, a combination of OSTE+ CC - SU-8 could be adopted to memorize wings thanks to OSTE+ CC and to improve anchoring system thanks to SU-8. Another possibility is to substitute OSTE+ CC with a photosensitive polyimide, that can be patterned directly by exposure to UV light, like OSTE+ CC, and can increase the stiffness of second layer [66]. Of course, these modifications require an analysis of the adhesion of these polymers with OSTE+.

Tensile Test

Tensile tests were performed on OpticSELINE fabricated in three different substrates (PI, OSTE+ CC, three-layer; Design 1) to evaluate the maximum force that causes the device's breakage and to compare it with the insertion force required during the mechanical tests. Analysing the curves and the maximum value obtained under the three substrates, it can be seen that the breaking force of OpticSELINE in PI (0.93 N) is about 10 times higher than those of the OSTE+ CC (0.11 N) and the three-layer substrate (0.089 N), as expected due to their respective maximum stresses (350 MPa for PI, 25 MPA for OSTE+ CC and 15 MPa for OSTE+ Flex). In particular, the value obtained for PI, similar to one evaluated in FE simulations for Design 1 (0.85 N), is about 18 times greater than its assessed insertion force (49.4 mN). Thus, PI device tolerates the insertion well, in fact, no problems were found during

the mechanical tests. As for OSTE+ CC, the breaking force is about 2 times higher than the maximum insertion force, which confirms that the device is still able to tolerate the insertion even if not as PI. Regarding the three-layer substrate, the maximum force evaluated is lower than the device in OSTE+ CC. However, a comparison with the maximum insertion force, required for such a substrate, cannot be made due to device breakage before reaching the active zone. The analysed results and the problems occurred during the insertion of this substrate indicate that the breaking force should be comparable to the insertion one. Finally, observing the two OSTE+ curves, we can see the higher deformation of the three layers substrate compared with OSTE+ CC, as expected because of their mechanical behaviours (elastic deformation for OSTE+ Flex contrasted with plastic deformation for OSTE+ CC).

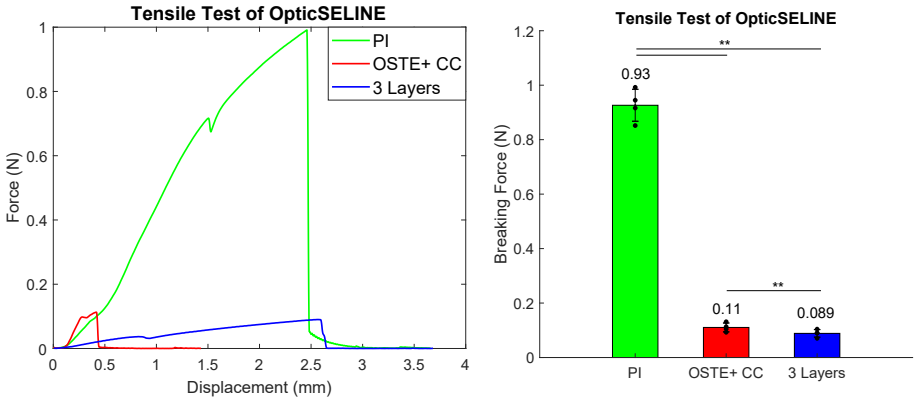

Figure 5.21: Tensile test curve of a single sample and bar diagram (mean ± s.d.) of maximum breaking force are reported for OpticSELINE in PI, OSTE+ CC and three layers substrate. Values are significant different (** $p < 0.01$, $n = 4$).

5.7 Optic nerve phantom

The role of optic nerve phantom is to substitute the explanted nerve to optimise the device and to evaluate the forces developed during the insertion and extraction tests. Mechanical tests were carried out to assess the similarity with the fresh nerve.
The phantom made of 1.5% agarose plus PDMS under technique 2 and the one characterised by a 10%-15% agarose cylinder (technique 4) were excluded from the mechanical tests because of their fabrication problems. In particular, the main drawback of technique 2-based phantom is the lack of good adhesion between the two substrates (1.5% agarose and PDMS). As for technique 4, on the other hand, the substrate realised is not completely homogeneous due to the lack of a machine that allows to heat the 10%-15% agarose under vacuum to avoid the bubbles' formation [57, 55].
Examining the results of insertion tests performed on the three other types of phantom, it is observed that PDMS cylinder-based phantom (technique 3) doesn't permit the device insertion, due to its high stiffness giving, thus, a negative feedback. By contrast, the thin PDMS layer-based phantom (technique 5) reported non-comparable insertion forces, lower than the fresh optic nerve's ones. As for technique 1 (1.5% agarose and PDMS), it has given a good performance. Besides, this technique allows to realise a phantom geometrically similar to real nerve and could be used for both insertion and extraction analysis, while the phantoms realised in Technique 3, 4 and 5 were fabricated only to assess the insertion forces.
Comparing the insertion tests results obtained with phantom and explanted rabbit, it can

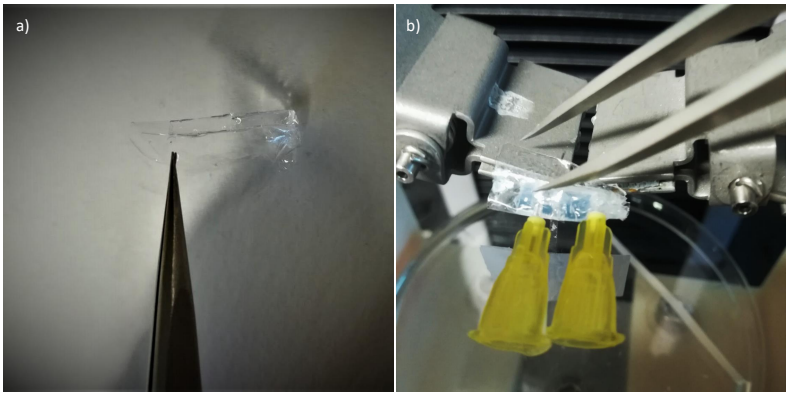

Figure 5.22: (*a*) Nerve phantom realised according to technique 1: parallelepiped of 1.5% agarose wrapped by 50 μm thick 10:1 PDMS. The ends of the PDMS layer were not cut to make it easier to handle the phantom during the tests. (*b*) Mechanical tests performed with nerve phantom.

be stated that the phantom nerve made with 1.5% agarose and surrounded by a layer of PDMS 10:1, 50 μm thick, has a mechanical behaviour very similar to the rabbit optic nerve. Figure 5.23 shows the trends of different samples (PI Design 2, PI Design 1, OSTE+ CC Design 2 and three layers Design 2) tested with phantom nerve in question and with fresh optic nerve. The three layers based samples broke in both situations after the insertion of the tip and before reaching the active area.
As for extraction tests, by contrast, the results obtained with nerve phantom (technique 1) are different from those evaluated with ex-vivo nerve. In particular, the peaks values, related to the extraction of wings anchored inside the nerve, are higher than nerve phantom's ones, as shown in Figure 5.24. Moreover, they are shifted compared with fresh nerve's ones because they develop when the wings pass through PDMS external layer.
The probable explanation of these results is related to optic nerve conformation, which is different from nerve phantom. The real nerve is characterised by axons bundles and, so, allows wings to anchor inside the nerve. By contrast, the phantom is composed of homogeneous agarose and doesn't reproduce the real configuration of fibres. For this reason, wings are not able to anchor well inside the phantom.

In conclusion, this phantom could be used in mechanical insertion tests to optimise the device structure and to assess the compatibility of the insertion forces with the implant. However, it is not suitable for any evaluation of the device fastening, due to the unrealistic conformation of the nerve tissue reproduced without axons bundles.
A possible improvement is, certainly, the addition of a compound able to simulate the fibres. An alternative to the described phantom is to use the gel wax material (reported in Section 1.10), whose mechanical characteristics are similar to the nerve. Maneas et al. have been presented a method to create heterogeneous tissue composed of cylindrical structure to mimic the nerve, adding glass spheres and paraffin wax to reproduce the tissue acoustic properties. This phantom, free of a pia mater-like material, could be covered by a layer of PDMS in order to simulate the pia mater, necessary for the evaluation of the insertion forces. Of course, an assessment of the adhesion of the two different materials should be carried out.

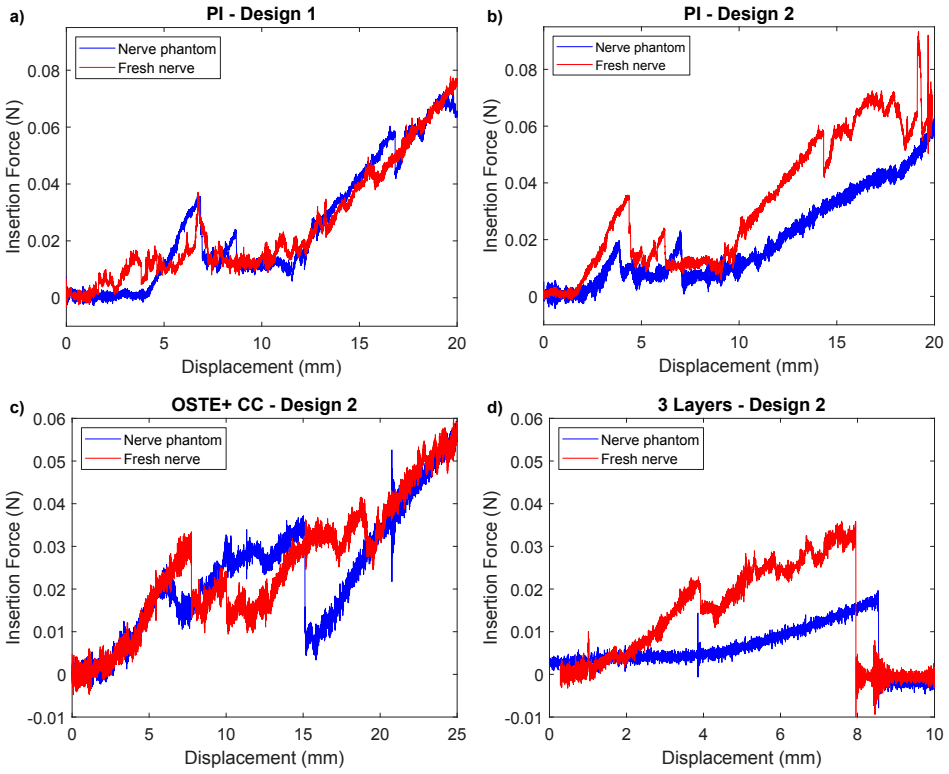

Figure 5.23: Comparison of insertion tests between nerve phantom (in blue) and fresh nerve (in red). The first peak is related to the tip insertion, while the second peak to the area enlargement. Samples analysed are PI Design 1 (*a*), PI Design 2 (*b*), OSTE+ CC Design 2 (*c*) and three layers Design 2 (*d*). For the three-layer substrate, the device breaks before to reach the active area in both fresh optic nerve and phantom. The graphs are referred on a single sample for each condition.

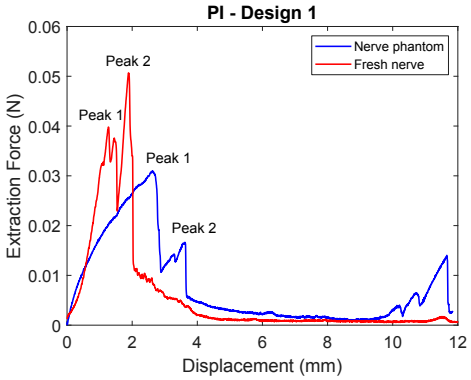

Figure 5.24: Comparison of extraction tests between nerve phantom (in blue) and fresh nerve (in red). The two peaks are related to the wings extraction. Samples analysed are PI Design 1.

6 Conclusion and Prospects

The OpticSELINE is the self-opening intraneural electrodes, implanted for optic nerve stimulation to partially restore the visual functionality of blind people. It is currently made in PI and has been implanted only in rabbit optic nerve. The flexibility of the electrodes is an important aspect to keep in mind to ensure greater longevity of the implant. Brittle and high stiffness devices cause a thickening of the neurons around their interface as a result of their inability to deform and, at the same time, reduce their functionality [67, 35]. To make the implant more compliant with neural tissue, in this work OpticSELINE in OSTE+, a photopatternable polymer with tunable mechanical properties, has been fabricated and mechanically tested.

The process flow of OpticSELINE fabrication, both in OSTE+ CC and in three-layers substrate (OSTE+ Flex/OSTE+ CC/OSTE+ Flex), has been optimised and presented in this work. It has been demonstrated the possibility to realise a more compliant device in OSTE+, even if this modification of device substrate has required some structural variations. Of course, three-layers based OpticSELINE still needs optimisation to overcome some issue related to its fabrication.

Two designs have been proposed with different size, one with the dimension of the active area comparable to the current version and one with 1.86 times larger active area. The mechanical tests, carried out on OpticSELINE, have shown that the insertion forces are compatible with the device in OSTE+ for both designs. However, the insertion of a three-layer based device requires a slightly different procedure due to the low stiffness of the material. As for the device anchorage, it has been proved the wings in the active configuration ensure good stability inside the nerve. Moreover, the wider wing design (Design 2) improves the performance of the anchorage system. However, an improvement of the anchorage for three-layer based device could be achieved by modifying the second layer with the introduction of SU-8 or a photosensitive polyimide, or by thickening OSTE+ CC layer essential to memorize the wings.

The main purpose of the wider design is to increase not only the mechanical stability of the implant but also the number of electrodes. Maintaining the same size of the wings, reported in this work, and increasing the width of the active area from 0.8 mm to 0.82 mm to fit with traces dimensions, a future design could be characterised by 12 electrodes per each side instead of 6. This design could improve the stimulation of the optic nerve fibres. Moreover, there shouldn't be problems during insertion of the device because of this enlargement of the active area to 0.82 mm.

Another possible future improvement of the device could be the use of stretchable inter-

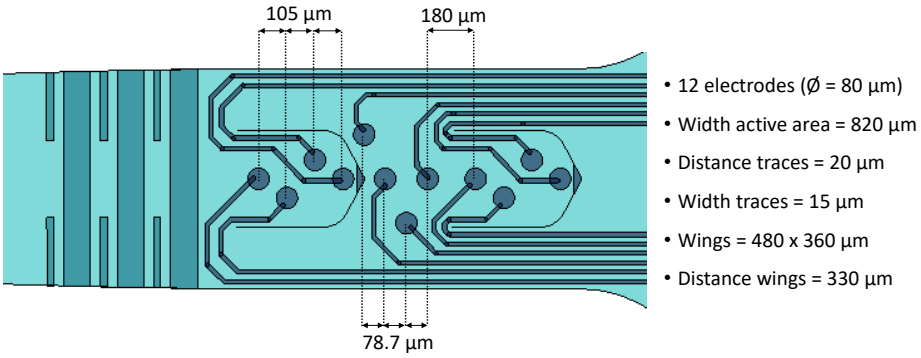

Figure 6.1: Possible future design with 12 electrodes per each side.

connects embedded in a soft matrix of OSTE+ [34]. It consists in using Au-coated TiO_2 nanowires with low impedance and high capacity for conductive tracks, instead of platinum interconnects more stiff material with a Young modulus of about 50- 500 GPa and more fragile. In this way, it is possible to reduce the mismatch between OSTE+ and electronics and overcome some issues related to fabrication. Of course, to confirm the optimisation of biocompatibility, it is also necessary to analyse biointegration and evaluate the foreign body reaction of the new softer design.

In conclusion, an innovative and more compliant OpticSELINE has been realised together with supports for its fabrication and mechanical testing. This new design could reduce the foreign body reaction thanks to OSTE+ substrate, increase the stimulation performance and guarantee a good mechanical stability inside the nerve.

Bibliography

[1] Blindness and vision impairment, Accessed: 13/04/2019. URL https://www.who.int/blindness/vision-report/wrv-info/en/.

[2] Stephen Bagi Liz Segre. Eye anatomy: A closer look at the parts of the eye, Accessed: 06/07/2019. URL https://www.allaboutvision.com/resources/anatomy.htm.

[3] adapted by Jennifer Walinga from Charles Stangor's textbook. *Introduction to Psychology: 1st Canadian Edition*, page Chapter 5 (Sensing and Perceiving). Thieme, 2012.

[4] Tim Newman. An introduction to eyes and how they work. *Medical News Today*, Accessed: 13/04/2019. URL https://www.medicalnewstoday.com/articles/320608.php.

[5] J.Uwe Meyer. Retina implant - a biomems challenge. *Fraunhofer-Institute for Biomedical Engineering*, 2001. URL https://www.britannica.com/print/article/430325.

[6] Nancy J. Fischbein Devin K. Binder, D. Christian Sonne. *Cranial Nerves: Anatomy, Pathology, Imaging*, pages 9–17. Thieme, 2010.

[7] Daniel M. Albert David M. Gamm. Optic nerve anatomy. *Enciclopedia Britannica*, 07/05/2015. URL https://www.britannica.com/science/\optic-nerve.

[8] The optic nerve, Accessed 13/04/2019. URL https://www.kenhub.com/en/library/anatomy/the-optic-nerve.

[9] Alfredo A. Sadun and Michelle Y. Wang. Chapter 5 - abnormalities of the optic disc. In Christopher Kennard and R. John Leigh, editors, *Neuro-ophthalmology*, volume 102 of *Handbook of Clinical Neurology*, pages 117 – 157. Elsevier, 2011. doi: https://doi.org/10.1016/B978-0-444-52903-9.00011-X. URL http://www.sciencedirect.com/science/article/pii/B978044452903900011X.

[10] Euronext Paris. Pixium Vision Focus shifts to Prima as human trials proceed, 2017.

[11] Ibrahim Mohammed Alotaibi. Artificial Vision - Visual Prosthesis. *International Journal of Research in Business and Technology*, 10(2):348–352, 2018. doi: 10.17722/ijrbt.v10i2.485.

[12] Smarter, smaller, better, Accessed: 13/04/2019. URL https://www.nano-retina.com/.

[13] Alejandro Barriga-Rivera, Lilach Bareket, Josef Goding, Ulises A. Aregueta-Robles, and Gregg J. Suaning. Visual prosthesis: Interfacing stimulating electrodes with retinal neurons to restore vision. *Frontiers in Neuroscience*, 11(NOV):1–17, 2017. ISSN 1662453X. doi: 10.3389/fnins.2017.00620.

[14] Yvonne H.L. Luo and Lyndon Da Cruz. A review and update on the current status of retinal prostheses (bionic eye). *British Medical Bulletin*, 109(1):31–44, 2014. ISSN 14718391. doi: 10.1093/bmb/ldu002.

[15] Karen C Cheung. Implantable microscale neural interfaces, 2007.

[16] Analiz Rodriguez James M. Anderson and David T. Chang. Foreign Body Reaction to Biomaterials, 2009.

[17] Ivan R. Minev, Pavel Musienko, Arthur Hirsch, Quentin Barraud, Nikolaus Wenger, Eduardo Martin Moraud, Jérôme Gandar, Marco Capogrosso, Tomislav Milekovic, Léonie Asboth, Rafael Fajardo Torres, Nicolas Vachicouras, Qihan Liu, Natalia Pavlova, Simone Duis, Alexandre Larmagnac, Janos Vörös, Silvestro Micera, Zhigang Suo, Grégoire Courtine, and Stéphanie P. Lacour. Electronic dura mater for long-term multimodal neural interfaces. *Science*, 347(6218):159–163, 2015. ISSN 0036-8075. doi: 10.1126/science.1260318. URL `https://science.sciencemag.org/content/347/6218/159`.

[18] Vadim S. Polikov, Patrick A. Tresco, and William M. Reichert. Response of brain tissue to chronically implanted neural electrodes. *Journal of Neuroscience Methods*, 148(1): 1–18, 2005. ISSN 01650270. doi: 10.1016/j.jneumeth.2005.08.015.

[19] Roy Biran, Dave C. Martin, and Patrick A. Tresco. The brain tissue response to implanted silicon microelectrode arrays is increased when the device is tethered to the skull. *Journal of Biomedical Materials Research Part A*, 82A(1):169–178, 2007. doi: 10.1002/jbm.a.31138. URL `https://onlinelibrary.wiley.com/doi/abs/10.1002/jbm.a.31138`.

[20] Roy Biran, Dave C. Martin, and Patrick A. Tresco. The brain tissue response to implanted silicon microelectrode arrays is increased when the device is tethered to the skull. *Journal of Biomedical Materials Research Part A*, 82A(1):169–178, 2007. doi: 10.1002/jbm.a.31138. URL `https://onlinelibrary.wiley.com/doi/abs/10.1002/jbm.a.31138`.

[21] Lisa C. Olmos de Koo Mark S.Humayun. *Retinal Prosthesis, a clinical guide to successful implementation*, page Chapter 1. Springer, 2018.

[22] Robert K. Shepherd, Mohit N. Shivdasani, David A X Nayagam, Christopher E. Williams, and Peter J. Blamey. Visual prostheses for the blind. *Trends in Biotechnology*, 31(10):562–571, 2013. ISSN 01677799. doi: 10.1016/j.tibtech.2013.07.001. URL `http://dx.doi.org/10.1016/j.tibtech.2013.07.001`.

[23] Mohammad Riazi-Esfahani, MohammadHossein Maghami, AmirMasoud Sodagar, Alireza Lashay, and Hamid Riazi-Esfahani. Visual prostheses: The enabling technology to give sight to the blind. *Journal of Ophthalmic and Vision Research*, 9(4):494, 2015. ISSN 2008-322X. doi: 10.4103/2008-322x.150830.

[24] Occhio bionico, Accessed: 13/04/2019. URL `http://www.iapb.it/occhio-bionico`.

[25] Philip M. Lewis, Helen M. Ackland, Arthur J. Lowery, and Jeffrey V. Rosenfeld. Restoration of vision in blind individuals using bionic devices: A review with a focus on cortical visual prostheses. *Brain Research*, 1595:51–73, 2015. ISSN 18726240. doi: 10.1016/j.brainres.2014.11.020. URL `http://dx.doi.org/10.1016/j.brainres.2014.11.020`.

[26] Hirokazu Sakaguchi, Motohiro Kamei, Kentaro Nishida, Yasuo Terasawa, Takashi Fujikado, Motoki Ozawa, and Kohji Nishida. Implantation of a newly developed direct optic nerve electrode device for artificial vision in rabbits. *Journal of Artificial Organs*, 15(3):295–300, 2012. ISSN 14347229. doi: 10.1007/s10047-012-0642-8.

[27] Xinyu Chai Xinyu Chai, Liming Li Liming Li, Kaijie Wu Kaijie Wu, Chuanqing Zhou Chuanqing Zhou, Pengjia Cao Pengjia Cao, and Qiushi Ren Qiushi Ren. C-Sight Visual Prostheses for the Blind. *IEEE Engineering in Medicine and Biology Magazine*, 27(5):20–28, 2008. ISSN 07395175. doi: 10.1109/MEMB.2008.923959. URL `http://www.ncbi.nlm.nih.gov/pubmed/18799386`.

[28] A. Cutrone, J. Del Valle, D. Santos, J. Badia, C. Filippeschi, S. Micera, X. Navarro, and S. Bossi. A three-dimensional self-opening intraneural peripheral interface (SELINE). *Journal of Neural Engineering*, 12(1):16016, 2015. ISSN 17412552. doi: 10.1088/1741-2560/12/1/016016. URL `http://dx.doi.org/10.1088/1741-2560/12/1/016016`.

[29] Emil H. Rijnbeek, Nick Eleveld, and Wouter Olthuis. Update on peripheral nerve electrodes for closed-loop neuroprosthetics. *Frontiers in Neuroscience*, 12(MAY):1–9, 2018. ISSN 1662453X. doi: 10.3389/fnins.2018.00350.

[30] Huaiqiang Yu, Wenjie Xiong, Hongze Zhang, Wei Wang, and Zhihong Li. A parylene self-locking cuff electrode for peripheral nerve stimulation and recording. *Journal of Microelectromechanical Systems*, 23(5):1025–1035, 2014. ISSN 10577157. doi: 10.1109/JMEMS.2014.2333733.

[31] Annarita Cutrone, Pier Nicola Sergi, Silvia Bossi, and Silvestro Micera. Modelization of a self-opening peripheral neural interface: A feasibility study. *Medical Engineering and Physics*, 33(10):1254–1261, 2011. ISSN 13504533. doi: 10.1016/j.medengphy.2011.06.001. URL `http://dx.doi.org/10.1016/j.medengphy.2011.06.001`.

[32] S. Wurth, M. Capogrosso, S. Raspopovic, J. Gandar, G. Federici, N. Kinany, A. Cutrone, A. Piersigilli, N. Pavlova, R. Guiet, G. Taverni, J. Rigosa, P. Shkorbatova, X. Navarro, Q. Barraud, G. Courtine, and S. Micera. Long-term usability and bio-integration of polyimide-based intra-neural stimulating electrodes. *Biomaterials*, 122:114–129, 2017. ISSN 18785905. doi: 10.1016/j.biomaterials.2017.01.014. URL `http://dx.doi.org/10.1016/j.biomaterials.2017.01.014`.

[33] Vivien Gaillet, Annarita Cutrone, Fiorenzo Artoni, Paola Vagni, Ariastity Mega Pratiwi, Sandra Alejandra Romero, Dario Lipucci Di Paola, Silvestro Micera, and Diego Ghezzi. Spatially selective activation of the visual cortex via intraneural stimulation of the optic nerve. *Nature Biomedical Engineering*, 2019. ISSN 2157-846X. doi: 10.1038/s41551-019-0446-8. URL `https://doi.org/10.1038/s41551-019-0446-8`.

[34] Eleonora Borda and Carlotta Guiducci. Fabrication and Validation of a self-opening intraneural interface tailored for optic nerve, PhD THESIS PROPOSAL, 2018.

[35] Stéphanie P. Lacour, Grégoire Courtine, and Jochen Guck. Materials and technologies for soft implantable neuroprostheses. *Nature Reviews Materials*, 1(10), 2016. ISSN 20588437. doi: 10.1038/natrevmats.2016.63.

[36] P Lacour, Samia Benmerah, Edward Tarte, and Barclay Morrison Iii. Flexible and stretchable micro-electrodes for in vitro and in vivo neural interfaces, 2010.

[37] Kinam Park, Janak Gaire, Kevin J Otto, Heui Chang Lee, Jens Schouenborg, Fredrik Ejserholm, Martin Bengtsson, Seth Currlin, and Lars Wallman. Histological evaluation of flexible neural implants; flexibility limit for reducing the tissue response?

Journal of Neural Engineering, 14(3):036026, 2017. ISSN 1741-2560. doi: 10.1088/1741-2552/aa68f0.

[38] Miao Liu, Jianren Sun, Ying Sun, Christopher Bock, and Quanfang Chen. Thickness-dependent mechanical properties of polydimethylsiloxane membranes. *Journal of Micromechanics and Microengineering*, 19(3):035028, feb 2009. doi: 10.1088/0960-1317/19/3/035028. URL https://doi.org/10.1088%2F0960-1317%2F19%2F3%2F035028.

[39] The Dow and Chemical Company. SYLGARD ™ 184 Silicone Elastomer APPLICATIONS, 2017.

[40] I D Johnston. Mechanical characterization of bulk Sylgard 184 for microfluidics and microengineering, 2014.

[41] Anton Georgiev, Dean Dimov, Erinche Spassova, Jacob Assa, Peter Dineff, and Gencho Danev. Chemical and physical properties of polyimides: Biomedical and engineering applications. In Marc J.M. Abadie, editor, *High Performance Polymers - Polyimides Based*, chapter 4. IntechOpen, Rijeka, 2012. doi: 10.5772/53918. URL https://doi.org/10.5772/53918.

[42] HD MicroSystems. PI-2600 Series – Low Stress Applications, 2009.

[43] Carl Fredrik Carlborg, Tommy Haraldsson, Kim Öberg, Michael Malkoch, and Wouter Van Der Wijngaart. Beyond PDMS: Off-stoichiometry thiol-ene (OSTE) based soft lithography for rapid prototyping of microfluidic devices. *Lab on a Chip*, 11(18):3136–3147, 2011. ISSN 14730189. doi: 10.1039/c1lc20388f.

[44] Carl Fredrik Carlborg, Alexander Vastesson, Yitong Liu, Wouter Van Der Wijngaart, Mats Johansson, and Tommy Haraldsson. Functional off-stoichiometry thiol-ene-epoxy thermosets featuring temporally controlled curing stages via an UV/UV dual cure process. *Journal of Polymer Science, Part A: Polymer Chemistry*, 52(18):2604–2615, 2014. ISSN 10990518. doi: 10.1002/pola.27276.

[45] Fredrik Ejserholm, John Stegmayr, Patrik Bauer, Fredrik Johansson, Lars Wallman, Martin Bengtsson, and Stina Oredsson. Biocompatibility of a polymer based on Off-Stoichiometry Thiol-Enes + Epoxy (OSTE+) for neural implants. *Biomaterials Research*, 19(1):1–10, 2015. ISSN 20557124. doi: 10.1186/s40824-015-0041-3. URL http://dx.doi.org/10.1186/s40824-015-0041-3.

[46] Andrew Shin, Lawrence Yoo, Joseph Park, and Joseph L. Demer. Finite Element Biomechanics of Optic Nerve Sheath Traction in Adduction. *Journal of Biomechanical Engineering*, 139(10):101010, 2017. ISSN 0148-0731. doi: 10.1115/1.4037562.

[47] Ian A. Sigal. Interactions between geometry and mechanical properties on the optic nerve head. *Investigative Ophthalmology and Visual Science*, 50(6):2785–2795, 2009. ISSN 01460404. doi: 10.1167/iovs.08-3095.

[48] Ian A. Sigal, John G. Flanagan, Inka Tertinegg, and C. Ross Ethier. Finite element modeling of optic nerve head biomechanics. *Investigative Ophthalmology and Visual Science*, 45(12):4378–4387, 2004. ISSN 01460404. doi: 10.1167/iovs.04-0133.

[49] Yuying Jiang, Haitao Xu, Jingxiang Liu, Peng Li, and Yazhen Wu. Biomechanical analysis of optic nerve injury treated by compound light granules and ciliary neurotrophic factor. *Neural regeneration research*, 7(36):2889–2900, dec 2012. ISSN 1673-5374. doi: 10.3969/j.issn.1673-5374.2012.36.006. URLhttps://www.ncbi.nlm.nih.gov/pubmed/25317141https://www.ncbi.nlm.nih.gov/pmc/PMC4190947/.

[50] Efthymios Maneas, Wenfeng Xia, Daniil I Nikitichev, Batol Daher, Maniragav Manimaran, Rui Yen J Wong, Chia-Wei Chang, Benyamin Rahmani, Claudio Capelli, Silvia Schievano, Gaetano Burriesci, Sebastien Ourselin, Anna L David, Malcolm C Finlay, Simeon J West, Tom Vercauteren, and Adrien E Desjardins. Anatomically realistic ultrasound phantoms using gel wax with 3D printed moulds. *Physics in medicine and biology*, 63(1):15033, jan 2018. ISSN 1361-6560. doi: 10.1088/1361-6560/aa9e2c. URL https://www.ncbi.nlm.nih.gov/pubmed/29186007https://www.ncbi.nlm.nih.gov/pmc/articles/PMC5802334/.

[51] Antonio E. Forte, Stefano Galvan, Francesco Manieri, Ferdinando Rodriguez y Baena, and Daniele Dini. A composite hydrogel for brain tissue phantoms. *Materials and Design*, 112:227–238, 2016. ISSN 18734197. doi: 10.1016/j.matdes.2016.09.063. URL http://dx.doi.org/10.1016/j.matdes.2016.09.063.

[52] Madhuvanthi A Kandadai, Jason L Raymond, and George J Shaw. Comparison of electrical conductivities of various brain phantom gels: Developing a 'Brain Gel Model'. *Materials science & engineering. C, Materials for biological applications*, 32(8):2664–2667, dec 2012. ISSN 1873-0191. doi: 10.1016/j.msec.2012.07.024. URL https://www.ncbi.nlm.nih.gov/pubmed/23139442https://www.ncbi.nlm.nih.gov/pmc/articles/PMC3489480/.

[53] Roland Pomfret, Gurwattan Miranpuri, and Karl Sillay. The substitute brain and the potential of the gel model. *Annals of Neurosciences*, 20(3):118–122, 2013. ISSN 09727531. doi: 10.5214/ans.0972.7531.200309.

[54] Ernest L Madsen, Maritza A Hobson, Hairong Shi, Tomy Varghese, and Gary R Frank. Tissue-mimicking agar/gelatin materials for use in heterogeneous elastography phantoms. *Physics in medicine and biology*, 50(23):5597–5618, dec 2005. ISSN 0031-9155. doi: 10.1088/0031-9155/50/23/013. URL https://www.ncbi.nlm.nih.gov/pubmed/16306655https://www.ncbi.nlm.nih.gov/pmc/articles/PMC3769983/.

[55] Valéry Normand, Didier L. Lootens, Eleonora Amici, Kevin P. Plucknett, and Pierre Aymard. New insight into agarose gel mechanical properties. *Biomacromolecules*, 1(4):730–738, 2000. ISSN 15257797. doi: 10.1021/bm005583j.

[56] Conor T. Buckley, Stephen D. Thorpe, Fergal J. O'Brien, Anthony J. Robinson, and Daniel J. Kelly. The effect of concentration, thermal history and cell seeding density on the initial mechanical properties of agarose hydrogels. *Journal of the Mechanical Behavior of Biomedical Materials*, 2(5):512–521, 2009. ISSN 17516161. doi: 10.1016/j.jmbbm.2008.12.007. URL http://dx.doi.org/10.1016/j.jmbbm.2008.12.007.

[57] Justine J. Roberts, Audrey Earnshaw, Virginia L. Ferguson, and Stephanie J. Bryant. Comparative study of the viscoelastic mechanical behavior of agarose and poly(ethylene glycol) hydrogels. *Journal of Biomedical Materials Research - Part B Applied Biomaterials*, 99 B(1):158–169, 2011. ISSN 15524973. doi: 10.1002/jbm.b.31883.

[58] F. Ejserholm, A. Vastesson, T. Haraldsson, W. Van Der Wijngaart, J. Schouenborg, L. Wallman, and M. Bengtsson. A polymer neural probe with tunable flexibility. *International IEEE/EMBS Conference on Neural Engineering, NER*, pages 691–694, 2013. ISSN 19483546. doi: 10.1109/NER.2013.6696028.

[59] Commission Regulation. OUR NEWEST COLORING POWER NORIT ® E 153 ACTIVATED CARBON PRODUCT PORTFOLIO INCLUDING NORIT A ULTRA E 153, 2012.

[60] AZoM. Platinum - properties and applications, 23/07/2001. URL https://www.azom.com/properties.aspx?ArticleID=601.

[61] Ghader Faraji, Hyoung Seop Kim, and Hessam Torabzadeh Kashi. Introduction. In Ghader Faraji, Hyoung Seop Kim, and Hessam Torabzadeh Kashi, editors, *Severe Plastic Deformation*, pages 1 – 17. Elsevier, 2018. ISBN 978-0-12-813518-1. doi: https://doi.org/10.1016/B978-0-12-813518-1.00020-5. URL http://www.sciencedirect.com/science/article/pii/B9780128135181000205.

[62] Mohamad HajjHassan, Vamsy Chodavarapu, and Sam Musallam. NeuroMEMS: Neural Probe Microtechnologies. *Sensors (Basel, Switzerland)*, 8 (10):6704–6726, oct 2008. ISSN 1424-8220. doi: 10.3390/s8106704. URL https://www.ncbi.nlm.nih.gov/pubmed/27873894https://www.ncbi.nlm.nih.gov/pmc/articles/PMC3707475/.

[63] Name Description Ostemer, Crystal Clear, Storage Handling Room, and U V Reaction. Ostemer® 322 Crystal Clear, 2017. URL http://www.ostemers.com/wp-content/uploads/2017/11/Data-sheet-OSTEMER-322-Crystal-Clear-v4{_}opt.pdf.

[64] Meng Deng, Xi Yang, Musa Silke, Weiming Qiu, Mingsheng Xu, Gustaaf Borghs, and Hongzheng Chen. Electrochemical deposition of polypyrrole/graphene oxide composite on microelectrodes towards tuning the electrochemical properties of neural probes. *Sensors and Actuators, B: Chemical*, 158(1):176–184, 2011. ISSN 09254005. doi: 10.1016/j.snb.2011.05.062. URL http://dx.doi.org/10.1016/j.snb.2011.05.062.

[65] Jiali Gao, Le Guan, and Jinkui Chu. Determining the Young's modulus of SU-8 negative photoresist through tensile testing for MEMS applications. In *Proc.SPIE*, volume 7544, dec 2010. URL https://doi.org/10.1117/12.885983.

[66] Ken Ichi Fukukawa and Mitsuru Ueda. Recent progress of photosensitive polyimides. *Polymer Journal*, 40(4):281–296, 2008. ISSN 00323896. doi: 10.1295/polymj.PJ2007178.

[67] Harbaljit S Sohal, Gavin J Clowry, Andrew Jackson, Anthony O'Neill, and Stuart N Baker. Mechanical Flexibility Reduces the Foreign Body Response to Long-Term Implanted Microelectrodes in Rabbit Cortex. *PloS one*, 11 (10):e0165606, 2016. ISSN 1932-6203. doi: 10.1371/journal.pone.0165606. URL http://www.ncbi.nlm.nih.gov/pubmed/27788240{%}0Ahttp://www.pubmedcentral.nih.gov/articlerender.fcgi?artid=PMC5082854.

Appendices

Table 6.1: Laser cutter parameters

Material	Thickness (μm)	Speed	Jump Speed	Firing Rate	Laser Power	Rep. Object
PI	12.5	300	300	100	32	5
PI	50	300	300	100	55	55
Alu foil		100	100	150	70	50
PET	23	300	300	100	35	20
PET + PDMS	23 + 50	100	100	100	35	30
OSTE+ CC	60	300	300	100	60	60
OSTE+ CC	30	300	300	70	50	30
OSTE+ CC + encap	20 + 5	300	300	70	38	30
OSTE+ CC	5	300	300	100	30	30
OSTE+ Flex	60	300	300	100	38	50
OSTE+ Flex	30	300	300	100	38	45
3 Layers	20	300	300	100	35	20
3 Layers + encap	20 + 5	300	300	100	35	20
Si scribing	-	200	200	50	20	1

Table 6.2: Spin coating parameters

Recipe	Step	Spin Speed (rpm)	Acceleration (rpm/s)	Spin Time duration (s)
325 rpm	1	200	100	5
	2	325	100	35
	3	1325	1000	1
	4	325	500	5
	5	0	500	15
1000 rpm	1	500	100	10
	2	1000	100	65
	3	2000	1000	1
	4	1000	500	10
	5		500	5
1500 rpm	1	500	100	10
	2	1500	100	65
	3	2500	1000	1
	4	1500	500	10
	5	0	500	5
2000 rpm standard	1	500	100	10
	2	2000	100	65
	3	3000	1000	1
	4	2000	500	10
	5	0	500	5
2000 rpm new	1	1000	100	10
	2	2000	100	120
	3	1000	500	10
	4	0	500	10
2500 rpm	1	500	100	10
	2	2500	200	70
	3	3500	1000	1
	4	2500	500	6
	5	0	500	5
3000 rpm	1	500	100	10
	2	3000	200	70
	3	4000	1000	1
	4	3000	500	6
	5	0	500	6
3500 rpm	1	500	100	10
	2	3500	100	65
	3	4500	1000	1
	4	3500	500	10
	5	0	500	10
4000 rpm	1	500	100	10
	2	4000	100	65
	3	5000	1000	1
	4	4000	500	10
	5	0	500	10

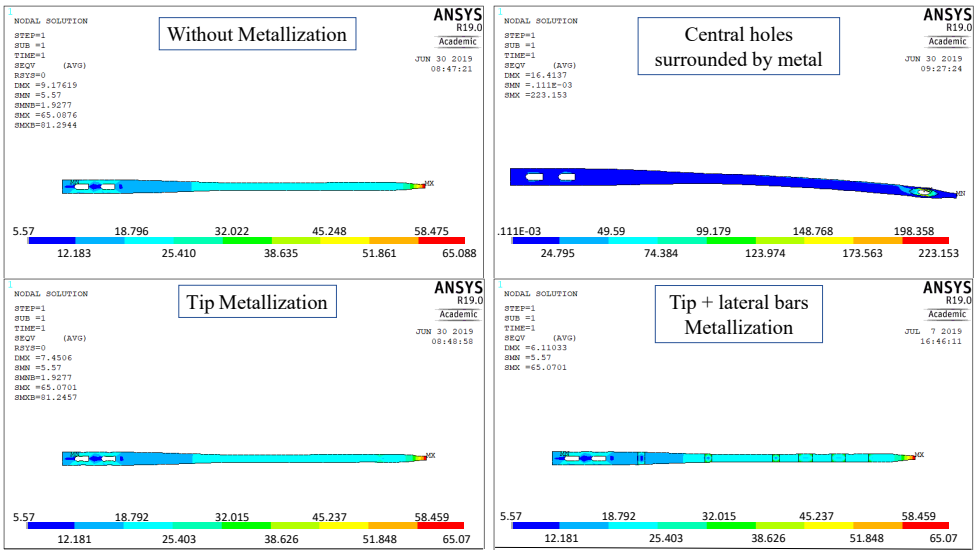

Figure 6.2: Von Mises stresses distribution of Design 1 in OSTE+ Flex for four support configurations: without metallic reinforcement, central holes surrounded by metal, tip with/without metallic transversal bars. Insertion force is 400 mN while the metal considered is platinum.

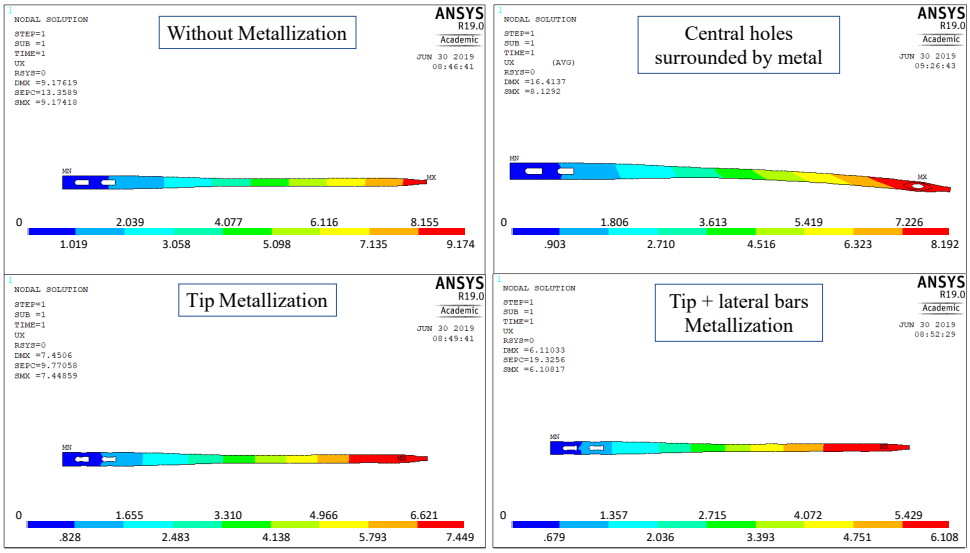

Figure 6.3: Displacement along x-axis of Design 1 in OSTE+ Flex for four support configurations: without metallic reinforcement, central holes surrounded by metal, tip with/without metallic transversal bars. Insertion force is 400 mN while the metal considered is platinum.

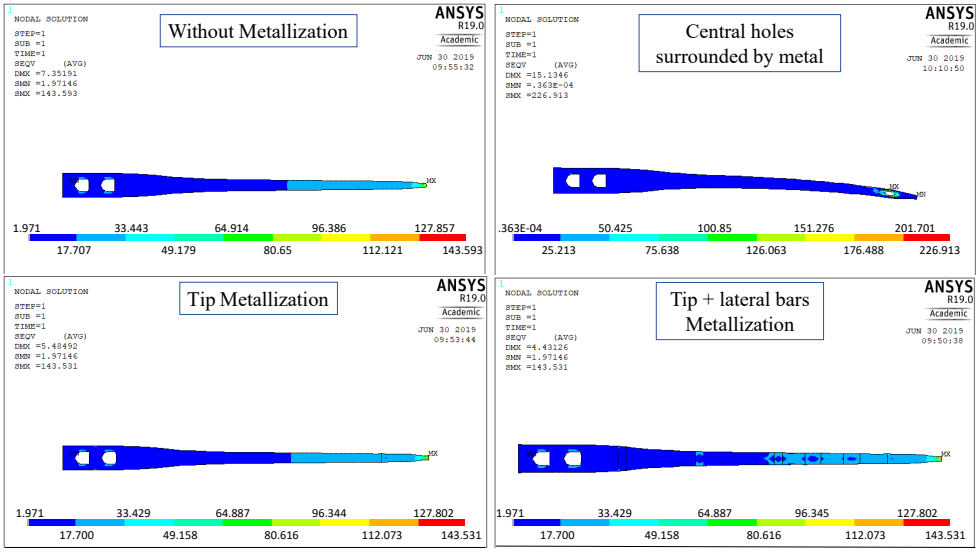

Figure 6.4: Von Mises stresses distribution of Design 2 in OSTE+ Flex for four support configurations: without metallic reinforcement, central holes surrounded by metal, tip with/without metallic transversal bars. Insertion force is 400 mN while the metal considered is platinum.

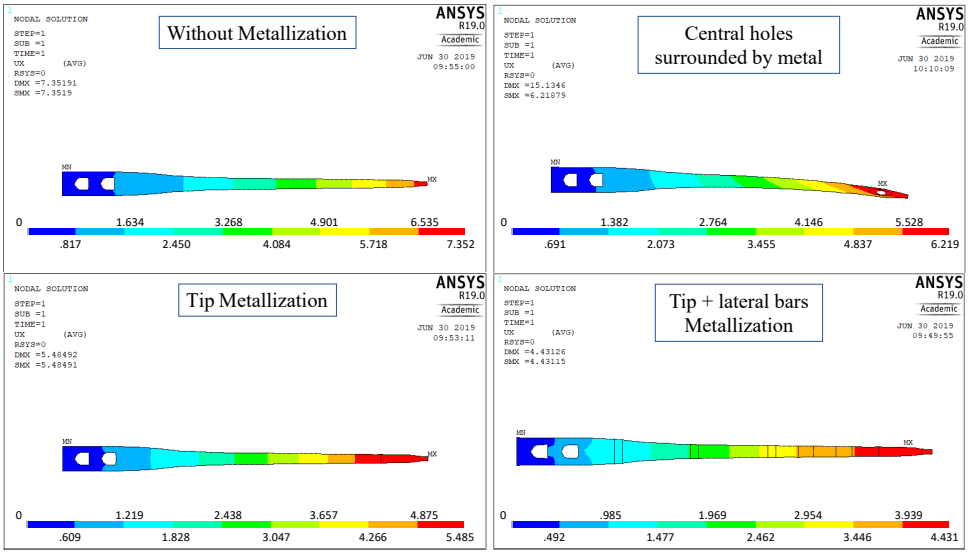

Figure 6.5: Displacement along x-axis of Design 2 in OSTE+ Flex for four support configurations: without metallic reinforcement, central holes surrounded by metal, tip with/without metallic transversal bars. Insertion force is 400 mN while the metal considered is platinum.

Step	Process description	Cross-section after process
01	**Substrate: Si** *Releasing layer (PSS)* Material: *PSS* Recipe: *2000 rpm + baking @ 145 °C for 10 min* Machine: *Spincoater*	
02	*OSTEmer coating and baking* Material: *OSTE+ Flex* Recipe: *2500 rpm + 2 min UV + 14h @ 100 °C* Machine: *OSTE mixer, Spincoater, Hotplate* Note: Baking at the center of HP + cooling down	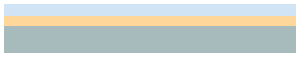
03	*OSTEmer coating* Material: *OSTE+ CC* Recipe: *3500 rpm* Machine: *OSTE mixer, Spincoater*	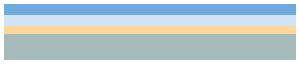
04	*Photolithography* Material: *250 µm thick PDMS film, Chrome mask* Recipe: *Hard contact - 60s x 2cycles - 10s hard contact time - 10s wait time* Machine: *MJB4* Note: *Before exposure, cast PDMS film onto uncured OSTE+ CC*	
05	*Development + Baking* Material: *Ethyl-l-lactate* Recipe: 5 min + shaker 70 rpm, *14h @ 100 °C* Machine: *Shaker, Hotplate* Note: Remove PDMS film during development	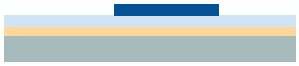
06	*OSTEmer coating and baking* Material: *OSTE+ Flex* Recipe: *2000 rpm + 2 min UV + 14h @ 100 °C* Machine: *OSTE mixer, Spincoater, Hotplate* Note: Baking at the center of HP + cooling down	
07	*Photolithography* Resist coating PR: *AZ1512 — 2.5 µm* Recipe*: 2 min @ 110 °C + cooling* Machine: *Semi-automatic coater, hotplate*	
08	*Exposure & Development* Recipe: *104 mJ/cm2 (λ=405 nm) + development 2.5* µm + rinse Machine: *MLA 150, Ritetrack developer*	

Figure 6.6: [Part 1/2] Complete process flow of OpticSELINE with substrate composed of OSTE+ Flex/OSTE+ CC/OSTE+ Flex and representation of cross-section after every step.

Step	Process description	Cross-section after process
09	*Pt sputtering* Material: 100 nm Pt Recipe: *100 W—low stress (DC_LS_Pt_100W)* Machine: *AC450* Note: Before sputtering, cover unnecessary parts of PR to faster lift off	
10	*Pt Lift off* Material: *PGMEA* Machine: *Wet bench + Sonication Bath RT* Note: Rinse with IPA and H20, take the wafer from the bath before sonication ends	
11	*OSTEmer encapsulation* Material: *OSTE+ Flex, Ethyl-l-lactate* Recipe: *2500 rpm (5-6* µm), 650 mJ/cm2 *(λ=375 nm) + 4 min @ 70 rpm in Ethyl-l-lactate, rinse in IPA, 14h @ 100 °C* Machine: *OSTE mixer, Spincoater, MLA 150, Hotplate* Note: Baking at the center of HP + cooling down	
12	*Laser cutter* Machine: *Laser cutter (Optec MM 200-US)* Recipe*: 300 300 100 35 20*	
13	*Release* Material: *DI* *Note: After release, dry device between tissues with weights placed on top*	
14	*Thermal memorization* Material: *metallic mold* Recipe: *40 °C overnight* Machine: *oven*	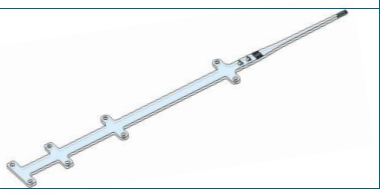

Figure 6.7: [Part 2/2] Complete process flow of OpticSELINE with substrate composed of OSTE+ Flex/OSTE+ CC/OSTE+ Flex and representation of cross-section after every step.

Step	Process description	Cross-section after process
01	**Substrate: Si** *Releasing layer (PSS)* Material: *PSS* Recipe: *2000 rpm + baking @ 145 °C for 10 min* Machine: *Spincoater*	
02	*OSTEmer coating and baking* Material: *OSTE+ CC* Recipe: *2000 rpm + 7 min UV + 14h @ 100 °C* Machine: *OSTE mixer, Spincoater, Hotplate* Note: Baking at the center of HP + cooling down	
03	*Photolithography* Resist coating PR: *AZ1512 — 2.5 µm* Recipe*: 2 min @ 110 °C + cooling* Machine: *Semi-automatic coater, hotplate*	
04	*Exposure & Development* Recipe: *104 mJ/cm2 (λ=405 nm) + development 2.5* µm + rinse Machine: *MLA 150, Ritetrack developer*	
05	*Pt sputtering* Material: 100 nm Pt Recipe: *100 W—low stress (DC_LS_Pt_100W)* Machine: *AC450* Note: Before sputtering, cover unnecessary parts of PR to faster lift off	
06	*Pt Lift off* Material: *PGMEA* Machine: *Wet bench + Sonication Bath RT* Note: Rinse with IPA and H20, take the wafer from the bath before sonication ends	
07	*OSTEmer encapsulation* Material: *OSTE+ Flex, Ethyl-l-lactate* Recipe: *2500 rpm (5-6* µm), 650 mJ/cm2 *(λ=375 nm) + 4 min @ 70 rpm in Ethyl-l-lactate, rinse in IPA, 14h @ 100 °C* Machine: *OSTE mixer, Spincoater, MLA 150, Hotplate* Note: Baking at the center of HP + cooling down	
08	*Laser cutter* Machine: *Laser cutter (Optec MM 200-US)* Recipe*: 300 300 70 38 30*	
09	*Release* Material: *DI* *Note: After release, dry device between tissues with weights placed on top*	
10	*Thermal memorization* Material: *metallic mold* Recipe: 5 h *@ 40 °C* Machine: *oven*	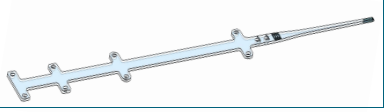

Figure 6.8: Complete process flow of OpticSELINE with substrate in OSTE+ CC and representation of cross-section after every step.